

**Exploring the Utilization of Magellan Drag and Reaction  
Wheel Data to Determine Latitudinal Variations in the Venus  
Upper Atmosphere**

by

Thomas James Schellenberg

B.S. December 1996, Pennsylvania State University

A Thesis submitted to

The Faculty of

The Graduate School of Engineering and Applied Science  
of The George Washington University in partial satisfaction  
of the requirements for the degree of Masters of Science

December, 1999

Thesis Directed by Dr. Robert Tolson



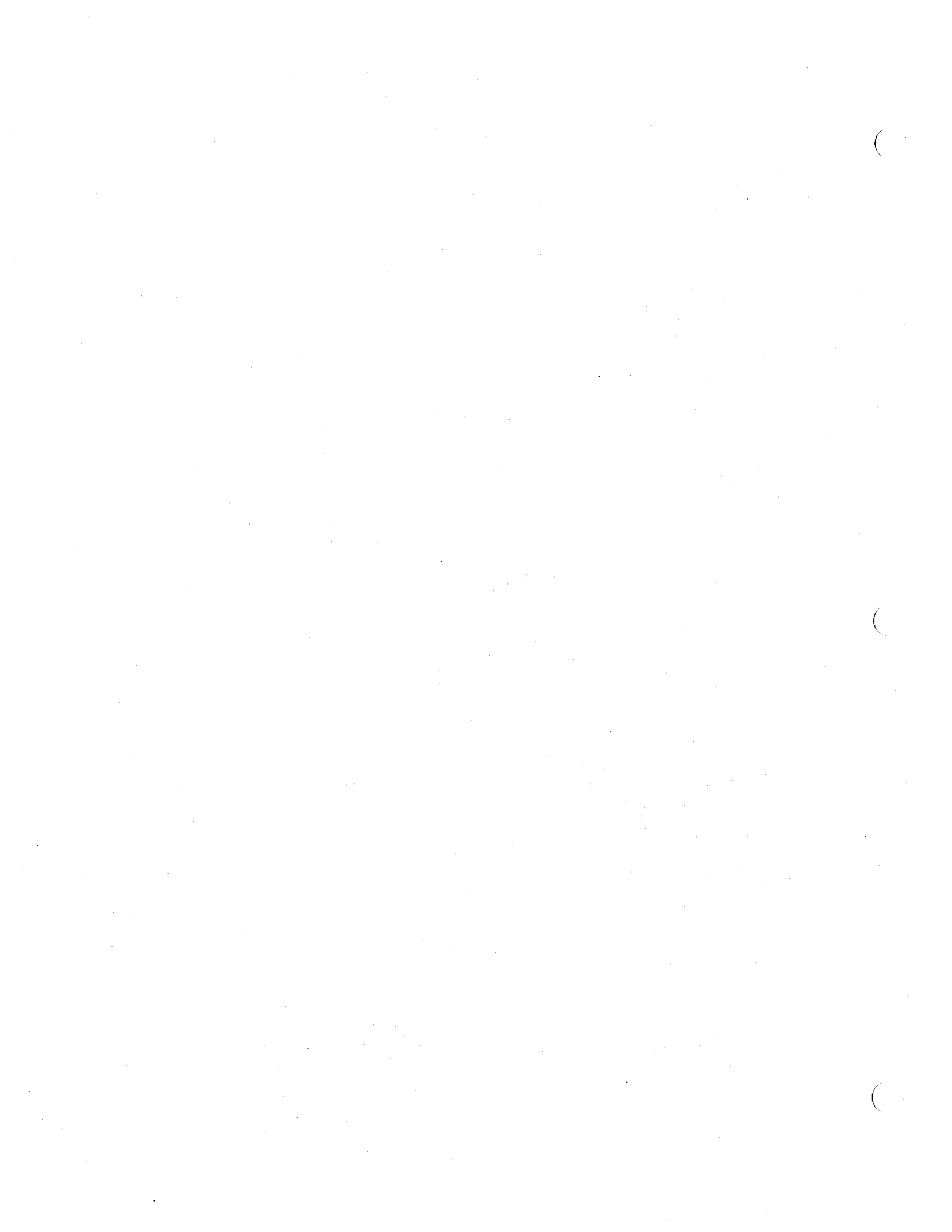
## ABSTRACT

Acquisition of combined atmospheric density measurements by the Pioneer Venus Orbiter (PVO) and the Magellan spacecraft provided an opportunity to update the Venus International Reference Atmosphere (VIRA) model. Drag data provided by PVO in 1992 and drag and reaction wheel data from Magellan measured during 1992, 1993, and 1994 were added to PVO data from 1978-1980 which were the only data used to construct the original VIRA model in 1985. The addition of Magellan data provided a wider sampling of latitude and solar activity than before. A minimum variance differential correction procedure minimized residuals and converged on an optimal set of coefficients. This study outlines the methods and steps taken to arrive at a possible update for the VIRA model. Possible updated sets of coefficients yield a model giving better estimates of latitudinal variation of the day side. This thesis sets forth a set of coefficients that produces a model which best fits available data. The updated set of coefficients provides insight into latitudinal variation of the model with a stronger drop off of density with respect to latitude on the dayside than expected.



## TABLE OF CONTENTS

ABSTRACT.....	ii
TABLE OF CONTENTS.....	iii
NOMENCLATURE AND ABBREVIATIONS.....	iv
I. INTRODUCTION.....	1
1.1 Overview.....	1
1.2 Purpose of This Study.....	2
II. VIRA MODEL.....	5
2.1 History.....	5
2.2 Boundary Conditions and Temperature Vertical Structure.....	8
2.3 Equations.....	11
2.4 Verification.....	15
III. DATA.....	17
3.1 Overview.....	17
3.2 Summary.....	20
3.3 Determination and Analysis of Reaction Wheel Data Bias.....	22
IV. DIFFERENTIAL CORRECTIONS METHOD.....	25
4.1 A Priori Differential Correction Method.....	25
4.2 Differential Corrections Steps.....	29
V. RESULTS.....	37
5.1 Method for Obtaining Results.....	37
5.2 Drag Data Results.....	39
5.3 Combined Drag and Reaction Wheel Data Results.....	44
5.4 Analysis of Coefficient Sets.....	50
5.5 Wave Activity on Venus.....	52
VI. DISCUSSION.....	55
VII CONCLUSIONS.....	64
REFERENCES.....	66
APPENDICES.....	68
Appendix A: One Step SZA Model Tables and Plots.....	68
Appendix B: Plots of Data Used to Define One Step SZA Model.....	78
Appendix C: Coefficient Solution Results and Correlation Tables.....	89
Appendix D: Observed Density Data Versus One Step SZA Model.....	99



## NOMENCLATURE AND ABBREVIATIONS

$F_{10}$	10.7 cm radio flux solar activity index ( $10^{-22}\text{Wm}^{-2}\text{Hz}^{-1}$ )
LST	Local Solar Time (hours from midnight)
OAD	Pioneer Venus Orbiter Atmospheric Drag
ONMS	Pioneer Venus Orbiter Neutral Mass Spectrometer
PVO	Pioneer Venus Orbiter
RWD	Reaction Wheel Data
SZA	Solar Zenith Angle (degrees)
$T_{\infty}$	Exospheric temperature (K)
$T_{100}$	Hedin model base altitude temperature at 100 km (K)
$T_{115}$	VIRA model base altitude temperature at 115 km (K)
$T_{BC}$	Temperature at the number density boundary condition at 150 km (K)
$T_j$	Temperature at the junction altitude at 143.9 km (K)
VIRA	Venus International Reference Atmosphere



## **I. INTRODUCTION**

### **1.1 Overview**

The Venus International Reference Atmosphere (VIRA) model<sup>1</sup> is a mathematical representation of temperature, constituent composition, and density of the Venus upper atmosphere. A detailed chronological history of Venus upper atmospheric models is offered in Section II. Of these models the VIRA model is recognized as the official model that represents the Venus upper atmosphere. The most important aspect that these models have in common is that the data used to define these models was restricted to low latitudes, i.e. latitudes less than 20°. Not until the final stages of the Magellan mission, when the periapsis of the spacecraft moved into northern mid latitudes, was drag data recorded with latitude exceeding 20°. Reduction of reaction wheel torque telemetry data<sup>2</sup> from the Magellan spacecraft resulted in atmospheric density measurements over wider latitudinal coverage than drag data. Reaction wheel data are density measurements of the Venus atmosphere determined by changes in the speed of the reaction wheels in the Magellan control system while taking into account known spacecraft properties such as spacecraft center of mass, spacecraft orientation and frontal area, and momentum accommodation coefficients. The mid latitude drag data and reaction wheel data provide an opportunity to use density data at mid and high latitudes to redefine coefficients for the VIRA model. The new coefficients will provide for more accurate latitudinal and solar activity variations in the model.

## **1.2 Purpose of This Study**

The purpose of this research is to apply previously unused Magellan drag data and Magellan reaction wheel data to update VIRA model coefficients. To distinguish the different types of density data used in this research, density measurements derived from traditional orbital decay techniques are subsequently referred to as drag data and density measurements derived from aerodynamic torques applied to the spacecraft recovered from the Magellan spacecraft control system reaction wheel rates are subsequently referred to as reaction wheel data. A more detailed discussion of data is offered in Section III. The data is analyzed using a minimum variance method discussed in Section IV which updates coefficients most relevant to be changed by the new data. The coefficients updated by this research include the Orbital Neutral Mass Spectrometer (ONMS) sensitivity parameters for CO<sub>2</sub>, and O derived from atmospheric drag. The sensitivity parameter for O is assumed to also apply to CO, N, and N<sub>2</sub>. Other parameters include the He sensitivity parameter; mean T<sub>∞</sub>; ten spherical harmonics for T<sub>∞</sub>; long-term and short-term day-side solar activity parameters for T<sub>∞</sub>; night-side long-term solar activity parameter for T<sub>∞</sub>; and day-side long-term solar activity parameters for CO<sub>2</sub> and O. The purpose of this research is to use all available data in the minimum variance procedure to find coefficients for an atmospheric model representative of latitudinal and solar activity variations.

### **1.2.1 Aspects of the Research**

The research can be thought of as involving three different, yet interrelated elements: the model, the data, and the minimum variance procedure to minimize the

difference between the model and the data. Assumptions made in solution parameters for any one of these elements can have significant side effects on the final results. To ensure consistency with previous models, special attention was paid to the VIRA model structure in the region of previous measurements. Different results are obtained when solving for models which define symmetric or asymmetric  $T_{\infty}$  with respect to Local Solar Time (LST) and Solar Zenith Angle (SZA). Inclusion and exclusion in various combinations of reduced data from the Pioneer Venus Orbiter (PVO) and Magellan used by the minimum variance procedure will affect the final results. Cases were run for this research which produce results using only drag data and using combined drag and reaction wheel data. The minimum variance procedure can yield different converged sets of coefficients depending on the utilization of predetermined data weighting and a priori coefficients.

### **1.2.2 Organization**

The organization of the rest of this thesis is as follows. Section II will discuss the VIRA model structure, equations, and validation with respect to previously published atmospheric models. Section III highlights the diversity and limitations of both drag data and reaction wheel data. Section IV discusses the differential correction procedure used to update specified VIRA model coefficients. Section V presents several sets of coefficients. Section VI discusses issues regarding the model, the data, and the solution coefficients which need to be resolved. Section VII presents final conclusions regarding this research.

### 1.2.3 Terminology

This section is provided to alleviate confusion regarding references within this paper to atmospheric models and model coefficient sets. Although other atmospheric models are discussed in this paper, this research concentrates specifically on the VIRA model. When the mathematics and structure of the VIRA model published in 1985 are discussed in this research the term "VIRA model" is used. This research updates model coefficients not the mathematical form of the model. Instances arise throughout this paper where there is a need to discuss and compare specific coefficient sets. For these instances the structure of the model remains unchanged for all coefficient set discussions or comparisons. Thus only the coefficients used in the VIRA model account for differences in temperature and density. There is one final important footnote regarding the implementation of the VIRA model in this research. The VIRA model published in 1985 is symmetric with respect to SZA in both temperature and composition. This research follows conventions adopted in the 1993 paper by Keating and Hsu<sup>4</sup> where the composition is asymmetric with respect to SZA.

## **II. VIRA Model**

First an overview of the history of Venus atmospheric models is presented. Different elements from the Hedin<sup>3</sup>, VIRA<sup>1</sup>, and KH<sup>4</sup> models are incorporated in the VIRA model used in this research. Then a discussion of boundary conditions and temperature profiles which comprise the VIRA model. Next a listing of the equations defining VIRA model. Finally, verification is presented showing that the model used in this research is consistent with previously published models.

### **2.1 History**

The Venus International Reference Atmosphere thermospheric model<sup>1</sup> is a mathematical representation of temperature, composition, and density of the thermosphere and exosphere of Venus. The origins of the VIRA model comes from two papers one by G. M. Keating et al.<sup>5</sup> and the other by A. E. Hedin et al.<sup>3</sup>. The Keating et al. paper presents the 1980 Orbiter Atmospheric Drag (OAD) model using data retrieved from the Pioneer Venus Orbiter Atmospheric Drag Experiment. The OAD model derived from reduced PVO drag data provides estimates of atmospheric density, temperature, and composition for low latitudes, altitudes from 140 km to 190 km, and any local solar time. The OAD model does not include any variation with solar activity.

The Venus Empirical Thermospheric Model<sup>3</sup> was published by A. E. Hedin et al. in 1983 and is subsequently referred to as the Hedin model in this paper. The Hedin model used PVO Orbiter Neutral Mass Spectrometer (ONMS) data to construct an analytical model primarily valid for calculations at low latitudes where all ONMS measurements were taken. The Hedin model temperature vertical structure is represented

by three Bates<sup>6</sup> profiles which have a base altitude of 100 km above the surface of Venus. Bates temperatures profiles permit closed form solutions of the hydrostatic equation to determine density changes with respect to altitude. The six constituent gases assumed present in the Venus atmosphere by the Hedin model include: carbon dioxide: (CO<sub>2</sub>), monatomic oxygen: (O), carbon monoxide: (CO), helium: (He), atomic nitrogen: (N), and molecular nitrogen: (N<sub>2</sub>). Each number density is determined by the integration of independently determined mixing and diffusive separation contributions with respect to altitude along three different Bates profiles. Once each constituent number density is determined, total atmospheric density can then be estimated. The Hedin model provides estimates over all local solar times and an altitude range from 100 to 250 km. The Hedin model also includes solar activity variations. The VIRA model in this research has composition boundary conditions at 150 km similar to the Hedin composition boundary conditions.

The OAD model and Hedin model used similar temperature structures in that temperatures were defined differently for the day-side than for the night-side of the planet. This is due to the presence of a cryosphere<sup>7</sup> on the night-side of Venus where temperature drops with increasing altitude as opposed to the day-side thermosphere where temperature increases with altitude.

The results from Keating<sup>5</sup> and Hedin<sup>3</sup> papers were combined and refined resulting in the VIRA model<sup>1</sup>. The VIRA model, published in 1985, is largely consistent with the Hedin model. However, the VIRA model differed from the Hedin model in three ways. The VIRA model used a spherical harmonic expansion function for  $T_{\infty}$  that is only a function of SZA. This makes  $T_{\infty}$  diurnally symmetrical before and after 1200 LST.

Hedin's expansion function for  $T_{\infty}$  is asymmetric with respect to SZA. The VIRA model also incorporated a simplified temperature profile and introduced hydrogen as an additional constituent. The VIRA paper presents a model for the Venus upper atmosphere from altitudes from 100 km up to 3500 km, where 'hot' species prevail. The VIRA model is also based on low latitude data taken over all local solar times and includes solar activity variations. The VIRA model in this research employs the mathematical representation of temperature profiles defined in the VIRA paper.

In 1992-1993 the PVO and Magellan spacecraft provided new drag data. These measurements were taken during a period of medium to low solar activity contrasting with measurements taken by PVO in 1978-80 during a period of high solar activity. Drag data retrieved from PVO in 1992 and Magellan in 1992 and 1993 in comparison with earlier results established improved representation of solar activity variations. Keating and Hsu published a paper<sup>4</sup> in 1993 which discussed improved representation of solar activity variations for the VIRA model, referred to subsequently as KH 93. Changes in the KH 93 from VIRA include: the addition of a night-side long-term solar activity parameter in  $T_{\infty}$  and O expansion functions (see Section 2.3); the update of day-side long-term and short-term solar activity parameters in the  $T_{\infty}$ ,  $\text{CO}_2$ , and O expansion functions; the update coefficients of the asymmetric  $T_{\infty}$  expansion function; and the elevation of the base altitude of the model to 115 km from 100 km. The VIRA model in this research incorporates the changes made by the KH 93 model by raising the base altitude of the model to 115 km and using the night-side solar activity coefficient<sup>4</sup>.

## 2.2 Boundary Conditions and Temperature Vertical Structure

The VIRA model is symmetric with respect to latitude and can be symmetric or asymmetric with respect to LST depending on the use or non-use of latitudinal spherical harmonics. The VIRA model is defined by nine boundary conditions and three temperature profiles. The temperature profiles used in this research are those defined in the VIRA paper<sup>1</sup>. The boundary conditions include two temperature boundary conditions, one for  $T_{\infty}$  and one temperature at the base of the model at 115 km ( $T_{115}$ ). The  $T_{\infty}$  boundary condition is adopted from the expansion function laid out by Hedin<sup>3</sup>. The  $T_{115}$  boundary condition remains unchanged from those given in Keating and Hsu<sup>4</sup>, and is provided in Table A.2 in Appendix A. The rest of the boundary conditions are constituent number densities for  $\text{CO}_2$ , O, CO, He, N,  $\text{N}_2$ , and H determined at 150 km. The H number density boundary condition at 150 km is provided in Appendix A, Table A.2. The number density boundary conditions are consistent with the Hedin model<sup>3</sup> at 150 km except for the number density multiplier constants or ONMS sensitivity parameters which make mass spectrometer data consistent with drag data.

Figure 1 shows an example of temperature profiles for the VIRA model.  $T_{\infty}$  is defined by a spherical harmonic expansion and solar activity parameters.  $T_{\infty}$  is assumed to be dependent only on latitude, LST, daily solar activity, and 81 day mean solar activity.  $T_{115}$  is only a function of LST. Note that  $T_{115}$  exclusive dependence on LST causes a discontinuity at the poles. This discontinuity has not been addressed due to the fact that all recorded density measurements occur at latitudes below  $80^{\circ}$ . The model could be modified such that when model predictions are required above  $80^{\circ}$  latitude the value of

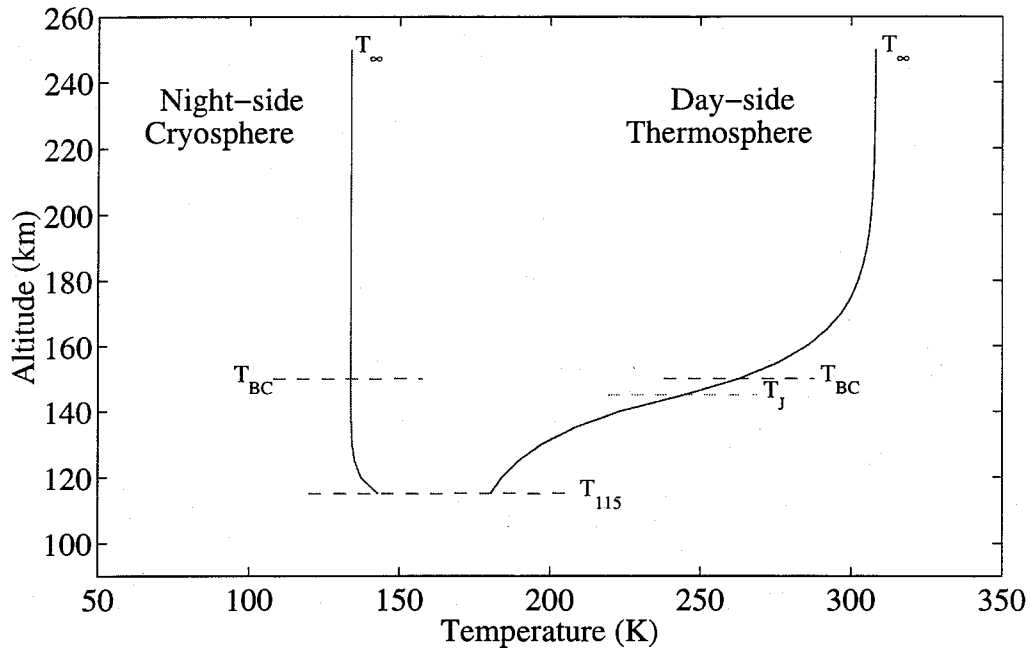


Figure 1 : VIRA model midnight and noon temperature profiles

$T_{115}$  approaches the value of  $T_{115}$  at the terminator which is 161.5 K. The temperature vertical profile on the day-side is different for that on the night-side. The day-side thermospheric temperature profile is made up of two Bates curves. The bottom profile defines temperature from the 115 km to the junction altitude at 143.9 km. The temperature at 143.9 km is the average of  $T_{\infty}$  and  $T_{115}$ . The upper profile defines temperature from 143.9 km to up above 200 km and approaches  $T_{\infty}$  asymptotically. Temperature above 200 km tends to change by less than 1% of  $T_{\infty}$ .

The night-side cryosphere<sup>7</sup> profile consists of only one Bates curve. As altitude increases on the night-side of the planet the temperature decreases and approaches the colder night-side  $T_{\infty}$ , which is lower than  $T_{115}$ . The decision to use the day-side or night-side profile for density calculation is determined by whether or not the exospheric temperature is greater than  $T_{115}$ . If  $T_{\infty}$  is determined to be greater  $T_{115}$ , the day-side

profiles are used. Conversely, if exospheric temperature is lower than  $T_{115}$ , the night-side profile is used. Note this condition may allow a nearly isothermal atmosphere to occur.

Figure 2 shows Hedin's model's temperature profiles for comparison to the simpler VIRA temperature profiles. Hedin day and night temperature profiles consist of three Bates variations. The Hedin model determines  $T_{\infty}$  similarly to the VIRA model. The temperature at 100 km is defined by Hedin as constant for the entire planet. The junction temperature at 140 km is a complicated calculation dependent on  $T_{\infty}$  and two other parameters defined by spherical harmonics which were eliminated from the VIRA model. The lower and upper Bates variations are similar to the VIRA day-side profile. The third variation deviates from the lower profile at below 140 km and joins the upper profile above the junction altitude.

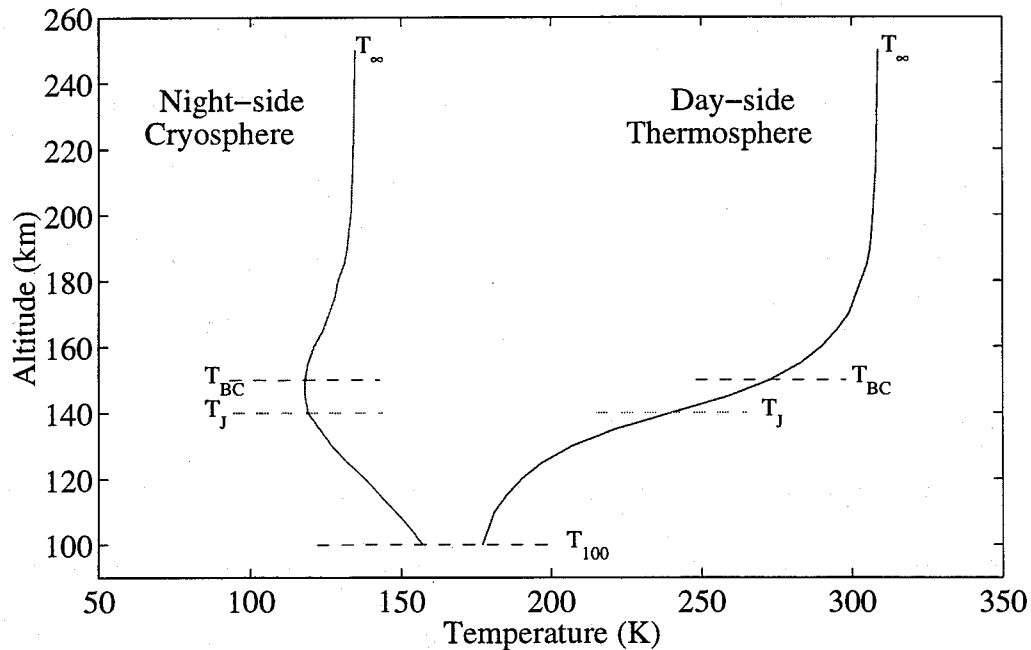


Figure 2 : Hedin model noon and midnight temperature profiles

All the composition number densities for the VIRA model and other published models are defined at 150 km. Except for hydrogen, the number densities are defined in a similar manner to the  $T_{\infty}$  expansion function which is dependent on latitude, LST, daily  $F_{10}$  solar activity, and 81 day mean  $F_{10}$  solar activity. Atomic hydrogen is defined only as a function of LST (see Table A.1 in Appendix A). The same mathematical discontinuity for hydrogen occurs at the poles as does for  $T_{115}$  and should be handled similarly. Once the boundary conditions are determined, determination of total density is assumed to be governed by diffusive separation, even if the altitude for which density is determined is lower than 150 km. To determine the total density at any altitude, each number density is determined in accordance with the appropriate day or night temperature profile and altitude change and the partial densities of individual species are summed together for the total density.

### **2.3 Equations**

The following is a detailed sequential list of equations and variables used in the VIRA model. These equations defining the VIRA model have been pieced together from several sources and reflect all the equations and calculations necessary, except the equations that define number densities at the 150 km boundary condition, to produce density predictions in the Venus upper atmosphere. Equations needed to define number density boundary conditions at 150 km are described in full detail in the Hedin paper<sup>3</sup> and take into account both diffusive separation and mixing contributions for each constituent.

### Model Inputs:

$\tau$	=	Local solar time
$\theta$	=	Colatitude
$\chi$	=	Solar zenith angle
$F_{10.7}$	=	Solar activity*
$\bar{F}_{10.7}$	=	Mean solar activity*
$h$	=	Geocentric altitude

\*Note that solar activity and mean solar activity are 10.7 cm solar flux measurements made at the Earth but are compensated in the direction of Venus by using time weighted averaging of the Sun's 27 day rotation at the distance of Earth from the Sun.

### Boundary/Junction Altitudes:

$h_L$	=	Base altitude of constituent densities of the model
$h_j$	=	Junction altitude of Bates profiles

### Geopotential Altitude Conversion:

$$z = (h - h_L)(R_p + h_L)/(R_p + h)$$

where:  $R_p$  = Radius of Venus\*\*

\*\*Note that radius of Venus used in VIRA model is 6053 km. However, the Magellan Navigation team used 6054 km as the radius of Venus.

### Legendre Polynomials used in Harmonic Expansion Function:

Use solar zenith angle to determine zonal harmonic expansion

$$P_n^0(\cos(\chi))$$

Use colatitude to determine sectoral harmonic expansion

$$P_n^n(\cos(\theta))$$

Model uses explicit Legendre Polynomial functions for appropriate zonal ( $P_n^0$ ) and sectoral ( $P_n^n$ ) harmonic expansions.

### Boundary Conditions for VIRA Model:

$T_{115}$  = Base temperature at 115 km. Note:  $T_{115}$  is a function of local solar time and determined by linear interpolation of values from a list of temperatures. See Appendix A Table A.2.

$T_\infty$  = Exospheric temperature

$$T_\infty = \bar{T}_\infty [1 + G(\theta, \tau, F_{10.7}, \bar{F}_{10.7})]$$

$n_k$  = Number densities for constituents k determined at 150 km

$n_H$  = Number density for hydrogen at 150 km. Note:  $n_H$  is a function of local solar time by linear interpolation between hourly values of hydrogen number densities. See Appendix A Table A.1.

Spherical Harmonic Expansion Function:

$$G(\theta, \tau, F_{10.7}, \bar{F}_{10.7}) = (\hat{f} + \bar{f})(\bar{F}_{10.7} - 200) + f(F_{10.7} - \bar{F}_{10.7}) \\ + F_c \sum_n^5 [a_{n0} P_n^0(\cos(\chi)) + b_{nn} P_n^n(\cos(\theta)) \sin(n\omega\tau)]$$

- where:  $f$  = Day-side daily  $F_{10.7}$  response coefficient  
 $\bar{f}$  = Day-side 81 day  $F_{10.7}$  response coefficient  
 $\hat{f}$  = Night-side 81 day  $F_{10.7}$  response coefficient  
 $F_c$  = Solar activity multiplier  
 $\omega$  =  $2\pi/24$  hours to radians conversion multiplier  
 $a_{n0}$  = Zonal Legendre polynomial coefficients  
 $b_{nn}$  = Sectoral Legendre polynomial coefficients

Solar Activity Multiplier:

$$F_c = 1 + \frac{\bar{f}(\bar{F}_{10.7} - 200) + f(F_{10.7} - \bar{F}_{10.7})}{a_{10} - a_{20} + a_{30} - a_{40} + a_{50}}$$

Solar Zenith Angle:

$$\cos(\chi) = \sin(\theta)\cos(\omega(\tau-12))$$

Exospheric Temperature Night-side Solar Activity Coefficient:

$$\hat{f} = \alpha \tan^{-1}((\tau - 19)\beta) / \tan^{-1}(5\beta) \quad \text{when } 19 \leq \tau < 24 \\ \hat{f} = \alpha \tan^{-1}((5 - \tau)\beta) / \tan^{-1}(5\beta) \quad \text{when } 0 \leq \tau \leq 5 \\ \hat{f} = 0 \quad \text{when } 5 < \tau < 19$$

- where:  $\alpha$  = primary parameter for night-side solar activity response  
 $\beta$  = secondary parameter for night-side solar activity response

Note: Even though a variable  $\beta$  term is provided for in these equations, the current model assigns  $\beta = 1$

Temperature Profile:

when  $T_\infty \geq T_{115}$  Day-side Temperature Profile

$$T(z) = T_\infty - (T_\infty - T_{z_j})\exp[-\sigma_1(z-z_j)] \quad \text{when } z \geq z_j \\ T(z) = T_L - (T_L - T_{z_j})\exp[\sigma_2(z-z_j)] \quad \text{when } 115 \leq z \leq z_j \\ T_L = \{T_{115} + 0.5T_\infty\exp[\sigma_2(115-z_j)]\} / \{1 + 0.5\exp[\sigma_2(115-z_j)]\}$$

where:  $z$  = Geopotential altitude for prediction  
 $z_j$  = Junction altitude of day-side temp profile  
 $\sigma_{1,2}$  = Day-side (upper/lower) inverse scale height ( $\sigma_1 = \sigma_2 = 0.069$ )  
 $T_{z_j}$  = Junction altitude temperature =  $(T_L + T_\infty)/2$   
 $T_L$  = Lower boundary temperature for day-side profile

when  $T_\infty \leq T_{115}$  Night-side Temperature Profile

$$T(z) = T_\infty - (T_\infty - T_{115})\exp[-\sigma_n(z-115)]$$

where:  $\sigma_n$  = Night-side inverse scale height ( $\sigma_n=0.2$ )

### Constituent Density Estimates at 150 km

Number densities are calculated using equations presented in Hedin's paper<sup>3</sup>. The VIRA model uses Hedin's involved calculations to produce constituent number densities at 150 km. These calculations include separate mixing and diffusive profiles which are combined to determine conditions at 150 km. Then the model assumes an atmosphere in diffusive equilibrium for use with a Bates temperature profile for further density calculations. Note that Hedin's equations are used for calculating number densities at 150 km. When reviewing Hedin's 83 paper one should view occurrences of 'z' in the equations not as varying altitudes but as a constant 150 km.

### Density Profile:

$$n'_k = n_k K_k \rho_B \left( \frac{T_{zd}}{T} \right)^{1+\alpha_k}$$

- where:  $n'_k$  = Number density for constituent k at altitude z  
 $n_k$  = Boundary condition number density for constituent k  
 $K_k$  = Number density ONMS sensitivity multiplier  
 $T_{zd}$  = Temperature at altitude  $z_d$   
 $T$  = Temperature at altitude z  
 $\alpha_k$  = Thermal diffusivity coefficient for constituent k (Note that model uses  $\alpha_{He} = -0.6$  and zero for other constituents)  
 $\rho_B$  = Bates analytical integration multiplier

when  $T_\infty \geq T_{115}$  (Day-side Profile)

when  $z \geq z_j$

$$\rho_B = [T(z_d) / T(z)]^{\gamma_{2k}} \exp[\sigma_1 \gamma_{2k} (z_d - z)]$$

when  $115 \leq z < z_j$

$$\rho_B = [T(z_d) / T(z_j)]^{\gamma_{2k}} \exp[\sigma_1 \gamma_{2k} (z_d - z_j)] * [T(z_j) / T(z)]^{\gamma_{2k}} \exp[\sigma_2 \gamma_{1k} (z - z_j)]$$

when  $T_\infty \leq T_{115}$  (Night-side Profile)

$$\rho_B = [T(z_d) / T(z)]^{\gamma_{2k}} \exp[\sigma_n \gamma_{2k} (z_d - z)]$$

where:  $T(z_d)$  = Temperature at base density altitude

$\sigma_1$  = Upper day-side inverse scale height ( $\sigma_1=0.069$ )

$\sigma_2$  = Lower day-side inverse scale height ( $\sigma_2=0.069$ )

$\gamma_{1k}, \gamma_{2k}$  = Model parameter reflecting constituent(k) molecular weight

k = Represents constituent species

$\sigma_n$  = Night-side inverse scale height ( $\sigma_n=0.2$ )

Gamma parameters:

$$\gamma_{1k} = MW_k g_d / (\sigma_1 R_g T_{115})$$

$$\gamma_{2k} = MW_k g_d / (\sigma_2 R_g T_\infty)$$

$$g_d = g_s / (1 + h_d / R_p)^2$$

- where:  $\gamma_k$  = Parameter reflecting constituent(k) molecular weight  
 $MW_k$  = Molecular weight of constituent  
 $g_d$  = Gravity at base density altitude  
 $g_s$  = Gravity at surface of Venus (0.008874 km/s<sup>2</sup>)  
 $R_g$  = Universal gas constant (0.008314 g·km<sup>2</sup>/mol·s<sup>2</sup>deg)

Total density:

$$\rho = \sum_k n_k MW_k / A$$

- where: k = Represents constituent species  
 $n_k$  = Number density for each constituent  
 $MW_k$  = Molecular weight for each constituent  
A = Avogadro's number (6.02x10<sup>23</sup>)

Note: output density from model is usually in log<sub>10</sub>(ρ).

## 2.4 Verification

Model verification is limited given the few published tables of information that are available. The following tables show the values of total density(g/cm<sup>3</sup>), number densities(cm<sup>-3</sup>) and temperature(K) at 150 km from tables given in Hedin's paper<sup>3</sup> and those corresponding values produced by the model using Hedin's coefficients (sensitivity parameters are properly adjusted to reflect the Hedin model):

Source	ρ	CO <sub>2</sub>	O	CO	He	N	N <sub>2</sub>	Temp
Table	9.68E-13	8.27E9	5.54E9	3.25E9	7.08E6	8.06E7	1.37E9	273
Output	9.67E-13	8.26E9	5.53E9	3.25E9	7.08E6	8.06E7	1.37E9	263

Table 1: Comparison of Hedin table and output values at noon on equator for F<sub>10</sub>=200

Source	ρ	CO <sub>2</sub>	O	CO	He	N	N <sub>2</sub>	Temp
Table	2.82E-14	6.29E7	7.07E8	5.71E9	1.44E7	4.74E6	4.14E7	118
Output	2.82E-14	6.28E7	7.06E8	5.70E7	1.44E7	4.73E6	4.14E7	134

Table 2: Comparison of Hedin table and output values at midnight on equator for F<sub>10</sub>=200

Clearly, the constituent results are essentially the same. The difference in temperatures is attributed to the different temperature profiles used in the VIRA model than in the Hedin model. The following tables show the values of total density( $\text{g/cm}^3$ ), number densities( $\text{cm}^{-3}$ ) and temperature(K) at 150 km given values from tables in the VIRA paper<sup>1</sup> compared to those produced by the model using VIRA coefficients (sensitivity parameters are properly adjusted to reflect the VIRA model):

Source	$\rho$	CO <sub>2</sub>	O	CO	He	N	N <sub>2</sub>	Temp
Table	9.94E-13	9.81E9	4.00E9	2.34E9	5.01E6	4.65E7	1.32E9	246.5
Output	9.93E-13	9.80E9	4.00E9	2.33E9	5.01E6	4.64E7	1.32E9	247.3

Table 3: Comparison of VIRA table and output values at noon at 16° lat. for  $F_{10}=150$

Source	$\rho$	CO <sub>2</sub>	O	CO	He	N	N <sub>2</sub>	Temp
Table	3.42E-14	7.10E7	8.51E8	7.24E7	1.89E7	5.80E6	5.91E7	127.4
Output	3.42E-14	7.09E7	8.50E8	7.25E7	1.88E7	5.79E6	5.91E7	127.6

Table 4: Comparison of VIRA table and output values at midnight at 16° Lat. for  $F_{10}=150$

Again the results are nearly the same. All model values are within 0.5% of one another. The results of the VIRA model using VIRA coefficients satisfactorily match results given in papers which originally defined the VIRA model after compensating for different ONMS sensitivity multipliers derived from drag data. Tables for hydrogen and T<sub>115</sub> boundary conditions and plots of temperature, density, and composition of constituent species of the VIRA model are provided in Appendix A.

### **III. Data**

#### **3.1 Overview**

This section gives an overview of the three fundamental types of data used to update the VIRA model. The three types of data include: drag data from retrieved by PVO during the main mission in 1978-1980 and towards the end of the extended mission in 1992; drag data from the Magellan spacecraft during its extended mission from 1992-1994 during Cycles 4,5 and 6; and reaction wheel data from Magellan during Cycles 5 and 6 during 1993 and 1994.

##### **3.1.1 Pioneer Venus Orbiter Characteristics**

The Pioneer Venus Orbiter(PVO) spacecraft<sup>8</sup>, also referred to as Pioneer 12, was launched on May 20, 1978. On December 4, 1978 PVO was inserted into a highly elliptical orbit around Venus with a inclination of 105°. The orbital period was 23 hours and 11 minutes. The lowest periapsis of the PVO spacecraft during the primary mission was about 150 km while the apoapsis remained around 66,000 km until the end of the mission. The orbital orientation allowed mass spectrometer and atmospheric drag measurements to be made near periapsis of each orbit. The mass spectrometer data were used to determine number density boundary conditions<sup>3</sup> for six major constituents at 150 km. The drag data led to the development of the VIRA model<sup>1</sup> published in 1985. The drag measurements taken by PVO during the first years of the mission were during a period of high solar activity. In 1992, PVO was used to take more drag measurements during a period of medium to low solar activity for comparison with previous results which resulted in better understanding of solar response of the Venus atmosphere<sup>4</sup>. With

an exhausted fuel supply, Pioneer Venus ended its 14 year mission on October 8th, 1992 by entering the Venus atmosphere.

### **3.1.2 Magellan Spacecraft Characteristics**

The Magellan<sup>9</sup> spacecraft was the first planetary spacecraft to be carried into orbit by a shuttle when the space shuttle Atlantis was launched from Kennedy Space Center on May 4, 1989. A solid rocket motor upper stage was then used to send Magellan on its 15 month journey to Venus. On August 10, 1990 Magellan was initially placed into a highly elliptical polar orbit with a periapsis of 294 kilometers and apoapsis of 8,543 kilometers with an orbital period of 3 hours and 15 minutes. During the first three cycles of the Magellan mission, Magellan performed scientific experiments which initially did not provide for the collection of drag data. A cycle refers to the 243 Earth-day sidereal period of Venus. During Cycle 4 of the mission, Magellan was dropped into the Venus atmosphere to make a diurnal survey of the atmosphere before aerobraking and also to study detailed characteristics of the gravity field. The Doppler effect was determined from radio waves returning from Magellan to establish orbit decay and gravity field characteristics. Drag measurements were made and used to update VIRA for Magellan Operations. After Cycle 4, from May 25th to August 3 1993, Magellan became the first planetary spacecraft to use an aerobraking procedure to nearly circularize the orbit. The KH 93 model coefficients were used to estimate densities for Magellan aerobraking operations. Aerobraking was successfully performed lowering apoapsis to 541 km. The orbital period after aerobraking was 94 minutes. Drag and reaction wheel measurements

continued to be made during Cycles 5 and 6 until the termination experiment<sup>10</sup> on October 11th, 1994.

### **3.1.3 Reaction Wheel Data Characteristics**

The reaction wheel method to obtain density measurements originated from a feasibility study by Marsden<sup>11</sup> to develop a complimentary technique to the orbital decay method<sup>12</sup> to determine atmospheric densities. Magellan spacecraft properties needed to perform this alternate technique were determined by Croom as extended results to the feasibility study<sup>13</sup>. These properties were used to reduce telemetry data from Magellan's reaction wheels to determine densities using a least squares fit performed during research by Espiritu<sup>2</sup>. Magellan's reaction wheels are used to keep the spacecraft inertially fixed even when flying through the atmosphere. While passing through the atmosphere, changes in the Magellan control system reaction wheel rates correspond to aerodynamic torques applied to the spacecraft. In turn these aerodynamic torques can be used to estimate atmospheric densities. Density results obtained in this manner are referred to as reaction wheel data (RWD). RWD passes consist of up to 30 measurements for a single orbit spread over almost 90 degrees of latitude which start close to the north pole as the spacecraft approaches periapsis and run south through periapsis and again out of the atmosphere. Density measurements altitudes for RWD passes, characteristically, begin around 260 km and descend to periapsis and then increase up to 260 km again as the satellite moves away from the planet. For use in the minimum variance method, all RWD above 220 km was removed from consideration because of low signal to noise ratios. Most of these orbits occurred at local solar times ranging from 1100 on the planet to just

across 1800 LST. Since Magellan was in a polar orbit, all density measurements obtained during single RWD passes are tagged at the same LST. Similarly, since RWD measurements are recorded within 10 minutes before and after periapsis, each RWD pass is tagged with the same short-term and long-term solar activities. Each RWD pass density measurements with all associated standard deviations (as the error bars) are shown versus latitude in Appendix D after the drag data plots. For comparison with the data, the one step SZA model (solid line) and the VIRA model (dashed line) are presented.

### 3.2 Summary

The following section summarizes details of all the drag and reaction wheel data sets that were used to obtain results. The drag data were divided into seven distinct sets depending on when the data was retrieved and by which satellite. This convention was adopted from previous research<sup>4</sup>. The following table shows maximum and minimum periapsis altitudes, periapsis latitudes, and  $F_{10.7}$  solar indices for each drag data set:

Data Range	Min Alt	Max Alt	Min Lat	Max Lat	Min F10	Max F10
PVO(78-80) pt. 1	142.70	189.00	16.00	16.00	123.63	210.43
PVO(78-80) pt. 2	143.00	187.40	16.00	16.00	129.93	260.24
PVO (92)	130.20	211.40	-11.00	-11.00	104.00	139.40
Magellan Cycle 4	169.60	190.70	10.40	11.40	90.80	117.70
Magellan Aerobrake	136.40	164.50	10.70	13.90	85.40	141.60
Magellan Cycle 5	157.48	208.84	10.90	31.20	82.50	128.70
Magellan Cycle 6	168.45	211.26	11.50	47.80	70.60	96.30

Table 5 : Data subset ranges for periapsis altitudes, latitudes, and solar activities

As the table indicates, the majority of drag pass data occurs at low latitudes. A small portion of drag measurements were taken at higher latitude towards the end of the Magellan mission during Cycle 5 and Cycle 6. Though not shown each set of the drag

data are well distributed in LST except for drag density data retrieved during Magellan aerobraking and during PVO measurements taken in 1992. Unfortunately, reaction wheel data orbits do not provide for a good distribution of LST since most of these orbits occur between 1100 and 1800 LST. A criterion was used to remove outlying measurements from consideration. This criterion was developed iteratively. First, all the data was used to determine new coefficients for the model. Next, all reaction wheel measured densities which had a percent error of more than 100% from the model were removed. Finally the data which satisfied all the filtering criterion were included in the final data set seen in

Figure 3:

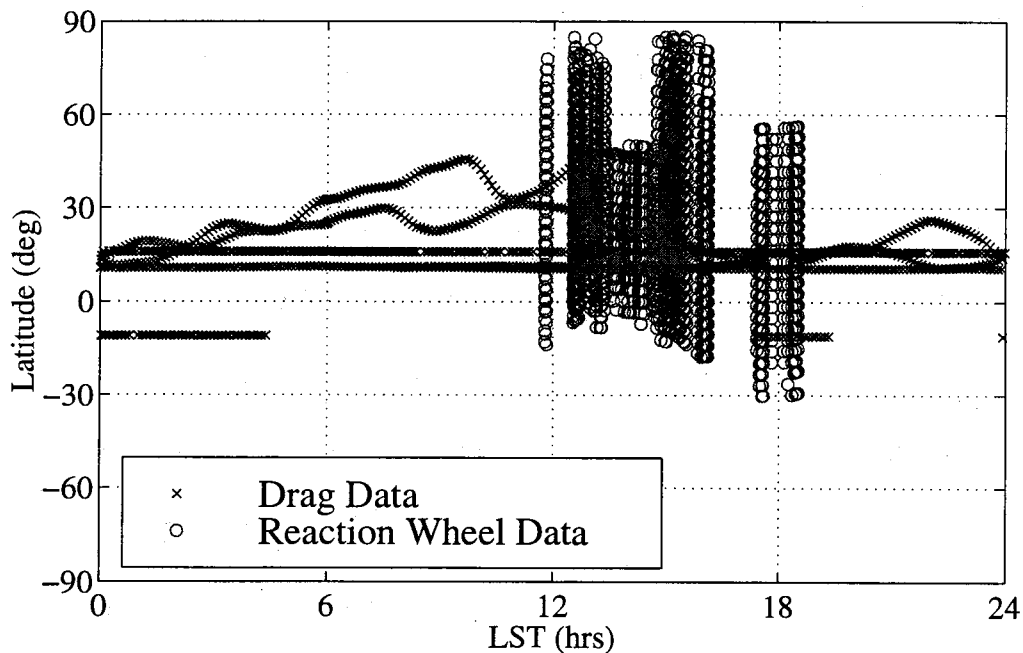


Figure 3 : Distribution of data with respect to latitude and LST

Changes between successive drag pass measurements have small changes in local solar time and minimal changes (or no change) in latitude. Reaction wheel data taken during a single pass are recorded at the same LST and rapidly change in latitude from

North to South as the satellite passed through periapsis. It should be noted that only 471 drag measurements from PVO and Magellan occur between 1100 and 1900 LST, where all of the reaction wheel data measurements are recorded.

Due to the fact that RWD outnumbered drag data 2 to 1 and does not have full coverage of LST, standard deviations associated with RWD measurements have been arbitrarily multiplied by a factor of four to reduce imbalance of the solution. This was found to be necessary when preliminary results showed obvious imbalances due to the over emphasis on RWD. By raising the standard deviations of the RWD, the RWD is weighted down to allow drag data to primarily shape the model with respect to SZA and have RWD still provide latitudinal variation in the  $T_{\infty}$  spherical harmonic terms. This result may suggest the model is over-parameterized based on available data.

### **3.3 Determination and Analysis of Reaction Wheel Data Bias**

Even though the existence of a bias between drag data and RWD was theorized, the bias was not detected until preliminary results were obtained. While determining weighted mean error of the initial results, the mean errors were not as close to zero as one would expect from a differential correction solution. It was concluded that the reason for this was that the RWD measurements did not agree with the drag data measurements.

The first step in determining the constant bias between RWD and drag densities was to find any orbits on which density was measured using both methods. Only seven such orbits coincided between available drag data and RWD. To correctly interpret these densities one must compensate for the different altitudes at which these measurements are tagged. The RWD densities used for this analysis are direct measurements of density at

the periapsis of the respective orbits. The value for drag densities are provided at 1/2 scale height above periapsis to minimize the solution sensitivity to assumed scale height<sup>12</sup>. The hydrostatic equation was used to correctly interpret RW densities at drag density altitudes. As suspected, these ratios were not uniformly one. The mean of these seven ratios is 1.3 although the values vary significantly. Figure 4 displays the seven density ratios.

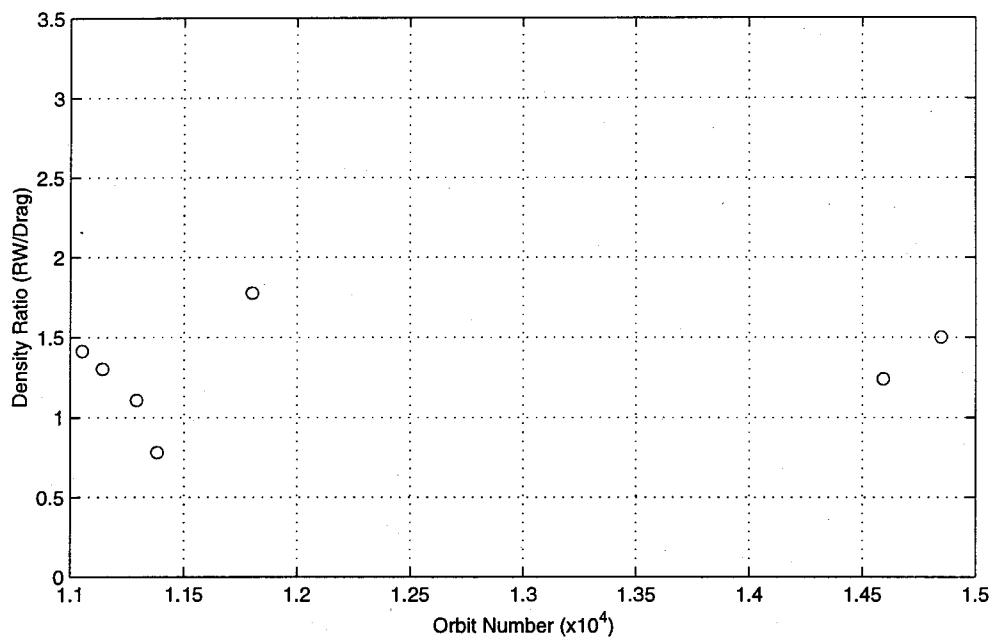


Figure 4 : Coincident RWD and drag data

Since Venus has a very slow diurnal cycle the atmospheric density contributing factors vary slowly from orbit to orbit, the second step in bias determination was to compare drag measurements of orbits which were recorded within five orbits of each RWD measurement. This method provided more than 70 ratios to consider, providing confidence in the final decision for the RWD bias. Figure 5 shows the seventy density ratios versus the orbit number of the RWD measurement.

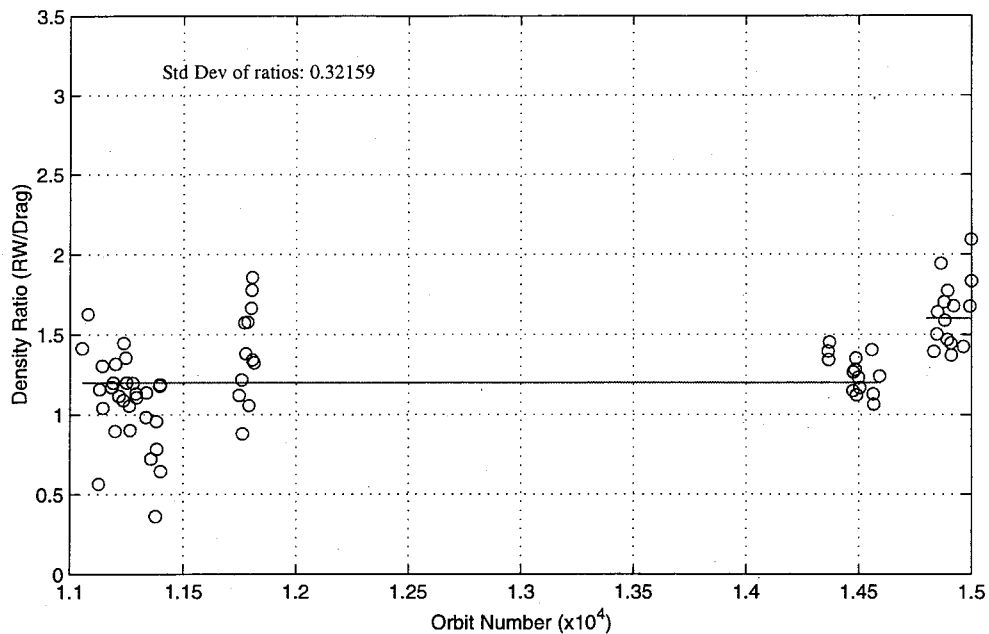


Figure 5 : Comparison of RWD and drag data within five orbits of each other

Note the mean ratios on the right side of the plot tend to be higher than those on the rest of the plot. These higher ratios all correspond to orbits close to the end of the Magellan mission. There are instances throughout the mission when the satellite's geometry was changed either due to an attempt to cool the solar panels by positioning them away from the sun or a maneuver to orient the high gain antenna toward the Earth. However, it has proved impossible to find any information from that late in the Magellan mission to confirm that such events took place. It was decided that data collected during these passes be compensated using a different constant bias than the rest of the reaction wheel orbits. To this end two biases were determined to make the RWD density measurements consistent with drag density measurements. All RWD orbit densities which occurred before orbit 14800 have been divided by the 1.2 bias and all densities in orbits after 14800 have been divided by 1.6 to make them consistent with drag densities.

## IV. Differential Correction Method

### 4.1 A Priori Differential Correction Method

A minimum variance method with a priori<sup>13</sup> was used to update model coefficients using density observations. The minimum variance method has many advantages over an unweighted least squares method. The following discussion presents several specific reasons for utilizing the minimum variance method for this investigation. The original data set, consisting of PVO measurements between 1978 and 1980, could not support the large number of parameters used in the model. Correlations between coefficients became very high leading to large biases in estimates. A priori coefficients are coefficient values assumed to be correct and can be used to constrain the solution to within reasonable estimates without increasing the standard deviation of the residuals. Minimum variance also limits the extent that data effects parameters in unrealistic ways. For example the He sensitivity multiplier was originally determined from an analysis of PVO mass spectrometer and drag measurements. A priori provides a way to not permit high latitude Magellan drag data to overly influence this parameter. A priori also allows faster solutions by conditioning the sensitivity matrix. The a priori coefficients are represented by the  $\bar{\mu}_x$  term in the equation below, and the a priori accuracy is represented by  $\Gamma_x$ . The minimum variance solution uses the standard deviation of each data point to weight all of the data according to accuracy. More accurately determined data will influence the solution more than weakly determined observations. The accuracy of the data is represented in the  $\Gamma_e$  term in the equation below. The following procedure outlines the minimum variance method:

General minimum variance with a priori differential correction equation <sup>13</sup>:

$$\Delta \bar{x}_n = (A^T \Gamma_e^{-1} A + \Gamma_x^{-1})^{-1} [A^T \Gamma_e^{-1} \bar{\epsilon} + \Gamma_x^{-1} (\bar{\mu}_x - \bar{x}_n)]$$

where:  $\Delta \bar{x}_n$  = vector of changes in estimated parameters

$\bar{x}_n$  = vector of values of estimated parameters

n = iteration index

$\bar{\mu}_x$  = vector of a priori estimates

$\bar{\epsilon}$  = vector of residuals between measured and model determined densities for all data points based on  $\bar{x}_n$

A = Sensitivity matrix ( $\partial \bar{\omega} / \partial \bar{x}$ ) represent partials of model density with respect to change in coefficient value

$\Gamma_e$  = measurement covariance matrix

$\Gamma_x$  = a priori covariance matrix

The following must be defined for the differential correction procedure:

Assign  $\bar{\mu}_x$ , the a priori estimate for each parameter

Define the data set of m data points to be used in differential corrections. Each observation contains eight parameters: Orbit # ,LST, altitude, density,  $F_{10.7}$ ,  $\bar{F}_{10.7}$ , latitude, sigma of the density measurements

Define  $\bar{x}$ , the N coefficients which are updated using the differential correction method

Define  $\Gamma_x$ , an M by M non-negative definite symmetric parameter covariance matrix generally considered to be a diagonal matrix where:  $\Gamma_x(i, i) = \sigma_{x,i}^2$   
i is an index representing an estimated parameter in the solution set

Define  $\Gamma_e$ , an N by N non-negative definite symmetric measurement covariance matrix generally considered to be a diagonal matrix where:  $\Gamma_e(j, j) = \sigma_{e,j}^2$   
j is an index representing an observation in the data set

Determine  $\delta x$ , a vector of increases/decreases to be made for each coefficient when defining the sensitivity matrix (A) by finite difference partials

Differential correction iterations are performed until the convergence criterion is satisfied. Each iteration defines  $\Delta \bar{x}_n$  which is used to obtain  $\bar{x}_{n+1}$  using the following expression  $\bar{x}_{n+1} = \bar{x}_n + \Delta \bar{x}_n$ . The convergence criterion for the differential correction is satisfied when the maximum change in any coefficient between iterations is less than

tolerance or iterations exceeds maximum iterations limit. (The tolerance was set to 0.001 to obtain results presented in Section V). Each differential corrections iteration includes the following steps:

Define  $\bar{\epsilon}$  :  $\bar{\epsilon}$  represents the vector of residuals between calculated model predictions for each observation and the actual density observations.

Define A: A represents an M by N matrix of two-sided partial derivatives

M = number of estimated parameters

N = number of observations

i = index representing the ith estimated parameter in the solution set

j = index representing the jth observation in the data set

A is created element by element by the two sided derivative:

$$A(i, j) = \left[ \rho_i(x_j + \delta x_j) - \rho_i(x_j - \delta x_j) \right] / 2 \cdot \delta x_j$$

All necessary matrices and vectors have been formed, now  $\Delta \bar{x}$  can be calculated using general minimum variance equation and then reassign  $\bar{x}_{n+1}$ . Repeat differential correction iterations until the convergence criterion is satisfied.

#### 4.1.1 Discussion of Data Weighting

The final parameter of the each observation contains a number referred to as the standard deviation of the density observation. The standard deviation is an estimate of the uncertainty of the associated individual density measurement. The values along the diagonal of the  $\Gamma_e$  matrix reflects the standard deviations for all measurements in the entire data set. The numbers stored in the  $\Gamma_e$  diagonal array weight in data considered more accurate. The weighting is determined by the ratio of the measurement sigma over the measured density. Given the fact that log density is minimized by the minimum

variance method each term of  $\Gamma_e$  is determined using the following conditions:

$$\begin{array}{ll} \text{if } \sigma_{e,i}/\rho_i < 0.05 \text{ then} & \Gamma_e(i,i) = 1.05 \\ \text{else} & \Gamma_e(i,i) = 1 + \sigma_{e,i}/\rho_i \end{array}$$

This condition assures that the minimum assumed error is 5%. For all drag density observations by PVO and Magellan  $\sigma_e$  is estimated at  $5e-16$  by analyzing published OAD data<sup>5</sup> and estimating the mean  $\sigma_e$  from the published tables. For reaction wheel density observations by Magellan  $\sigma_e$  has been calculated along with the density for each observation<sup>2</sup>. Due to concerns of the quality and distribution of the RWD the  $\sigma_e$  values have been multiplied by four so that the RWD does not dominate the coefficient solution. The density standard deviation for all drag and RWD measurements are illustrated in plot B.8 in Appendix B (note that the RWD already takes into account the factor of 4 multiplier used to reduce RWD influence on the solution).

## 4.2 Differential Correction Steps

Research by Hedin<sup>3</sup> and by G. M. Keating and N. C. Hsu<sup>4</sup> set the precedent of using three steps to redefine the coefficients solved for in this research. This "three step process" was adopted for the drag data set as well as the mass spectrometer data set because solving for all of the coefficients at once while weighting all the drag data equally did not provide for a converged solution of coefficients. Table 6 shows a list of all the coefficients updated in the three step process, the variable which represents them in the model, and which step is used to solve for which coefficient:

Description of Coefficient	Model Symbol	Step Solved
CO <sub>2</sub> ONMS sensitivity multiplier	$\kappa_{CO_2}$	1
O (CO, N, N <sub>2</sub> ) ONMS sensitivity multiplier	$\kappa_O$	1
Mean T <sub>∞</sub>	$\bar{T}_\infty$	1, 2, 3
T <sub>∞</sub> Spherical Harmonic a <sub>10</sub> (SZA)	T <sub>∞</sub> a <sub>10</sub>	1
T <sub>∞</sub> Spherical Harmonic b <sub>11</sub> (latitude)	T <sub>∞</sub> b <sub>11</sub>	1
T <sub>∞</sub> Spherical Harmonic a <sub>20</sub> (SZA)	T <sub>∞</sub> a <sub>20</sub>	1
T <sub>∞</sub> Spherical Harmonic b <sub>22</sub> (latitude)	T <sub>∞</sub> b <sub>22</sub>	1
T <sub>∞</sub> Spherical Harmonic a <sub>30</sub> (SZA)	T <sub>∞</sub> a <sub>30</sub>	1
T <sub>∞</sub> Spherical Harmonic b <sub>33</sub> (latitude)	T <sub>∞</sub> b <sub>33</sub>	1
T <sub>∞</sub> Spherical Harmonic a <sub>40</sub> (SZA)	T <sub>∞</sub> a <sub>40</sub>	1
T <sub>∞</sub> Spherical Harmonic b <sub>44</sub> (latitude)	T <sub>∞</sub> b <sub>44</sub>	1
T <sub>∞</sub> Spherical Harmonic a <sub>50</sub> (SZA)	T <sub>∞</sub> a <sub>50</sub>	1
T <sub>∞</sub> Spherical Harmonic b <sub>55</sub> (latitude)	T <sub>∞</sub> b <sub>55</sub>	1
T <sub>∞</sub> Day-side Long-term Solar Response	T <sub>∞</sub> $\bar{f}$	2
T <sub>∞</sub> Day-side Short-term Solar Response	T <sub>∞</sub> f	2
CO <sub>2</sub> Day-side Long-term Solar Response	CO <sub>2</sub> $\bar{f}$	2
O Day-side Long-term Solar Response	O $\bar{f}$	2
T <sub>∞</sub> Night-side Long-term Solar Response	T <sub>∞</sub> α	3
He ONMS sensitivity multiplier	$\kappa_{He}$	3

Table 6: Solution coefficients with respective symbols and solution step

Step 1 uses all data, day-side, night-side, and data within one hour of the terminator, to solve for coefficients which are considered global and indicated with a 1 in

column 3. Step 2 only uses day-side data between 700 and 1700 LST to determine day-side coefficients indicated by a 2 in column 3. Step 3 only uses night-side data between 1900 and 500 LST to determine night-side coefficients indicated by a 3 in column 3. The 3 step procedure is very computationally expensive and slow to converge. A comparison in converged results and relative performance of the one step and three step processes can be found in Section 5.3.4.

#### **4.2.1 List of Cases Run**

To improve convergence and computational efficiency a single step solution process was developed. The one step process solves for all the same coefficients as the three step process, but it solves for all coefficients at the same time. This solution procedure is referred to as the "one step process".

To provide some continuity between the VIRA coefficients and the coefficient sets provided by the one step procedure, a one step solution using only PVO and Magellan drag data was run. This one step procedure using only drag data is referred to as the "drag one step process".

To analyze a symmetric atmospheric model where  $T_{\infty}$  is only dependent on solar zenith angle instead of both latitude and LST, a one step solution was run which only determined  $T_{\infty}$  spherical harmonic coefficients dependent on SZA. However, composition was assumed to have an asymmetric distribution not symmetric with SZA. Harmonic coefficients dependent on latitude were set to zero for this solution (see Table 6). This solution of SZA dependent temperature harmonics which includes RWD to provide a solution is referred to as the "one step SZA process". Another similar

procedure was developed which only used drag data to provide a solution, this was referred to as the "drag one step SZA process".

The following table is provided as a quick reference to summarize properties of all coefficient sets referred to in this paper. The table shows which models were determined using what data and whether or not  $T_{\infty}$  and constituent density compositions are determined assuming symmetric or asymmetric distribution with respect to SZA.

Coefficient Set	PVO Drag	Magellan Drag	Magellan RWD	$T_{\infty}$ Dist.	Composition Distribution	steps
Hedin	yes	no	no	Asym	Asym	3
VIRA*	yes	no	no	Sym	Asym	3
KH 93	yes	yes	no	Asym	Asym	3
drag one step SZA	yes	yes	yes	Sym	Asym	1
drag one step	yes	yes	yes	Asym	Asym	1
one step SZA	yes	yes	yes	Sym	Asym	1
one step	yes	yes	yes	Asym	Asym	1
three step	yes	yes	yes	Asym	Asym	3

Table 7: Summary of properties of coefficient sets used in this research

\* Note that the VIRA model used in this research is not exactly the model laid out in the 1985 paper. This model combines the use of asymmetrical composition boundary conditions with a symmetrical  $T_{\infty}$  boundary condition. This version of the VIRA model is a convention taken from previous research conducted in 1993.

#### 4.2.2 Comparison of Three Step and One Step Results

This comparison is laid out here to promote confidence of results presented in Section V, which only presents results from one step solutions of coefficients. Both the one step and three step coefficient solution sets discussed in this section used the same data set which included all available drag and RWD densities. This discussion shows that two separate methods result in similar model coefficient results and are therefore similar

models. One step and three step procedure coefficient results are generally within 30% of each other. Table 8 lists coefficients from the converged three step process and one step procedure and their respective percent differences:

Coefficient	1 Step	3 Step	% Difference((1s-3s)/1s)
$\kappa_{CO_2}$	1.1504e+0	1.2543e+0	-9.0354
$\kappa_O$	1.0280e+0	9.9747e-1	2.9730
$\bar{T}_\infty$	2.3032e+2	2.3162e+2	-0.5652
$T_\infty a_{10}$	5.9465e-1	5.8857e-1	1.0218
$T_\infty b_{11}$	-5.8479e-2	-5.9691e-2	-2.0729
$T_\infty a_{20}$	-3.1598e-2	-2.6979e-2	14.6185
$T_\infty b_{22}$	-1.4308e-2	-1.4291e-2	0.1184
$T_\infty a_{30}$	-2.3039e-1	-2.2894e-1	0.6310
$T_\infty b_{33}$	2.6335e-3	2.7538e-3	-4.5656
$T_\infty a_{40}$	-1.0008e-2	-9.4154e-3	5.9244
$T_\infty b_{44}$	1.9997e-4	1.9242e-4	3.7788
$T_\infty a_{50}$	3.8554e-2	3.3499e-2	13.1111
$T_\infty b_{55}$	-1.2215e-5	-1.1820e-5	3.2359
$T_\infty \bar{f}$	1.4450e-3	1.3405e-3	7.2359
$T_\infty f$	-9.3270e-5	-6.1759e-5	33.7844
$T_\infty \alpha$	4.9526e-4	6.0134e-4	-21.4197
$CO_2 \bar{f}$	-1.3266e-3	-8.6823e-4	34.5513
$O \bar{f}$	4.1469e-3	4.2080e-3	-1.4714
$\kappa_{He}$	1.5199e+0	2.1880e+0	-43.9527

Table 8: Comparison 3 Step vs. 1 Step coefficients and percent difference

One step and three step converged values agree with percent differences within 22% with a few exceptions of parameters whose results are sensitive to changes in solution method parameters. Figures 11 and 12 show how each method converges with respect to each other.

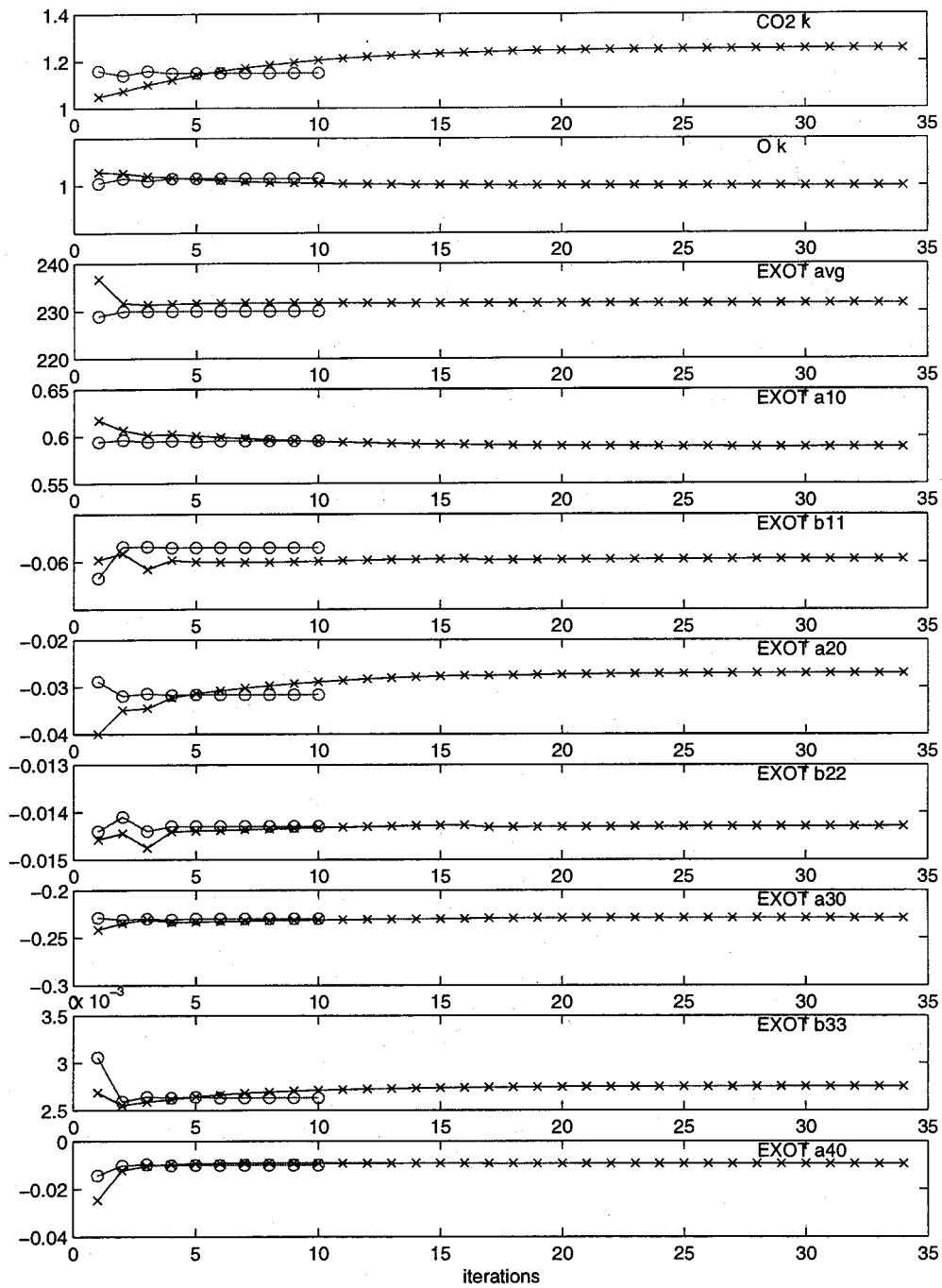


Figure 6 : Coefficient convergence steps of one step(o) and three step(x) procedures

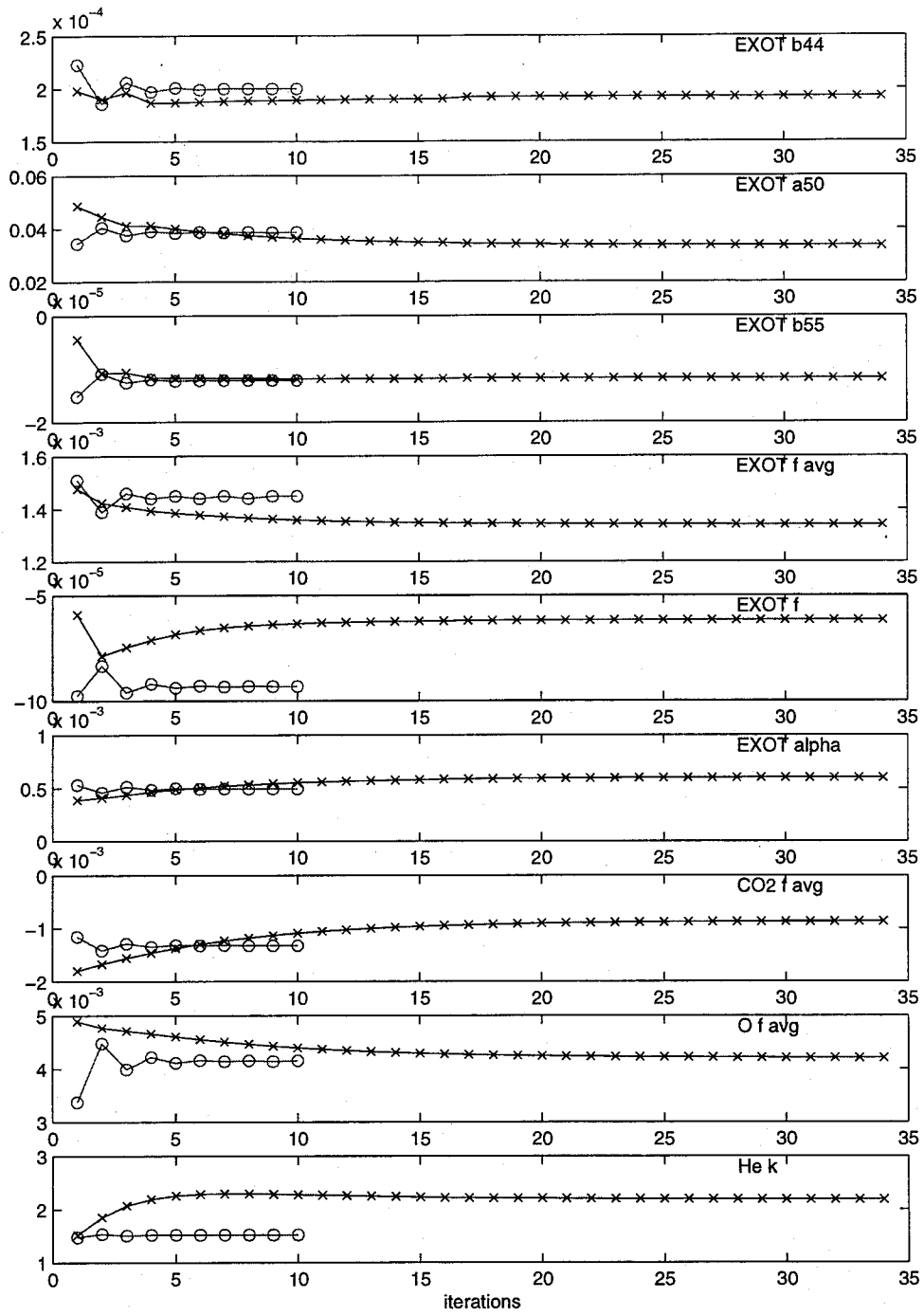


Figure 7 : Coefficient convergence steps of one step(o) and three step(x) procedures

Tables 9 and 10 show the maximum and minimum temperature and density ratios between the three step and one step models:

	150 km	175 km	200 km
Maximum Temperature Ratio	1	1	1
Minimum Temperature Ratio	0.98	0.98	0.98

Table 9 : Maximum and minimum temperature ratios at 150, 175, and 200 km

	150 km	175 km	200 km
Maximum Density Ratio	1.02	1.02	1.00
Minimum Density Ratio	0.99	0.88	0.76

Table 10 : Maximum and minimum density ratios at 150, 175, and 200 km

Figure 8 shows contour plots of ratios comparing results of the one step and three step coefficients sets at 150, 175, and 200 km. Solar activity for these comparisons was set to 100 to establish variability with respect to solar activity. When solar activity is set to 200 the solar activity variations within the model are canceled. Differences in temperatures never exceed  $\pm 2\%$ . Similarly, the density prediction results between coefficient sets do not vary by more than  $\pm 25\%$  from each other. These results show fair agreement between one step and three step procedures. The three step procedure once needed to attain convergence is no longer needed with the use of data weighting. The one step is preferable to the three step due to its efficiency.

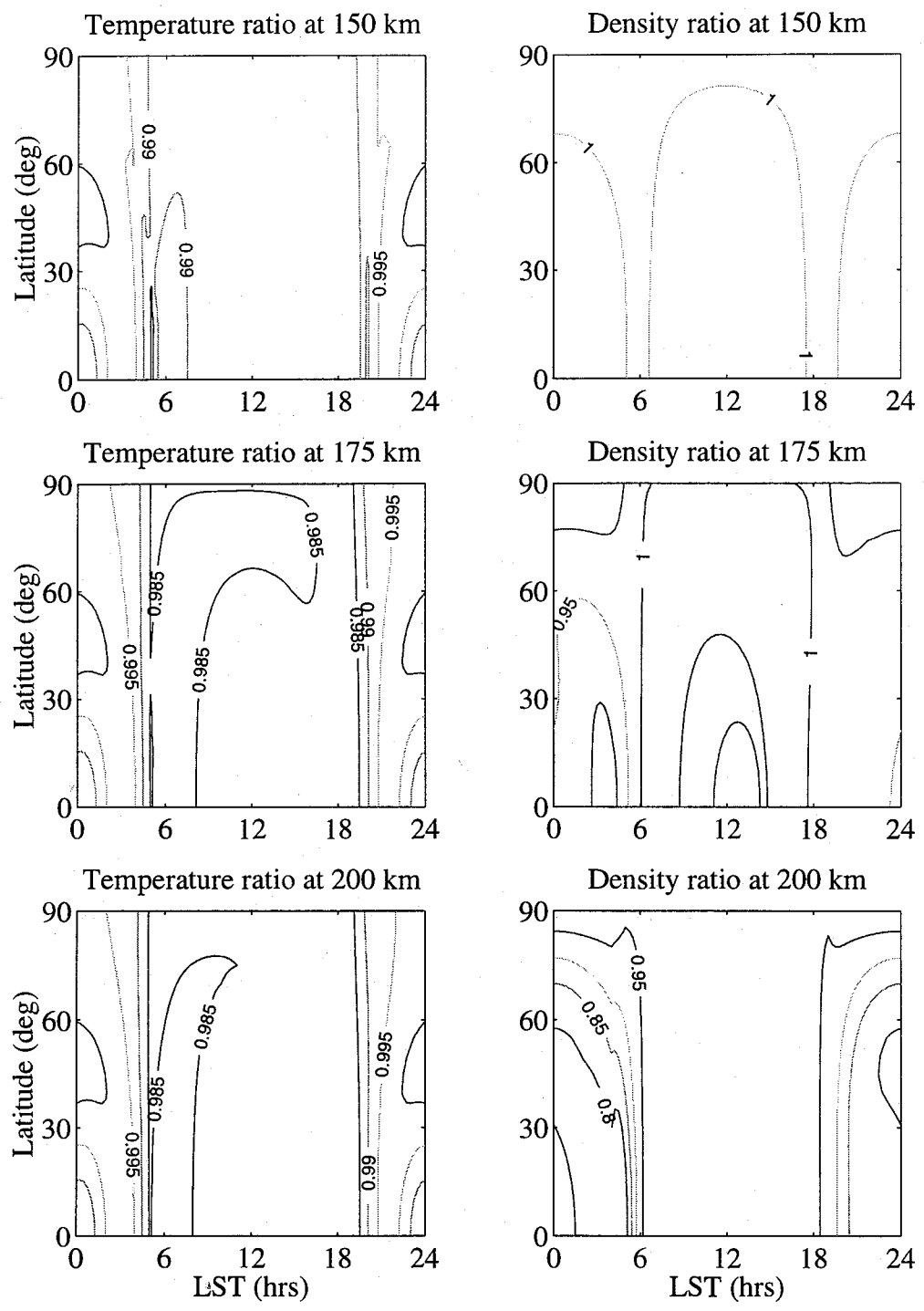


Figure 8 : Comparison of three step vs. one step coefficients

## V. RESULTS

### 5.1 Methods for Obtaining Results

Results were obtained by using data discussed in Section II in the minimum variance method discussed in Section IV. The minimum variance method minimized residuals in log density. Whenever possible, the estimated parameters were converged without using a priori. Converged coefficient solutions which do not use a priori more truly reflect what the data represents and not some assumption of what the model should represent. However, one instance did arise where a single coefficient, the Helium ONMS sensitivity, was restricted to insure the solutions resulted in models which made physical sense. The Helium ONMS sensitivity was restricted because no RWD sampled the Helium bulge on the night-side.

To ensure converged coefficient sets are independent of starting coefficients two cases were run which were identical except for the starting coefficients. These test cases used both drag and RWD density measurements. One step used VIRA coefficients. While the other used a coefficient set randomly 20% above or below the VIRA coefficients. The minimum variance method without using a priori converged to the exact same values. However, converged results using the three step procedure are dependent on initial coefficients.

Fourteen of the nineteen coefficients proposed to be updated are coefficients which determine  $T_{\infty}$ . A discussion is presented to clarify the history and progression of these coefficients and provide a layout of how results are presented in this section. The published VIRA model is a diurnally symmetric model in determination of  $T_{\infty}$  and density composition meaning that  $T_{\infty}$  and density composition only vary in SZA. However, an

asymmetric model was developed simultaneously with the published VIRA model which varied in SZA and latitude. This model, referred to as VIRA asymmetric model, provides for asymmetries in  $T_{\infty}$  and composition between a.m. and p.m. The VIRA asymmetric model is consistent with the Hedin number density boundary conditions at 150 km, which are asymmetric in SZA, except for the ONMS sensitivity parameters derived from drag data. Continued research in 1993<sup>4</sup> included more recently acquired PVO and low latitude Magellan drag data to update the asymmetric model and determined updated coefficients for spherical harmonics dependent on SZA and latitude. The results presented in this section update symmetric and asymmetric models accordingly. To use a symmetric model the  $T_{\infty}$   $b_{nm}$  coefficients are set to zero, thus producing a model with  $T_{\infty}$  dependent on SZA.

Recall the discussion made in Section 1.2.3 regarding the VIRA model and coefficient sets. The model remains unchanged throughout the research using different coefficient sets. Converting the model to have either a symmetric or asymmetric temperature distribution with respect to SZA simply requires setting the asymmetric coefficients to zero for a symmetric distribution. This does not require changes within the mathematical formulation of the model. The results section presents coefficient sets for use with the VIRA model mathematical structure. The coefficients were determined using the minimum variance method. Solar activity for these comparisons was set to 100 to establish variability with respect to solar activity. When solar activity is set to 200 the solar activity variations in the model cancel (see Section 2.3 spherical harmonic expansion function).

## 5.2 Drag Data Results

Discussed in this section are results determined using only drag data from PVO and Magellan. These results include mid latitude Magellan drag density measurements which were obtained after the KH93 model<sup>4</sup> was developed.

### 5.2.1 Symmetric Coefficients

This section discusses symmetric coefficient results obtained from the one step process only using PVO and Magellan drag data. These results have been designated the "drag one step SZA coefficients". Appendix C contains tables of the correlation matrix for this converged solution and estimated accuracy of each parameter. Correlations between coefficients are mostly below 60% although some coefficients are correlated to one another as high as 89%. The 89% correlation is between CO<sub>2</sub> ONMS sensitivity and CO<sub>2</sub> solar activity variation coefficients. The most uncertain coefficient of the solution is the T<sub>∞</sub> harmonic a<sub>40</sub> coefficient at 44% standard deviation. Tables 11 and 12 show the maximum and minimum temperature and density ratios comparing results of the VIRA and the drag one step SZA coefficient sets at 150, 175, and 200 km:

	150 km	175 km	200 km
Maximum Temperature Ratio	0.99	0.99	0.99
Minimum Temperature Ratio	0.79	0.79	0.79

Table 11: Maximum and minimum temperature ratios at 150, 175, and 200 km

	150 km	175 km	200 km
Maximum Density Ratio	1.03	0.91	0.90
Minimum Density Ratio	0.82	0.49	0.39

Table 12: Maximum and minimum density ratios at 150, 175, and 200 km

Figure 9 shows contour plots of temperature ratio and density ratio results comparing VIRA and drag one step SZA coefficients sets at 150, 175, and 200 km. The

differences in temperatures never exceed  $\pm 21\%$ . However, the differences between densities increase with altitude, varying for a maximum ratio at 0.90 and minimum ratio at 0.37. The biggest deviations between results appear to be at mid latitudes and at night. The locations of these deviations make intuitive sense since the data set contains more data at mid latitudes and at night.

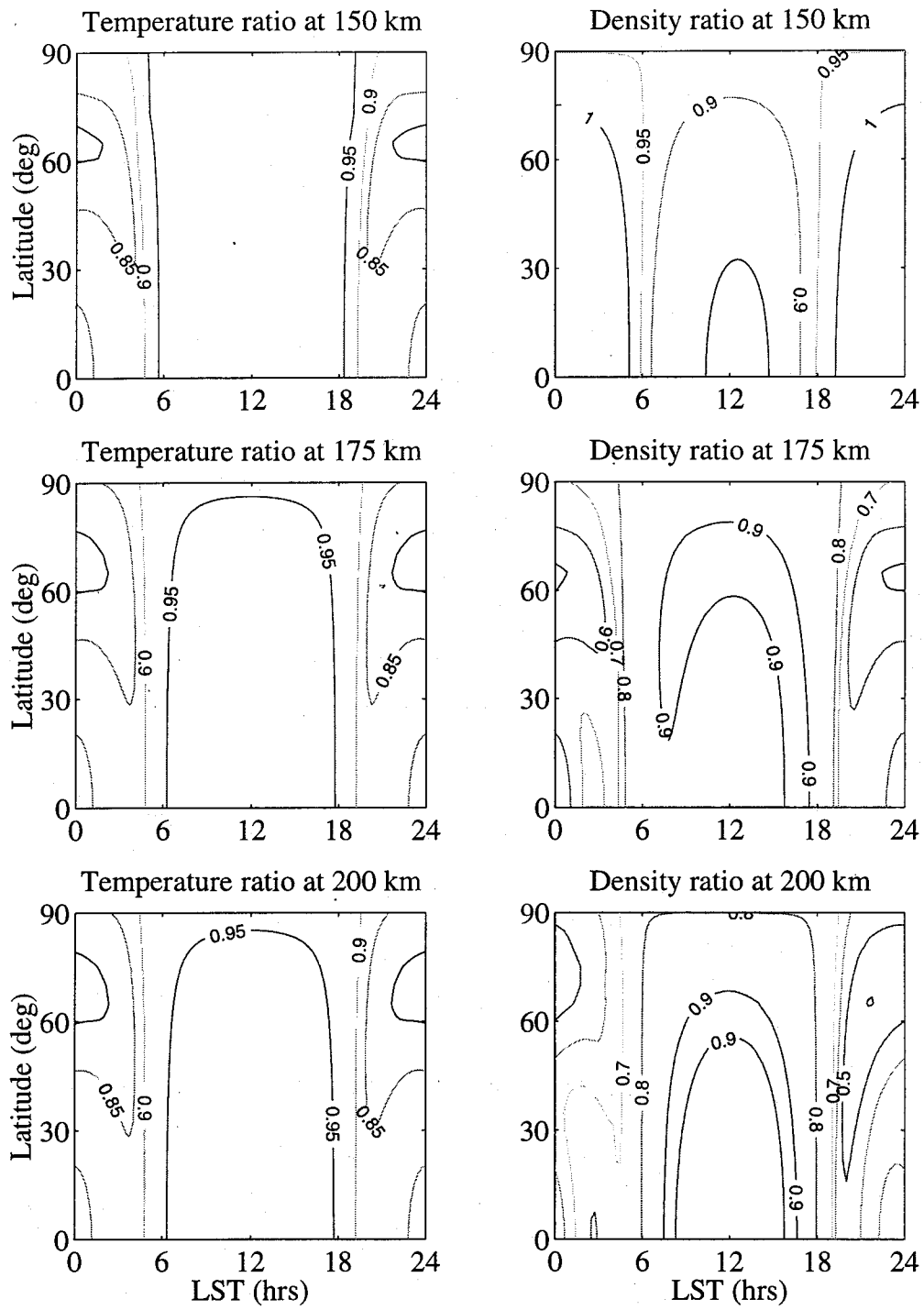


Figure 9 : Comparison of VIRA vs. drag one step SZA coefficients

### 5.2.2 Asymmetric Coefficients

This section discusses asymmetric coefficient results obtained from the one step process only using PVO and Magellan drag data. These results have been designated the "drag one step coefficients". Appendix C contains tables of the correlation matrix for this converged solution and estimated accuracy of each parameter. Correlations between coefficients are mostly below 60% although some coefficients are correlated to one another as high as 89%. The 89% correlation is between CO<sub>2</sub> ONMS sensitivity and CO<sub>2</sub> solar activity variation coefficients. The most uncertain coefficient of the solution is the T<sub>∞</sub> harmonic a<sub>40</sub> coefficient at 47% standard deviation. Tables 13 and 14 show the maximum and minimum temperature and density ratios comparing results of the KH 93 and drag one step coefficient sets at 150, 175, and 200 km:

	150 km	175 km	200 km
Maximum Temperature Ratio	1.06	1.07	1.07
Minimum Temperature Ratio	0.91	0.89	0.89

Table 13 : Maximum and minimum temperature ratios at 150, 175, and 200 km

	150 km	175 km	200 km
Maximum Density Ratio	1.25	1.86	2.23
Minimum Density Ratio	0.99	0.86	0.83

Table 14 : Maximum and minimum density ratios at 150, 175, and 200 km

Figure 10 shows contour plots of temperature ratio and density ratio results comparing KH 93 and drag one step coefficients sets at 150, 175, and 200 km.

Differences in temperatures never exceed  $\pm 11\%$ . However, the density ratios increase with altitude, varying for a maximum of 1.11 and a minimum of 0.47. Again, the largest deviations occur at mid latitudes and on the night-side.

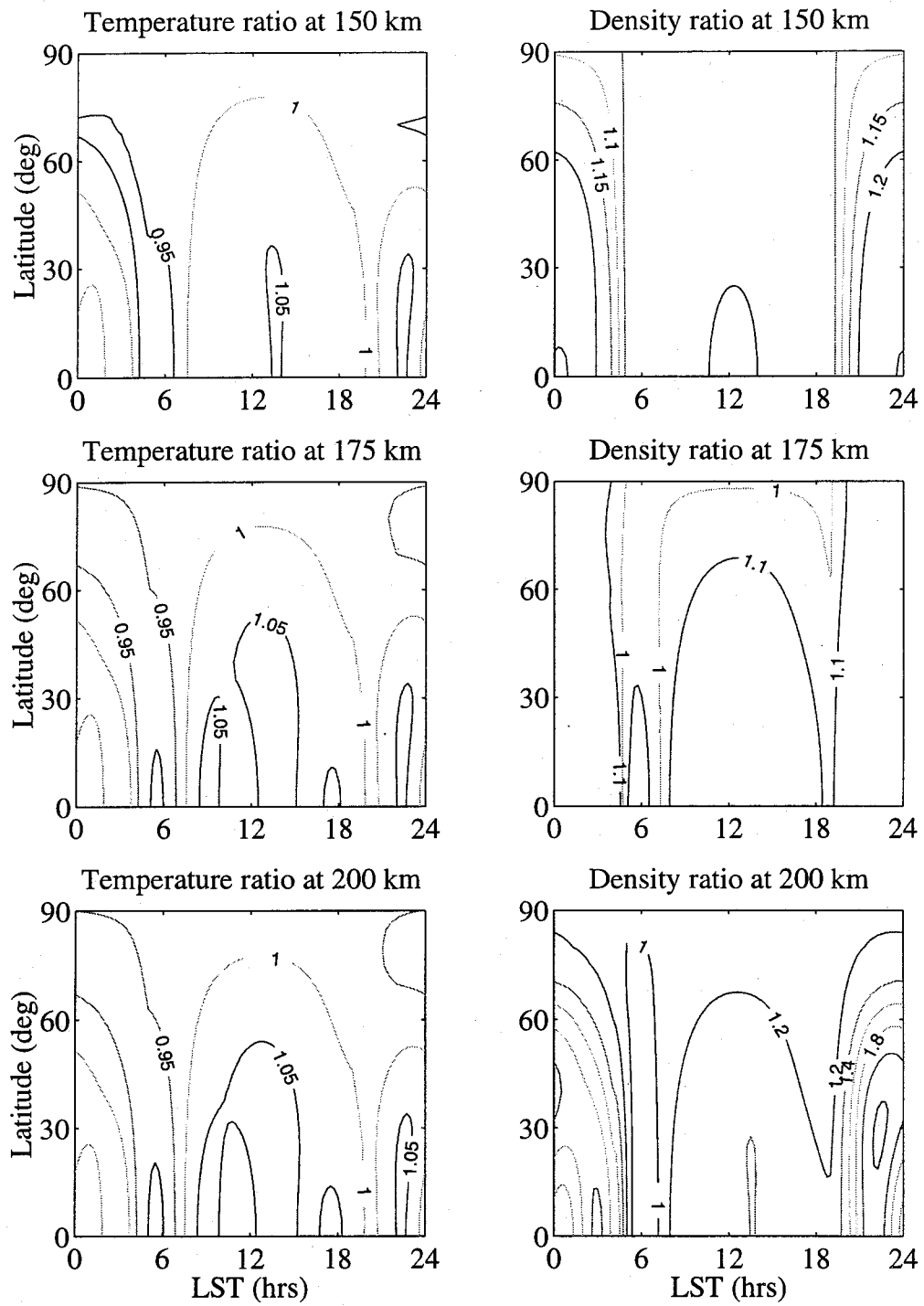


Figure 10: Comparison of KH 93 vs. drag one step coefficients

### 5.3 Combined Drag and Reaction Wheel Data Results

#### 5.3.1 Symmetric Coefficients

This section discusses symmetric coefficient results obtained from the one step process using all PVO drag, Magellan drag, and Magellan reaction wheel data. These results have been designated the "one step SZA coefficients". Appendix C contains tables of the correlation matrix for this converged solution and estimated accuracy of each parameter. Correlations between coefficients are mostly below 60% although some coefficients are correlated to one another as high as 90%. The 90% correlation is between CO<sub>2</sub> ONMS sensitivity and CO<sub>2</sub> solar activity variation coefficients. The most uncertain coefficient of the solution is the T<sub>∞</sub> harmonic a<sub>40</sub> coefficient at 47% standard deviation. Tables 15 and 16 show the maximum and minimum temperature and density ratios comparing results of the VIRA and one step SZA coefficient sets at 150, 175, and 200km:

	150 km	175 km	200 km
Maximum Temperature Ratio	1.10	1.13	1.14
Minimum Temperature Ratio	0.81	0.81	0.81

Table 15 : Maximum and minimum temperature ratios at 150, 175, and 200 km

	150 km	175 km	200 km
Maximum Density Ratio	1.06	1.11	1.11
Minimum Density Ratio	0.89	0.45	0.47

Table 16 : Maximum and minimum density ratios at 150, 175, and 200 km

Figure 11 shows contour plots of temperature ratio and density ratio results comparing the VIRA and one step SZA coefficients sets at 150, 175, and 200 km. Differences in temperatures never exceed  $\pm 20\%$ . However, the density ratios increase with altitude, varying for a maximum of 1.11 to minimum of 0.47. Again, the largest differences between results occur at mid latitudes and at night.

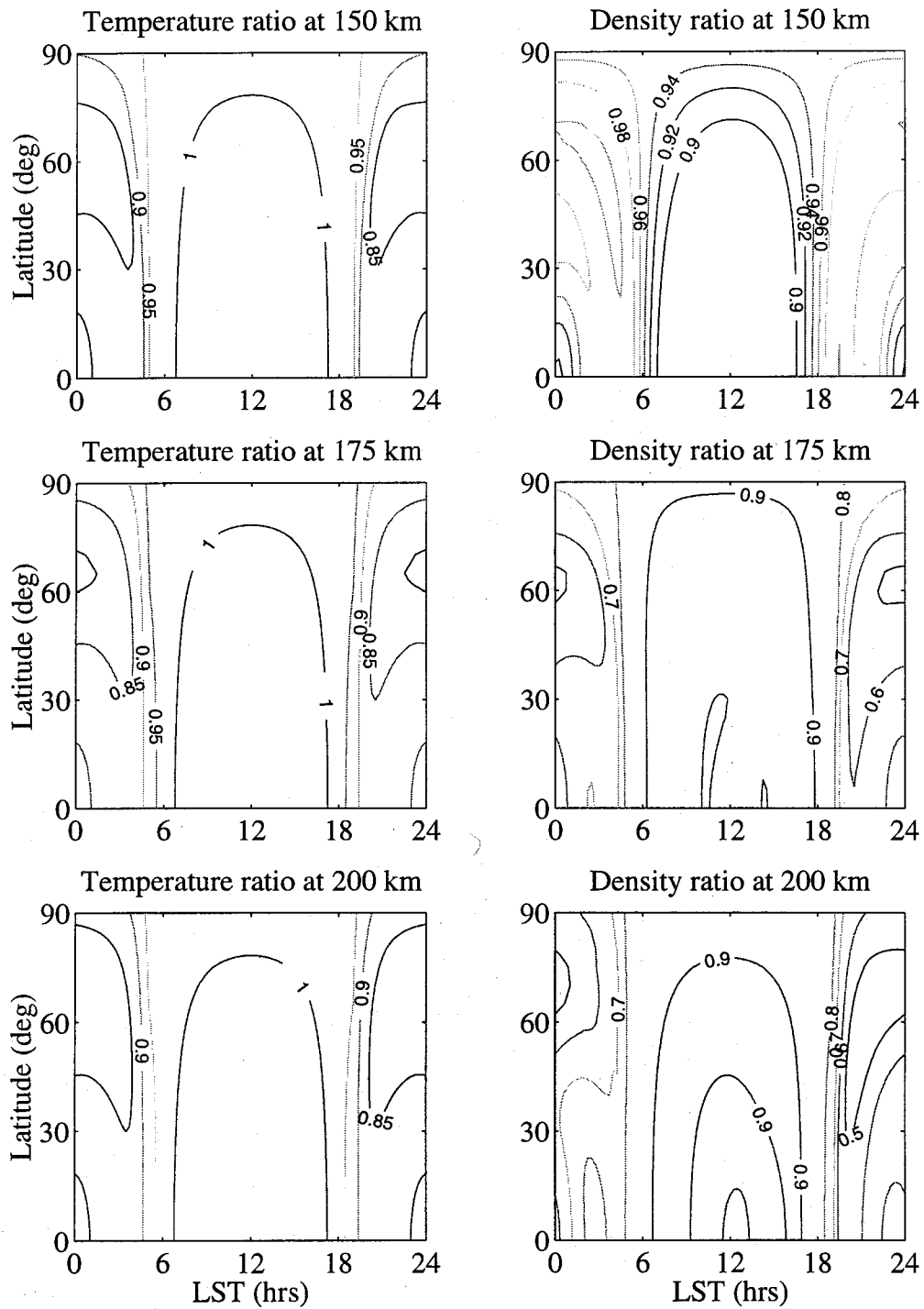


Figure 11 : Comparison of VIRA vs. one step SZA coefficients

### 5.3.2 Asymmetric Coefficients

This section discusses asymmetric coefficient results obtained from the one step process using all PVO drag, Magellan drag, and Magellan reaction wheel data to produce results. These results have been designated the "one step coefficients". Appendix C contains tables of the correlation matrix for this converged solution and estimated accuracy of each parameter. Correlations between coefficients are mostly below 60% although some coefficients are correlated to one another as high as 90%. The 90% correlation is between CO<sub>2</sub> ONMS sensitivity and CO<sub>2</sub> solar activity variation coefficients. The most uncertain coefficient of the solution is the T<sub>∞</sub> harmonic a<sub>40</sub> coefficient at 67% standard deviation. Tables 17 and 18 show the maximum and minimum temperature and density ratios comparing results for the KH 93 and one step coefficient sets at 150, 175, and 200 km:

	150 km	175 km	200 km
Maximum Temperature Ratio	1.13	1.13	1.13
Minimum Temperature Ratio	0.90	0.87	0.87

Table 17 : Maximum and minimum temperature ratios at 150, 175, and 200 km

	150 km	175 km	200 km
Maximum Density Ratio	1.13	1.73	1.83
Minimum Density Ratio	0.99	0.85	0.73

Table 18 : Maximum and minimum density ratios at 150, 175, and 200 km

Figures 12 shows contour plots of temperature ratio and density ratio results comparing the KH 93 and the one step coefficient sets at 150, 175, and 200 km. Differences in temperatures never exceed  $\pm 13\%$ . However, the density ratios increase with altitude, varying for a maximum of 1.83 to minimum of 0.73. Again, the largest differences between results occur at mid latitudes and at night.

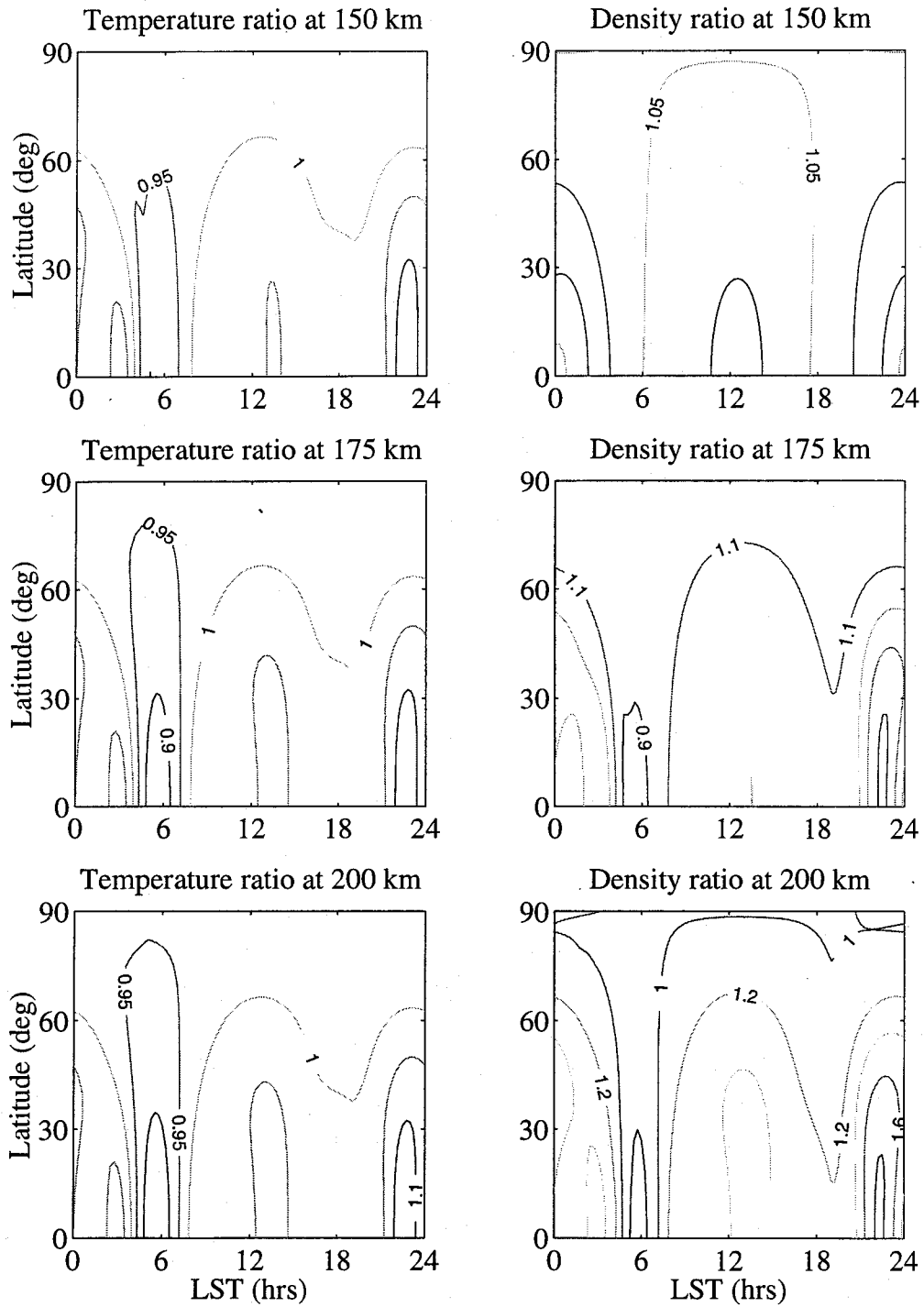


Figure 12: Comparison of KH 93 vs. one step coefficients

### 5.3.3 Asymmetric Results from Three Step Procedure

This section discusses asymmetric coefficient results obtained from the three step process using all PVO drag, Magellan drag, and Magellan reaction wheel data to produce results. These results have been designated the "three step coefficients". Appendix C contains tables of the correlation matrix for each converged solution step and estimated accuracy of each parameter. Correlations between coefficients are mostly below 60% although some coefficients are correlated to one another as high as 92%. The 92% correlation is between O ONMS sensitivity and mean  $T_{\infty}$  coefficients for the first step. The most uncertain coefficient of the solution is the  $T_{\infty}$  harmonic  $a_{40}$  coefficient at 58% standard deviation for step one and the  $T_{\infty}$  short term solar activity parameter coefficient at 385% standard deviation for step two. Tables 19 and 20 show the maximum and minimum temperature and density ratios comparing results of the KH 93 and three step coefficient sets at altitudes of 150, 175, and 200 km:

	150 km	175 km	200 km
Maximum Temperature Ratio	1.14	1.14	1.14
Minimum Temperature Ratio	0.91	0.88	0.87

Table 19 : Maximum and minimum temperature ratios at 150, 175, and 200 km

	150 km	175 km	200 km
Maximum Density Ratio	1.11	1.78	2.22
Minimum Density Ratio	0.97	0.87	0.79

Table 20 : Maximum and minimum density ratios at 150, 175, and 200 km

Figures 13 shows contour plots of temperature ratio and density ratio results comparing the KH 93 and three step coefficient sets at 150, 175, and 200 km. Differences in temperatures never exceed  $\pm 14\%$ . However, the density ratios increase with altitude, varying for a maximum of 2.22 to minimum of 0.79. Again, the largest difference between results occur at mid latitudes and at night.

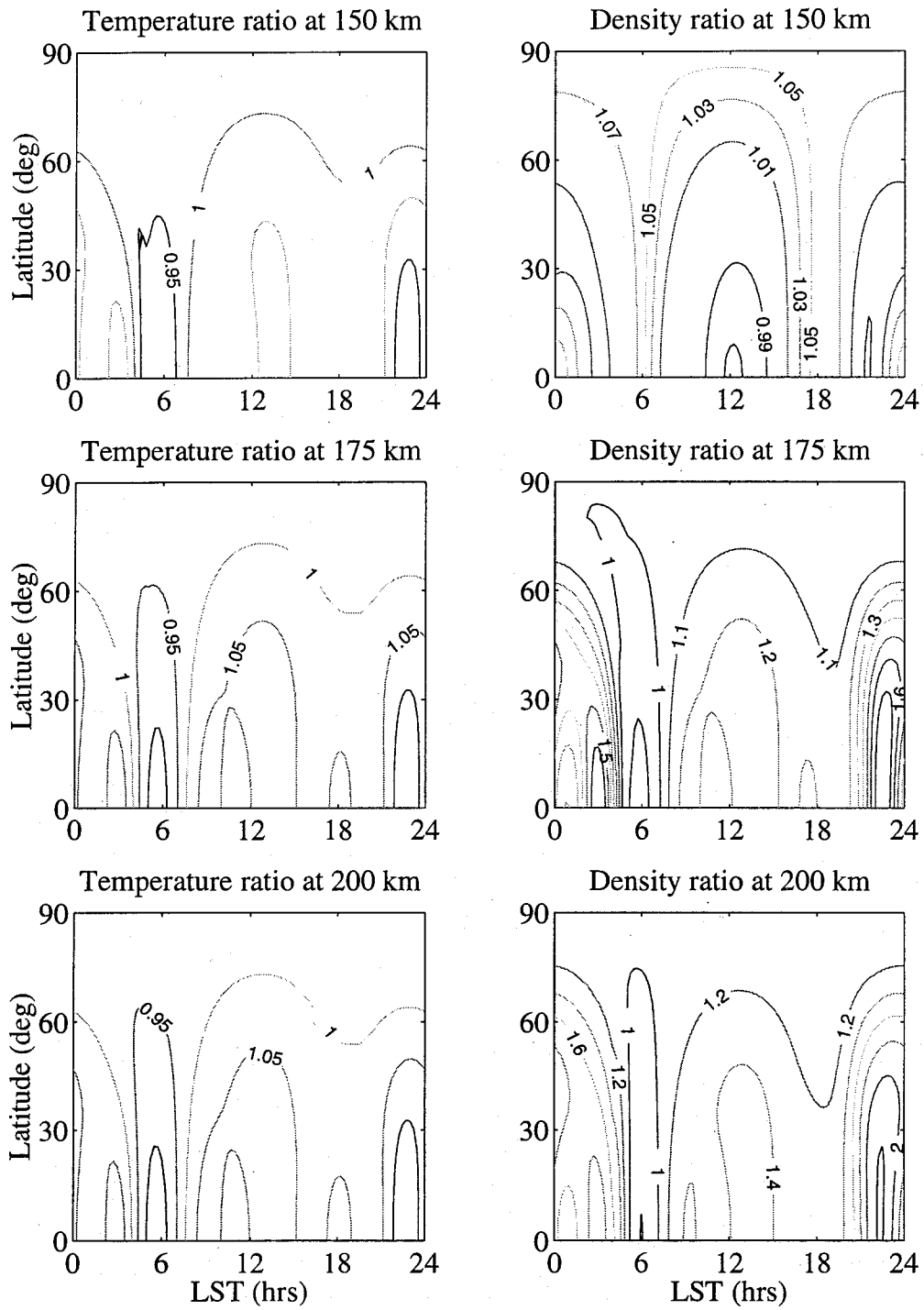


Figure 13 : Comparison of KH 93 vs. three step coefficients

## 5.4 Analysis of Coefficient Sets

A measure was established to compare different coefficient sets and determine which set of coefficients best fits available density measurements. The weighted mean of residuals and weighted standard deviation of residuals are calculated to determine how well a coefficient set reproduces the observations. Each observation and model estimate residual is weighted in the same manner that the minimum variance method weights reliable observations more than unreliable observations. This is done to give a clearer picture of how well the minimum variance method produced converged coefficient sets according to the data. The following equation shows how the weighted residual between each observation and model prediction is calculated:

$$\varepsilon = \ln\left(\frac{\rho_{\text{obs}}}{\rho_{\text{model}}}\right) \cdot \frac{\rho_{\text{obs}}}{\sigma_{\text{obs}}}$$

The weighted mean residual and weighted standard deviation of residuals can then be calculated. Table 21 shows weighted mean residuals and weighted standard deviation of residuals from all data including both drag and RWD measurements for each coefficient set:

Coefficient Set	Weighted Mean	Weighted Standard Deviation
Hedin	-0.4527	2.1446
VIRA	-0.2863	2.1748
drag one step SZA	0.1110	1.9671
drag one step	0.0810	1.8738
one step SZA	-0.0333	1.9607
one step	-0.0196	1.8578
three step	-0.0056	1.8574

Table 21 : Weighted mean and standard deviation of all data residuals

A model which perfectly fits available data would have a mean residual of zero and a standard deviation of residual of zero. Presumably the one step SZA, one step and

three step models fit all available data the best since the means of these models are closest to zero. However, Table 22 shows that mean residuals for each coefficient set of only drag data and only RWD are not close to zero. This may indicate that issues still exist between drag and RWD measurements. Table 22 shows weighted mean residuals and weighted standard deviation of residuals from only drag data measurements and only RWD measurements for each coefficient set model:

Coefficient Set	Weighted Mean of drag data residuals	Weighted Std. Dev. of drag data residuals	Weighted Mean of RWD residuals	Weighted Std. Dev. of RWD residuals*
Hedin	-0.6537	3.5533	-0.3444	0.4965
VIRA	-0.6535	3.5646	-0.0866	0.5706
drag SZA	-0.0568	3.1912	0.2013	0.6698
drag one step	-0.1520	3.0382	0.2065	0.6233
SZA	-0.1246	3.2004	0.1182	0.6168
one step	-0.1517	3.0360	0.1118	0.5694
three step	-0.2055	3.0343	0.1020	0.5649

Table 22: Weighted mean and standard deviation of drag and RWD residuals

\*Note that weighted standard deviation of RWD measurements are closer to zero than weighted standard deviations of drag data because the RWD is more inaccurate with less weighting and consequently has a lower standard deviation than the drag data residuals.

Interpretation of Tables 21 and 22 leads to the conclusion that the bias analysis is not completely correct. When estimating for all data the mean residuals approach zero, but when only drag data is estimated by the same models the mean residuals tend to be negative and the exact opposite occurs for RWD observations for which the mean is positive. This suggests that a bias still exists between the drag and RWD measurements.

## 5.5 Wave Activity on Venus

Figures 14 and 15 show examples of transient spatial and temporal variations, which are here on called waves for lack of a better term, where observed density measurements substantially deviated from atmospheric models. Previously, two instances of possible wave activity have been detected during the reduction of the reaction wheel data<sup>2</sup> in orbits 11730, 11732, 11734 and 11740, 11742, 11744 which occur around 1700 LST. Available plots of orbits between 11776 and 11796 show another wave not discussed in a previous thesis by Espiritu. Appendix D contains plots of every orbit from which reaction wheel data was successfully retrieved and reduced. Closer inspection of reaction wheel data measurements of successive orbits around the terminator show deviation between reaction wheel measurements and the model that are interpreted as an example of wave activity or some other phenomena. A wave begins to manifest itself on orbit 11776 as a noticeable bulge relative to model estimates below 10°N latitude. The bulge progressively increases to a maximum on orbit 11786. Density then gradually drops back to model estimates until orbit 11796 where the reaction wheel data and the model are in good accord.

Another discernible trend in the plots shown in Figures 14 and 15 is a consistent deviation of reaction wheel measurements from model estimates. The maximum deviation seems to occur near the same latitude, approximately 5 degrees north of the equator, for all of these orbits which is not the periapsis latitude. The latitudes of periapsis of these orbits tend to be around 12°N. These plots show a sustained density gradient with respect to latitude. Such a gradient is not evident in other RWD passes in Appendix D. This phenomenon may be isolated to regions near the terminator.

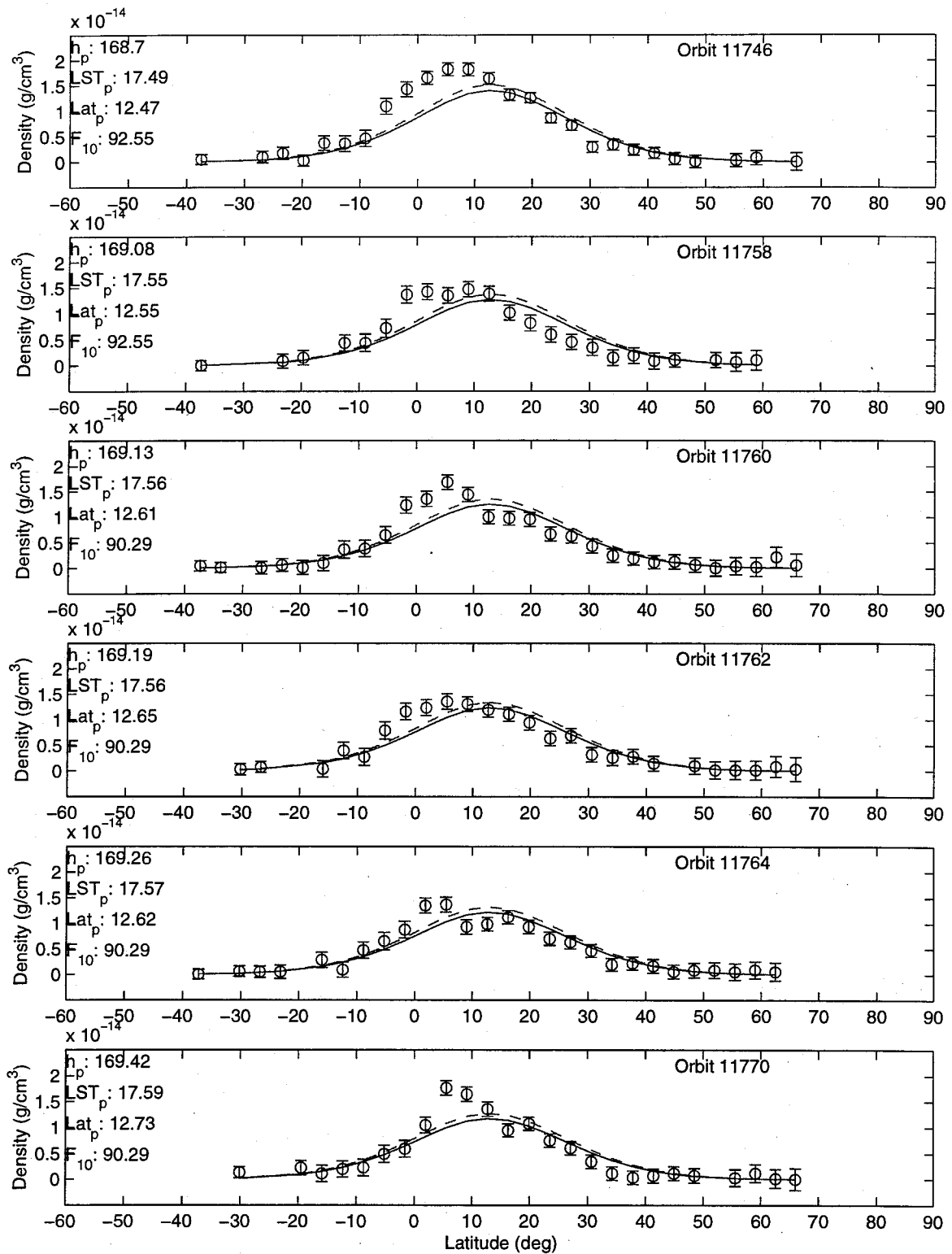


Figure 14 : Successive reaction wheel orbits near terminator  
 (Solid - one step SZA model ; Dashed - VIRA model)

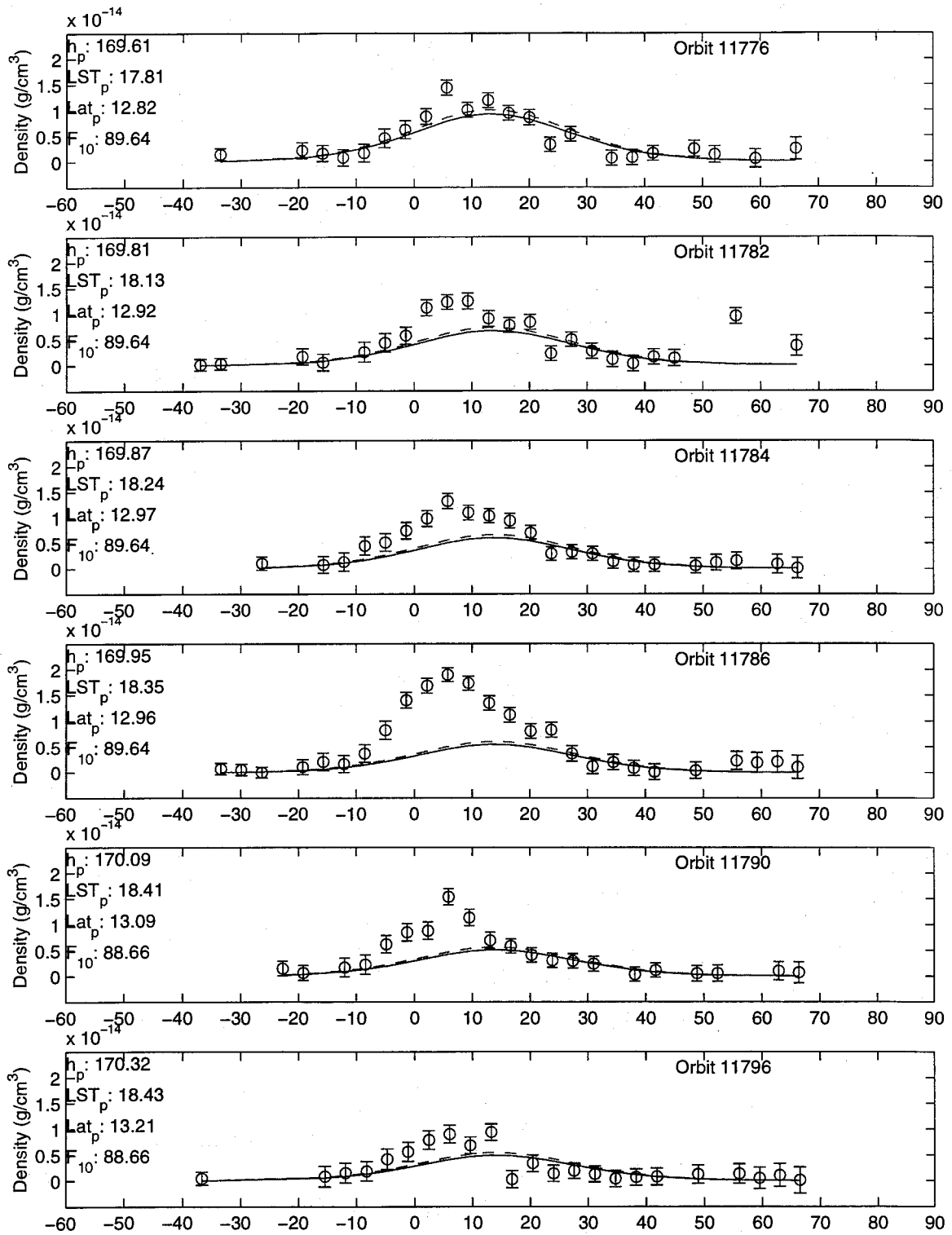


Figure 15 : Successive reaction wheel orbits near terminator  
(Solid - one step SZA model ; Dashed - VIRA model)

## VI. DISCUSSION

Results provided in Section V present several coefficient sets to discuss. This section will introduce and briefly discuss topics which were encountered during the course of this research that do not belong earlier in this paper. Such topics include: acknowledged dynamic effects which occur within the atmosphere that are reflected in coefficient sets presented in Section V; effects on minimum variance solutions regarding the inclusion or exclusion of RWD; improved estimation by the VIRA model of the latitudinal variations; and improvement of the VIRA model using drag and RWD.

The VIRA model is mathematical in nature and does not directly reflect dynamic effects such as adiabatic cooling<sup>7</sup> present in the Venus atmosphere. The minimum variance method is a method to adjust model coefficients to fit the available data. When these resulting model coefficients predict expected physical phenomena this lends credence to the model coefficients. Figure 16 shows model coefficients which reflect adiabatic cooling.

Figure 16 shows temperature profiles of the VIRA model using the four one step coefficient sets from Section V. The existence of adiabatic cooling is represented by the lower temperatures around 1200 LST, where the atmosphere is rising and adiabatic cooling is taking place, compared to higher temperatures before and after 1200 LST. The two plots on the left are temperature plots of  $T_{\infty}$  symmetric models which used drag only and drag and RWD to obtain converged coefficients. These plots resemble each other imparting confidence that the inclusion of RWD does not overly influence the VIRA model.

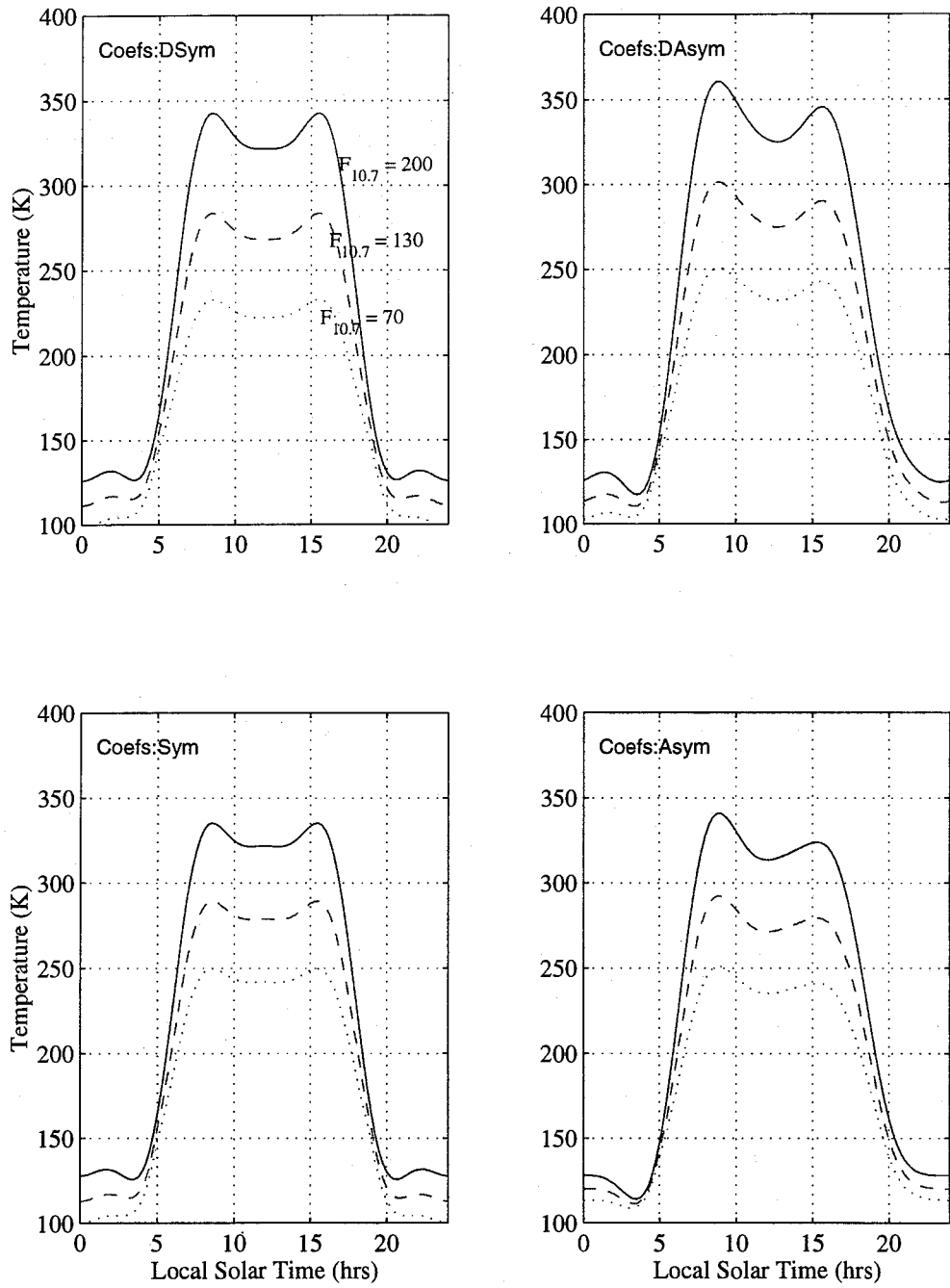


Figure 16 :  $T_{\infty}$  distributions of four coefficient set models varying in solar activity

The two other plots on the right side are temperature plots of  $T_{\infty}$  asymmetric models using drag only and drag and RWD to obtain converged results. These asymmetric models both indicate a hotter atmosphere in the morning than at night. The hotter temperatures in the morning may be indicative of mathematical artifacts within the model created by a poor distribution of data.

Also referring to Figure 16, the asymmetry in  $T_{\infty}$  is just as evident in the asymmetric model from drag data as it is in the asymmetric model derived from drag data and RWD. This implies that the RWD does not unbalance the model with respect to a.m./p.m. temperature distribution. However, both symmetric and asymmetric models resulting from the use of drag and RWD measurements have cooler temperatures than their respective models which only used drag data. This suggests that solar activity variations be restricted during or removed from minimum variance solutions which involve all reaction wheel data measurements. The fact that symmetric and asymmetric temperature profiles in Figure 16 are similar indicates that the symmetric model adequately fits available data by using fewer model coefficients. The symmetric one step approach is the most practical method to further investigate updating the VIRA model. Using the asymmetric model may create asymmetries in LST because all the RWD is in the afternoon.

Figure 17 show ratios of observed RWD densities over estimated densities using the VIRA model. Figures 18 and 19 show the same ratios using the one step SZA model and one step model density estimates, respectively. Figures 20, 21 and 22 show the same density ratios plotted versus SZA. The observation to model ratio mean and standard deviation for each coefficient set is also listed on these plots.

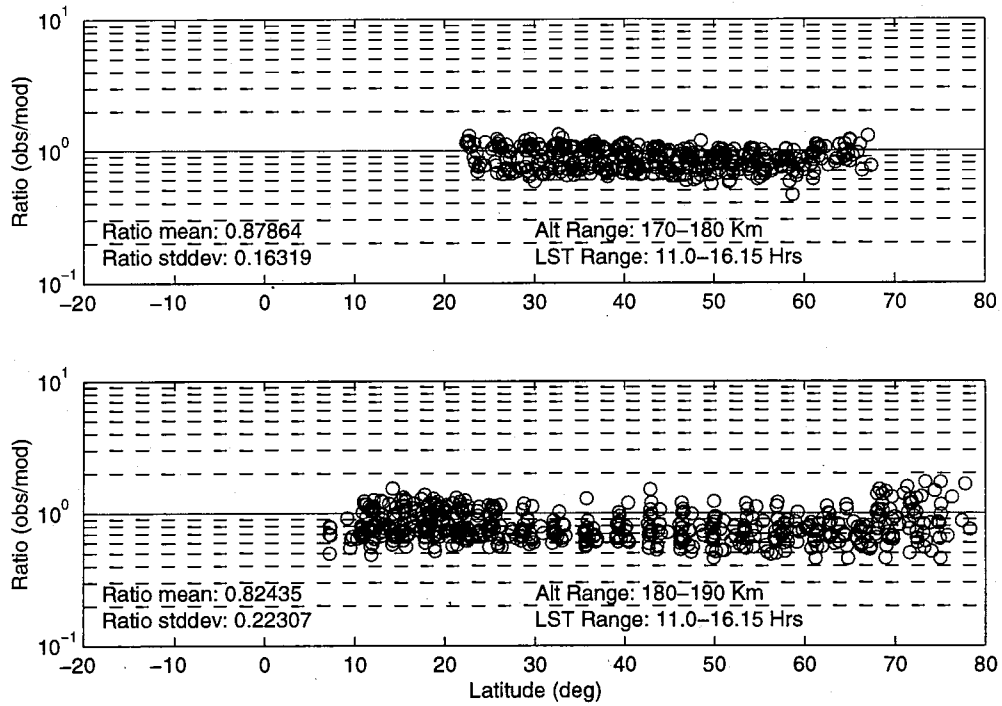


Figure 17: Day-side RWD observed/model density ratio vs. latitude using VIRA model

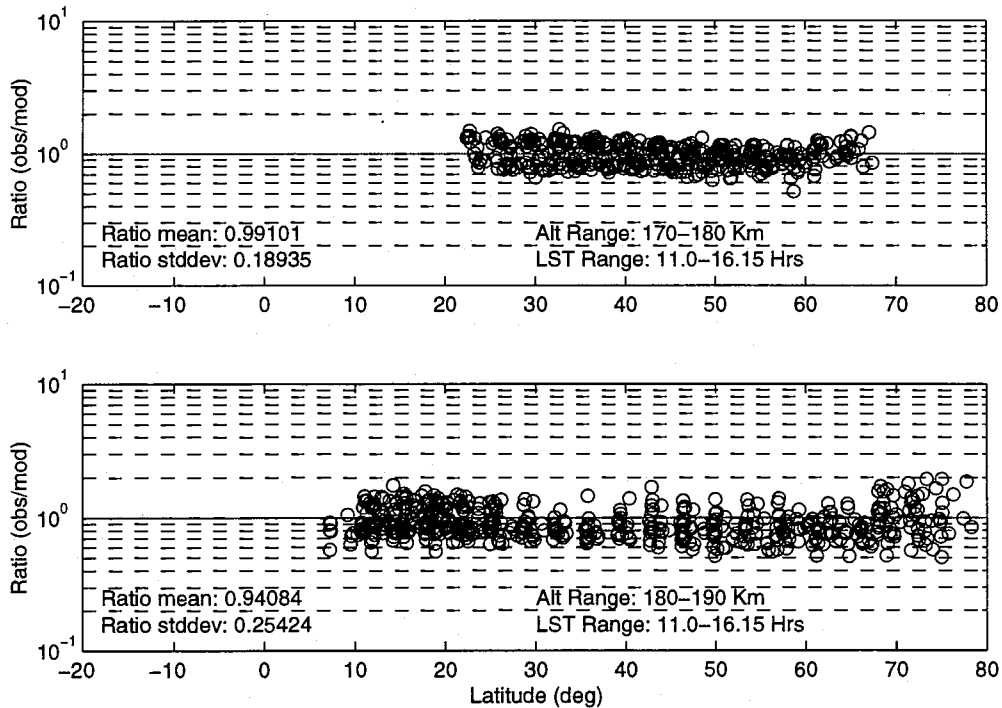


Figure 18: Day-side RWD observed/model density ratio vs. latitude using SZA model

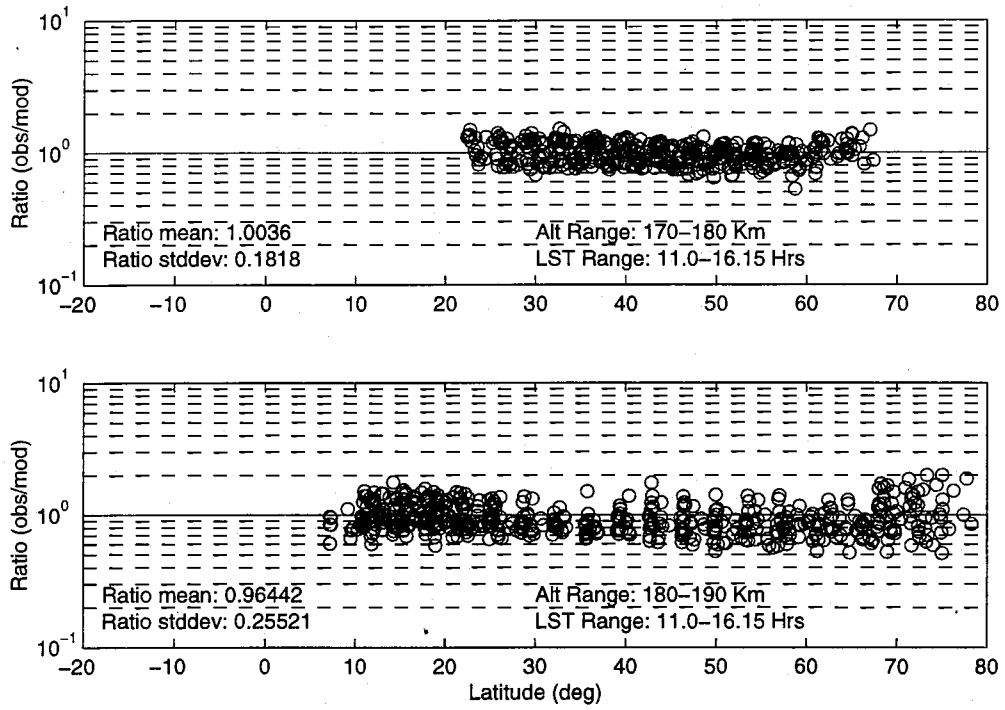


Figure 19: Day-side RWD observed/model density ratio vs. latitude using one step model

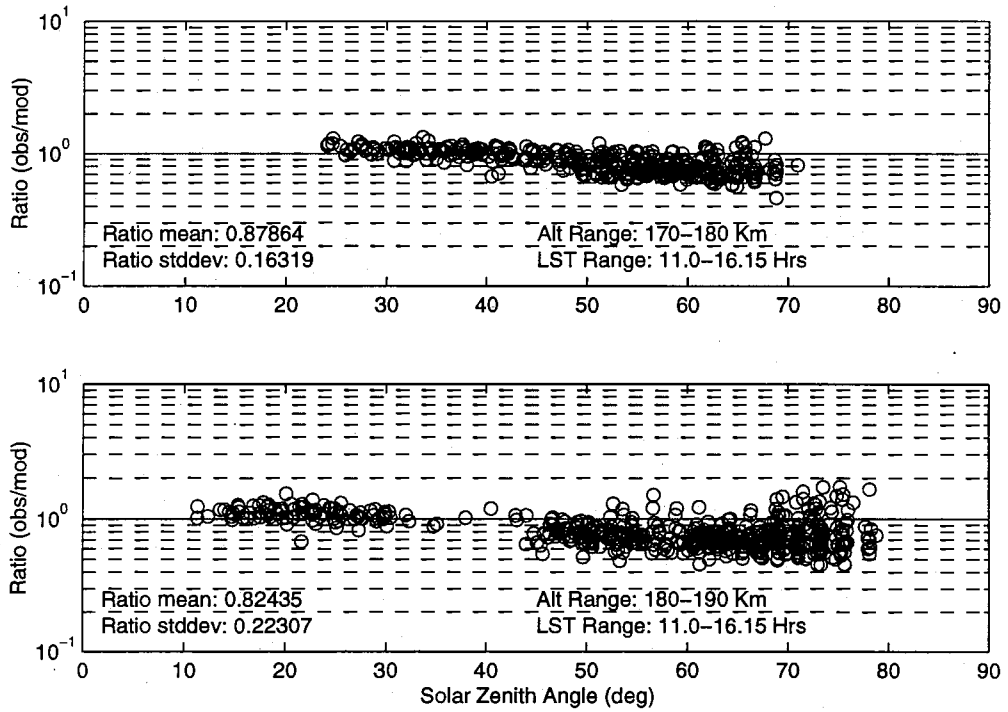


Figure 20: Day-side RWD observed/model density ratio vs. SZA using VIRA model

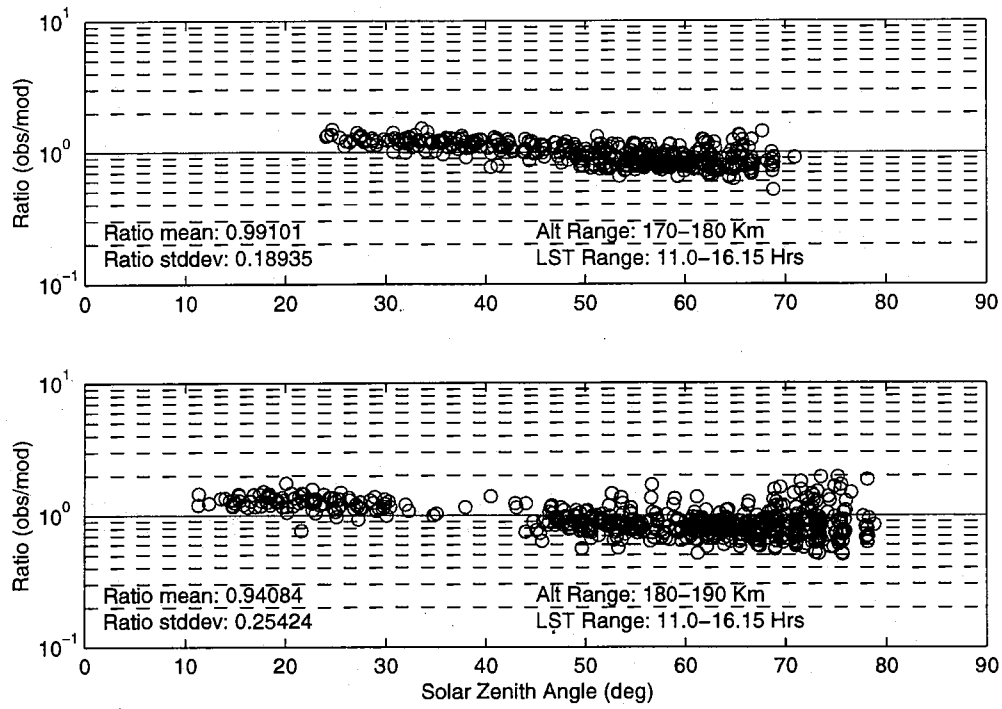


Figure 21: Day-side RWD observed/model density ratio vs. SZA using SZA model

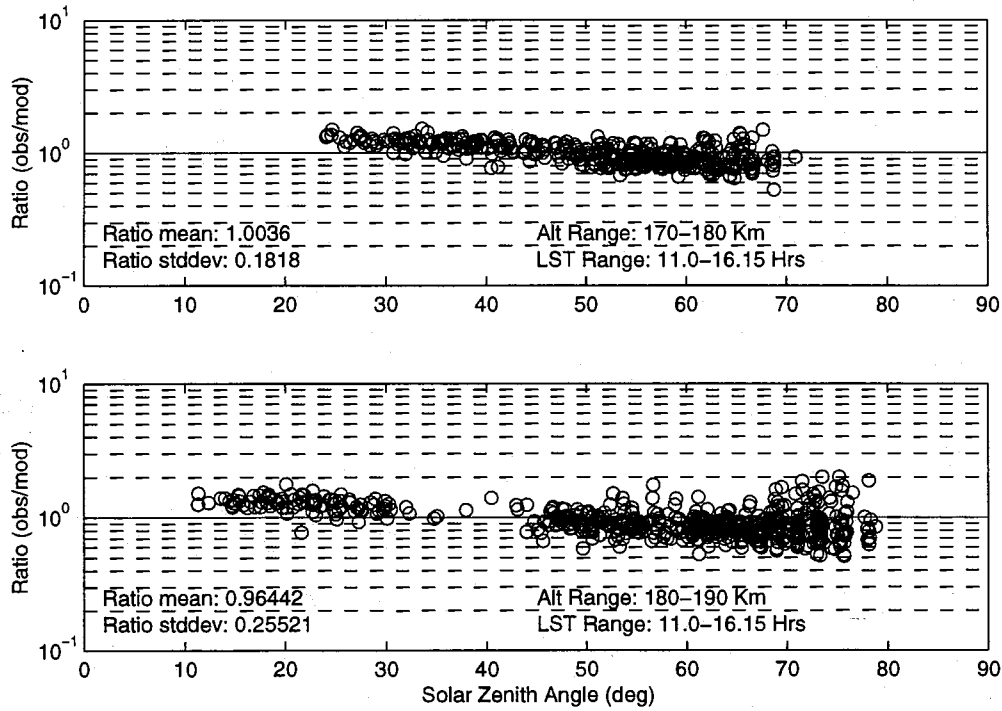


Figure 22: Day-side RWD observed/model density ratio vs. SZA using one step model

In figures 17, 18, and 19 the mean ratios show that the one step SZA and one step coefficient sets better approximate RWD than the VIRA coefficients. This is also the case in Figures 20, 21 and 22. The scatter at high SZA on each plot can be attributed to higher variability along the terminator. Notice that the one step and one step SZA coefficient set results both perform reasonably well compared to one another. This suggests that the model could be simplified to a symmetric model with respect to SZA. The plots where the density ratios are plotted versus SZA show a trend inherent with each model presented where the RWD density ratios decrease with increasing SZA. This suggests that both the symmetric and asymmetric  $T_{\infty}$  models need some sort of correction parameter inversely proportional to SZA, so that density predictions will not decrease with increasing SZA.

The VIRA model reflects data with limited coverage in latitude and solar activity since all the data used to create the VIRA model in 1985 was a low latitude and high solar activity. The newer drag data from PVO and Magellan provides better latitudinal coverage as well as measurements during a period of low solar activity. Progress made in this research with Magellan drag data is evident in comparing the one step SZA coefficient model (solid lines) with the VIRA model (dashed lines) in Figures D.1 through D.7 in Appendix D. Figures D.1 and D.2 show how each model, although difficult to distinguish the two lines, does when attempting to predict PVO drag data from 1978-80. This demonstrates that the addition of more data in this research does not detract from the one step SZA model to predict the original data set used to create the VIRA model. Figures D.3, D.4 and D.5 show the one step SZA model and the VIRA versus additional low latitude drag data obtained with PVO in 1992 and with Magellan

during Cycle 4 and Aerobraking, which were all acquired after the VIRA model was established. These plots show that both models predict density reasonably well, aside from night side variability which is difficult to predict. Upon closer inspection of residuals at the bottom of each plot, the one step SZA model tends to more accurately model the drag data as evident in the mean ratios of the SZA model are closer to one than those of the VIRA model. Figures D.6 and D.7 show each estimates of the two models as drag data enters mid latitudinal ranges in Magellan Cycle 5 and Cycle 6. As expected, the one step SZA model which includes this data in its solution more accurately estimates Magellan drag data taken at mid latitudes. These figures also reveal an issue which needs to be investigated and resolved in that both models have difficulty predicting data around 20:00 LST. This difficulty seems to be inherent in the VIRA model's mathematical formulation which is consistent between the two models shown. This issue needs to be investigated and resolved before a true update can be established. One theory to resolve this issue is the inclusion of more spherical harmonic terms. Either include tesseral harmonics of the orders already used or higher harmonics which are needed to more accurately predict the night side variability.

The remaining figures in Appendix D (pages 108 to 125) show RWD from all passes compared to the VIRA and one step SZA coefficient sets. In these plots the circles represent the RWD density measurement and the error bar as each measurement's estimated standard deviation without the factor of four multiplier, the one step SZA model is represented by a solid line, the VIRA model is represented by a dashed line, and if a coincident drag measurement occurs within five orbits it is represented by a star. Generally the difference between RWD and the one step SZA model has 2.4 standard

deviation. Some plots of RWD density passes show clean density measurements compared with the two models (for example, orbits 14474, 14520, and 14821). However, more other orbits show how the RWD varies compared to model predictions for those passes. The RWD density measurements provide a much wider sampling of density measurements with respect to latitude. However, the RWD is limited in LST coverage and also the accuracy of some RWD is seriously in doubt. This makes it difficult to resolve how to integrate the RWD with the drag data density measurements which were collected using two entirely different methods. One theory to resolve the RWD issue is to consider the following. There are 2454 RWD measurements which cover a period of about 8 hours. In this 8 hour range 471 drag data measurements exist. The ratio of the number of RWD measurements to drag measurements is about 5.2:1. Relative accuracy of drag data to RWD is acknowledged to be double. Taking these two statistics into account a RWD standard deviation multiplier can be determined by which all RWD weighting will be consistent with drag data measurements. In summary, complications still exist when combining RWD with drag data, but the RWD shows much more structure with respect to latitude than a single drag measurement per orbit.

## VII. Conclusions

The original goal of this research was to provide an update to VIRA model coefficients using more recent data sets from PVO and Magellan drag and Magellan RWD density measurements. This research does contribute to that goal, but issues remain unresolved which prevent that goal from being achieved. This research provides a solid intermediate step toward updating the VIRA model coefficients. The eventual update will assist future missions to Venus and the work done to obtain the update will enhance the general understanding of planetary atmospheres.

Future work needing to be done before updating the VIRA model include further validation of the VIRA model, reevaluation of the RWD bias, reconsideration of what coefficients to solve for with the RWD, and possibly implementing changes to the mathematical structure of VIRA to better estimate all available data. The need for validation of the model is evident in Appendix D where the drag density plots consistently show a large residual near 2000 LST for each drag density set. The source of this error must be determined. The discussion of weighted residual means and standard deviations in Section 5.4 concludes that a bias still exists between drag and RWD density measurements. Section 3.3 only analyzes drag and RWD density measurements at periapsis. An entirely new approach may be necessary to accurately determine the bias between drag data and RWD. Figure 16 shows temperature profiles of solved coefficient set models that used RWD are cooler than their respective temperature profiles of coefficient set models which did not use RWD. This suggests that either a priori coefficients be used to constrict variation in solar activity response coefficients or that these coefficients be removed from solutions which use RWD. Figures 20, 21, and 22

show a trend of decreasing density ratios with increasing SZA. This indicates that the VIRA model may require some sort of correction parameter inversely proportional to SZA, so that density predictions will not decrease with increasing SZA. Results throughout this paper regularly suggest that the VIRA model be simplified to a symmetric distribution of  $T_{\infty}$  with respect to SZA. Lastly, in order to better approximate night-side variability more spherical harmonic terms could be added.

This research set out to investigate updating the VIRA model and has accomplished valuable results. Exploration of using drag and RWD to update the VIRA model has been done and the merits have been presented. Drag data alone provides better coverage than the original PVO data set used to establish the VIRA model. The use of more recent PVO and Magellan drag data improves density estimates without significant detriment to the prediction of original PVO drag data. The RWD provides even greater coverage with respect to latitude although does bring with it problems which need to be resolved. Mid-latitude drag data slightly improves latitudinal variation within the VIRA model. The inclusion of RWD will improve the latitudinal variation of the VIRA model even further which provides incentive to resolve the complex issues associated with its implementation. This research has also demonstrated the value of using the minimum variance method with data weighting to update the VIRA model. Overall, a greater understanding of the Venus upper atmosphere and difficulties involved with updating the VIRA model has been gained.

## REFERENCES

- 1 Keating, G. M. et al., "Models of the Venus Neutral Upper Atmosphere: Structure and Composition," *Advances in Space Research*, Vol. 5, No. 11, pp. 117-171, 1985.
- 2 Espiritu, Raymond C., "Momentum Accommodation Coefficient and Venus Atmospheric Density Variation From Magellan Attitude Control Data," Masters Thesis, GWU, 1995.
- 3 Hedin, A. E. et al., "Global Empirical Model of The Venus Thermosphere," *Journal of Geophysical Research*, Vol. 88, No. A1, pp. 73-83, 1983.
- 4 Keating G. M. and Hsu, N. C., "The Venus Atmospheric Response to Solar Cycle Variations," *Geophysical Research Letters*, Vol. 20, No. 23, pp. 2751-2754, 1993.
- 5 Keating, G. M. et al., "Venus Upper Atmosphere," *Journal of Geophysical Research*, Vol. 85, No. A13, pp. 7941-7956, 1980.
- 6 Walker, James C. G., "Analytic Representation of Upper Atmosphere Densities Based on Jacchia's Static Diffusion Models," *Journal of Atmospheric Sciences*, Vol. 22, pp. 462-463, 1965.
- 7 Keating, G. M. et al., "Venus Thermosphere and Exosphere: First Satellite Drag Measurements of an Extraterrestrial Atmosphere," *Science*, Vol. 203, Number 4382, pp. 772-774, Feb. 23, 1979.
- 8 Lasher, Larry (Project Manager), "The Pioneer Missions," web site:  
[http://spaceprojects.arc.nasa.gov/Space\\_Projects/SFDivision/ThePast.html](http://spaceprojects.arc.nasa.gov/Space_Projects/SFDivision/ThePast.html).
- 9 Griffith, Douglas (Project Manager), "Magellan Summary Sheet," web site:

<http://www-b.jpl.nasa.gov/magellan/fact1.html>

- 10 Tolson, R. H., Patterson, M.T., Lyons, D. T. , "Magellan Windmill and Termination Experiments," Proceedings of International Symposium on Space Flight, pp. 265-272, 1995.
- 11 Marsden, Patrick D., "Determining the Atmospheric Density of Venus and Magellan Aerodynamic Properties From Spacecraft Attitude Data," Masters Thesis, GWU 1993.
- 12 King-Hele, Desmond, Satellite Orbits in an Atmosphere: Theory and Applications, Blackie and Son Ltd., London, 1987.
- 13 Croom, Christopher A., "Venusian Atmospheric and Magellan Properties From Attitude Control Data," Master Thesis, GWU, 1994.

## Appendices

### Appendix A: One Step SZA Model Tables and Plots

Tables and plots provided in Appendix A are provided to help construct an empirical atmospheric model of Venus in addition to equations provided in Section II.

The plots following the tables use coefficients from one step SZA coefficient set and are reference plots to be used in confirmation of results.

Local Solar Time (hours)	Hydrogen Number Density (cm <sup>-3</sup> )
1	2.54e7
2	3.88e7
3	4.98e7
4	6.11e7
5	1.06e7
6	1.87e6
7	7.66e5
8	3.27e5
9	2.05e5
10	1.15e5
11	1.03e5
12	9.16e4
13	8.53e4
14	7.93e4
15	8.55e4
16	9.17e4
17	1.82e5
18	3.95e5
19	9.75e5
20	2.39e6
21	4.44e6
22	8.40e6
23	1.19e7
24	1.69e7

Table A.1 : Boundary condition Hydrogen at 150 km vs. local solar time

Time	Temperature(K)	Time	Temperature(K)	Time	Temperature(K)	Time	Temperature(K)
0:00	143.02	6:00	162.96	12:00	180.32	18:00	160.12
0:10	142.90	6:10	164.92	12:10	180.42	18:10	158.70
0:20	142.86	6:20	166.82	12:20	180.44	18:20	157.33
0:30	142.87	6:30	168.62	12:30	180.38	18:30	156.02
0:40	142.96	6:40	170.31	12:40	180.22	18:40	154.79
0:50	143.11	6:50	171.88	12:50	179.99	18:50	153.65
1:00	143.33	7:00	173.32	13:00	179.68	19:00	152.61
1:10	143.62	7:10	174.62	13:10	179.31	19:10	151.65
1:20	143.96	7:20	175.78	13:20	178.91	19:20	150.81
1:30	144.34	7:30	176.79	13:30	178.51	19:30	150.10
1:40	144.73	7:40	177.65	13:40	178.11	19:40	149.53
1:50	145.09	7:50	178.38	13:50	177.75	19:50	149.12
2:00	145.39	8:00	178.97	14:00	177.45	20:00	148.88
2:10	145.58	8:10	179.44	14:10	177.21	20:10	148.81
2:20	145.64	8:20	179.78	14:20	177.05	20:20	148.90
2:30	145.54	8:30	180.01	14:30	176.95	20:30	149.15
2:40	145.30	8:40	180.15	14:40	176.90	20:40	149.53
2:50	144.93	8:50	180.19	14:50	176.89	20:50	150.00
3:00	144.49	9:00	180.16	15:00	176.89	21:00	150.50
3:10	144.04	9:10	180.05	15:10	176.86	21:10	150.98
3:20	143.65	9:20	179.90	15:20	176.77	21:20	151.36
3:30	143.38	9:30	179.70	15:30	176.60	21:30	151.56
3:40	143.29	9:40	179.48	15:40	176.31	21:40	151.55
3:50	143.43	9:50	179.26	15:50	175.88	21:50	151.30
4:00	143.82	10:00	179.05	16:00	175.31	22:00	150.81
4:10	144.47	10:10	178.88	16:10	174.58	22:10	150.12
4:20	145.37	10:20	178.76	16:20	173.71	22:20	149.28
4:30	146.52	10:30	178.71	16:30	172.69	22:30	148.35
4:40	147.89	10:40	178.72	16:40	171.54	22:40	147.41
4:50	149.46	10:50	178.81	16:50	170.28	22:50	146.51
5:00	151.18	11:00	178.97	17:00	168.94	23:00	145.69
5:10	152.99	11:10	179.17	17:10	167.52	23:10	144.97
5:20	154.91	11:20	179.42	17:20	166.06	23:20	144.37
5:30	156.89	11:30	179.68	17:30	164.57	23:30	143.88
5:40	158.92	11:40	179.93	17:40	163.07	23:40	143.50
5:50	160.95	11:50	180.15	17:50	161.58	23:50	143.22

Table A.2 : Temperature at 115 km vs. local solar time

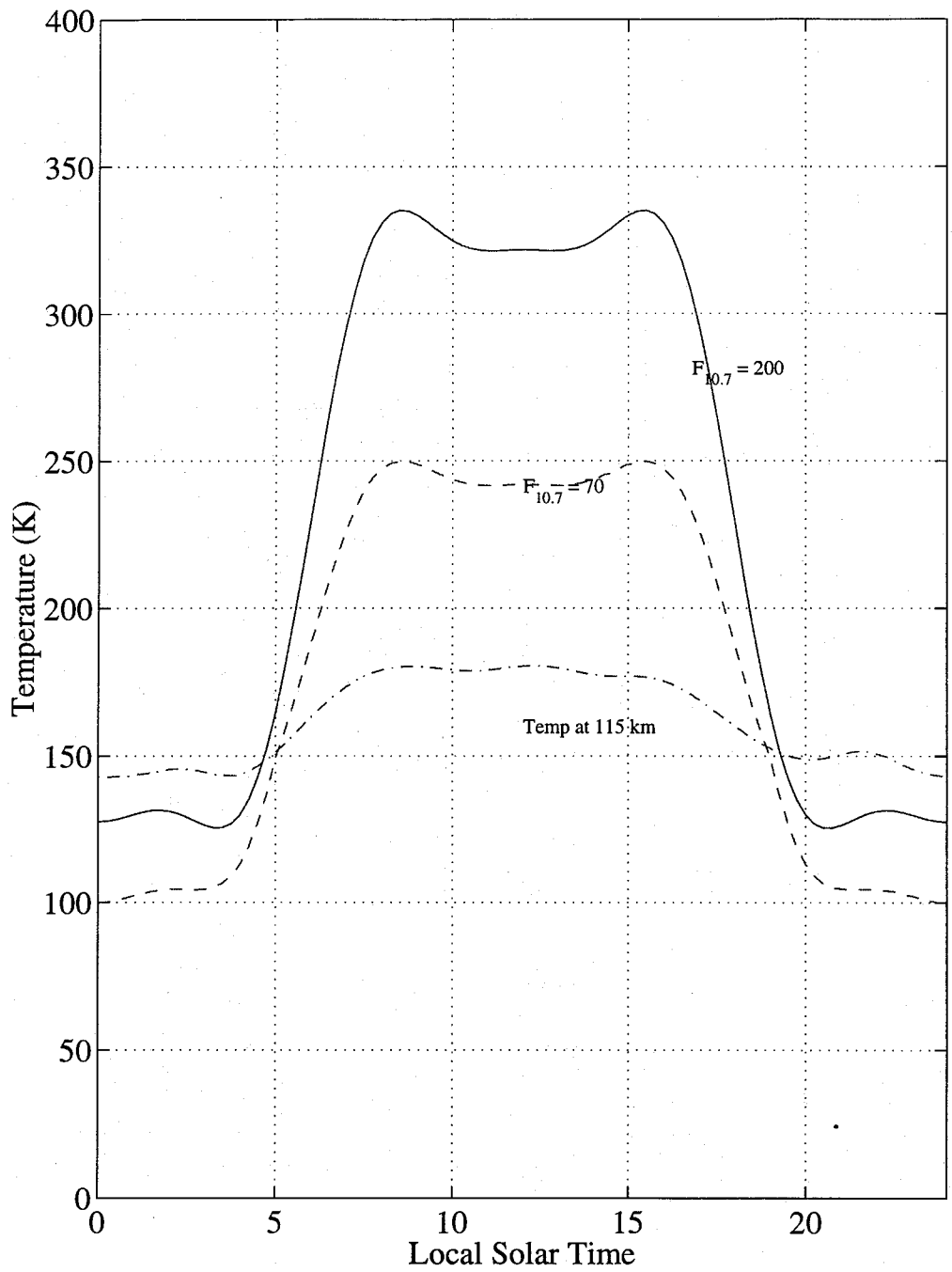


Figure A.1 : Temperature at 115 km and exospheric temp. for F<sub>10.7</sub> at 200 and 70

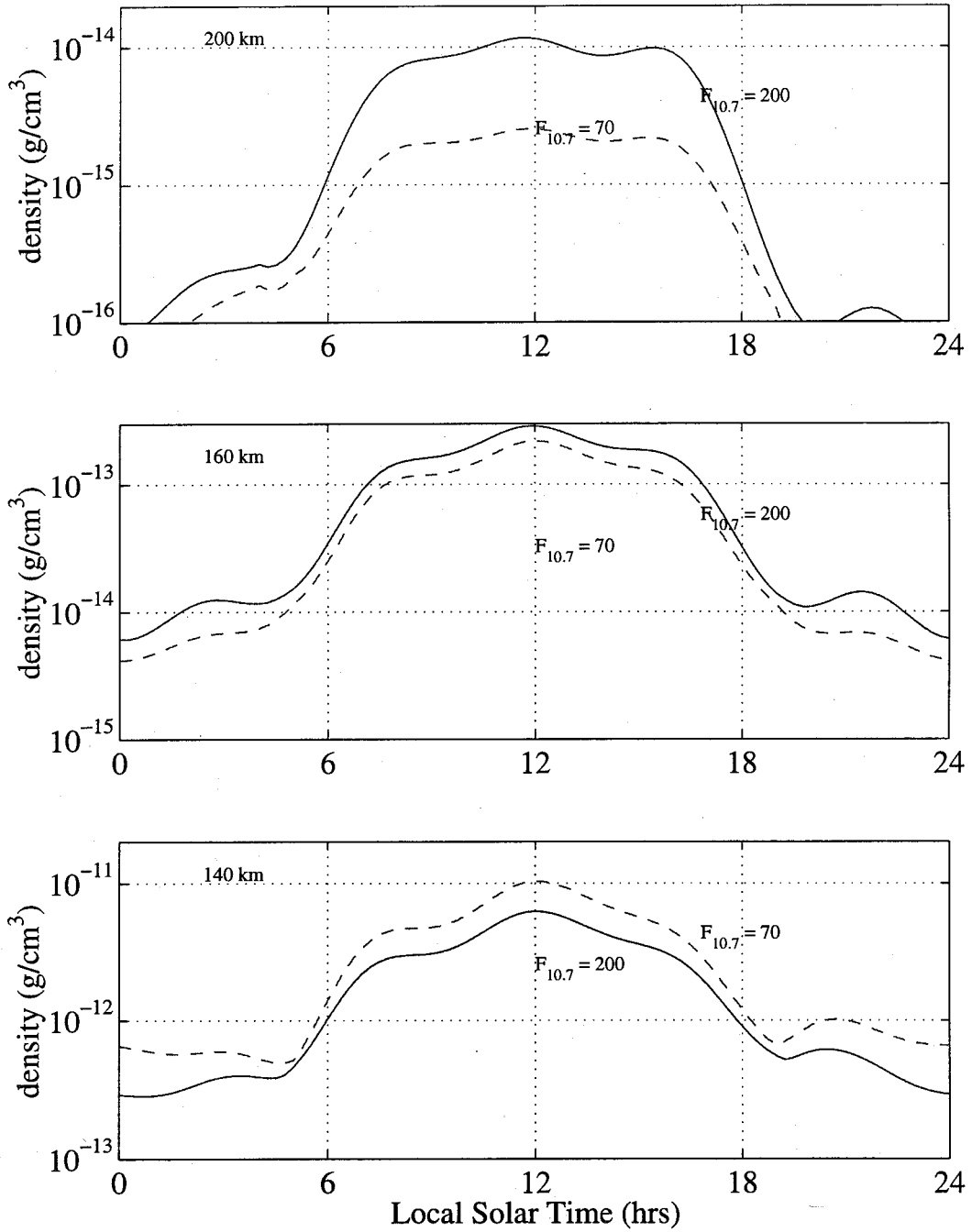


Figure A.2 : Density at 200, 160, and 140 km for F<sub>10.7</sub> at 200 and 70 (Lat = 0°)

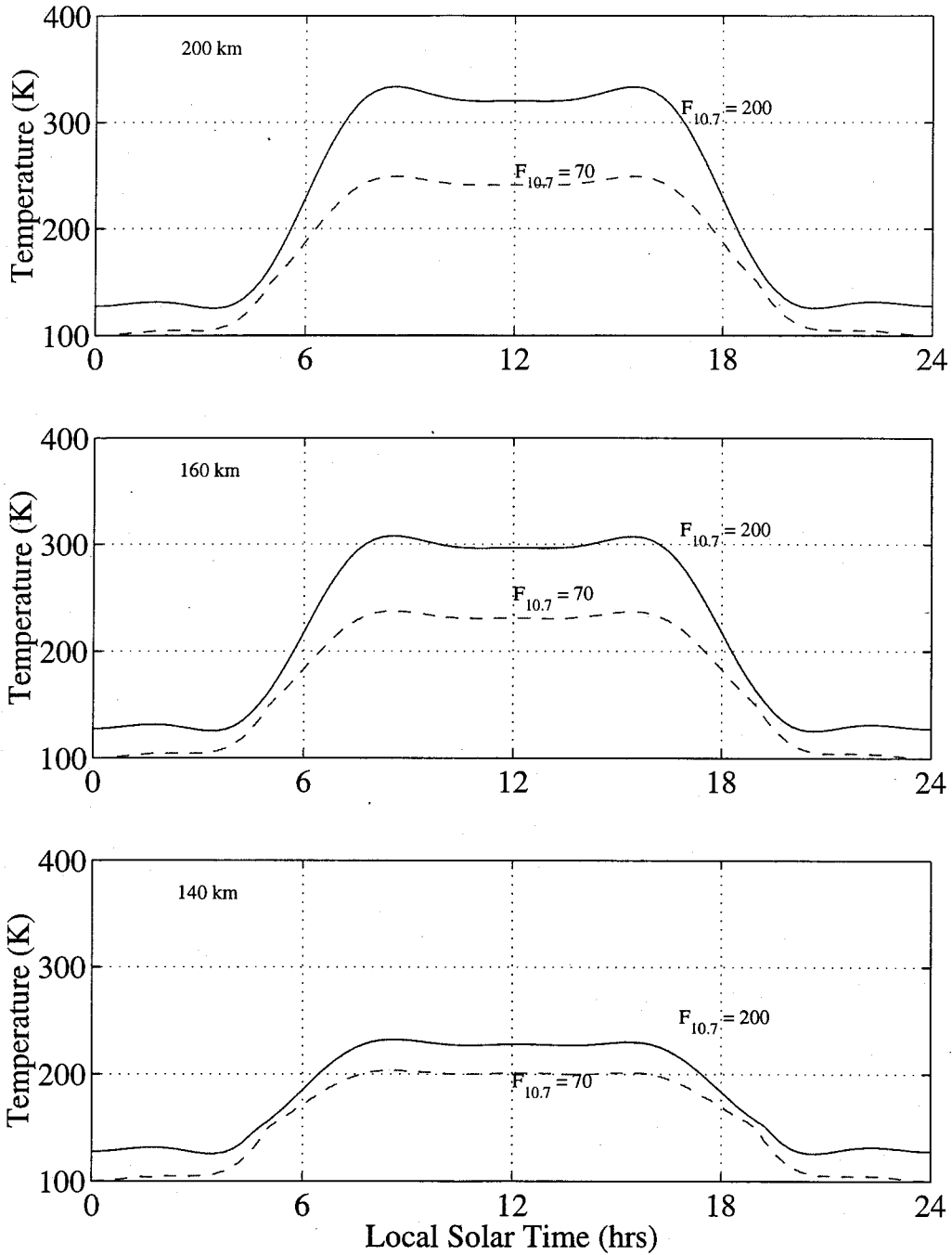


Figure A.3: Temperature at 200, 160, and 140 km for  $F_{10.7}$  at 200 and 70 (Lat=0°)

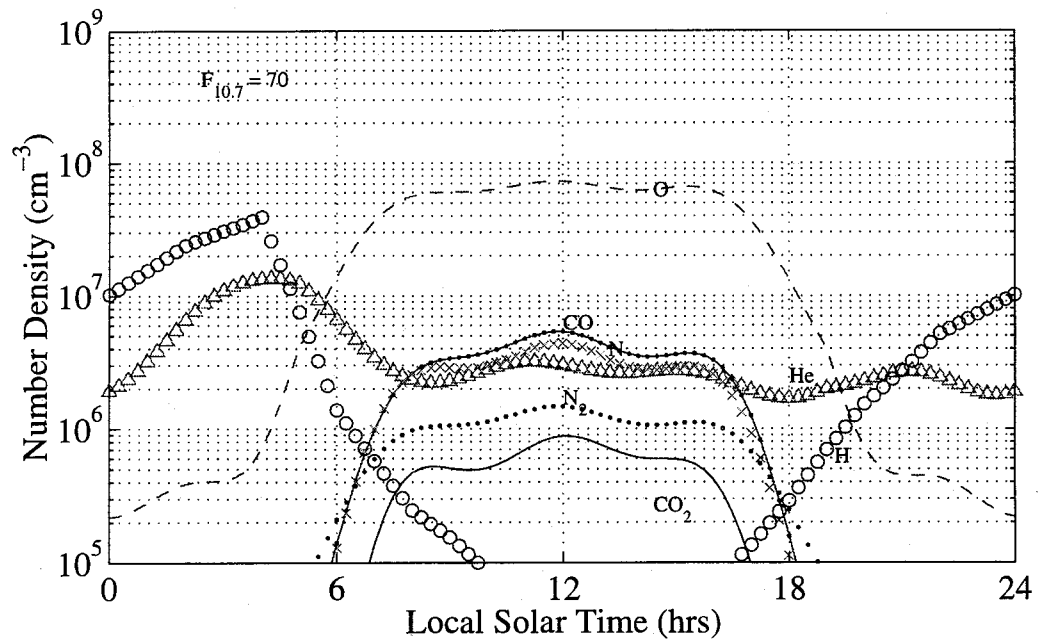
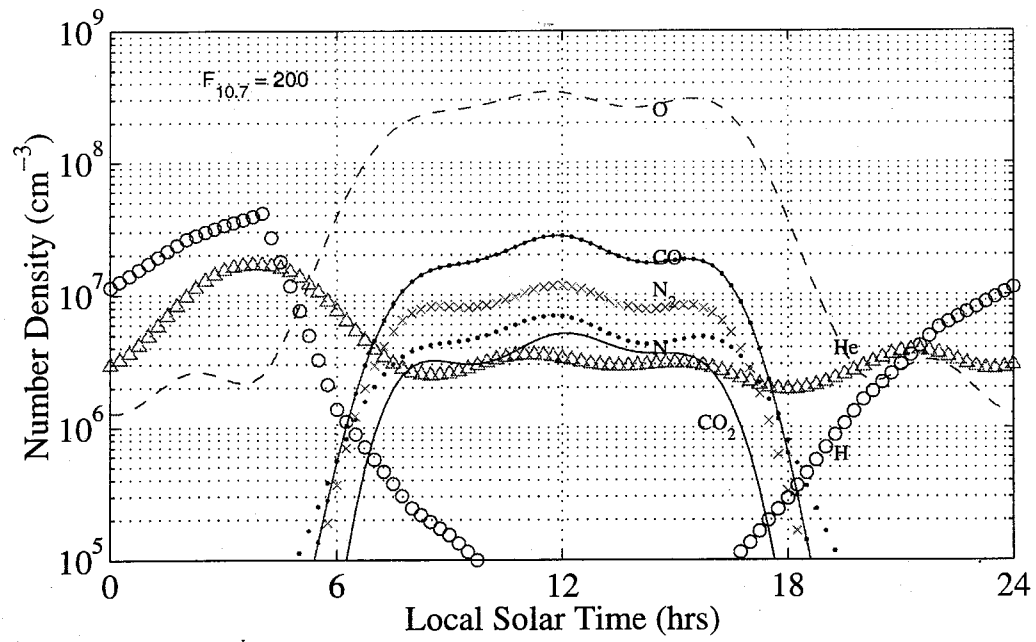


Figure A.4 : Number Densities at 200 km for  $F_{10.7}$  at 200 and 70 (Lat =  $0^\circ$ )

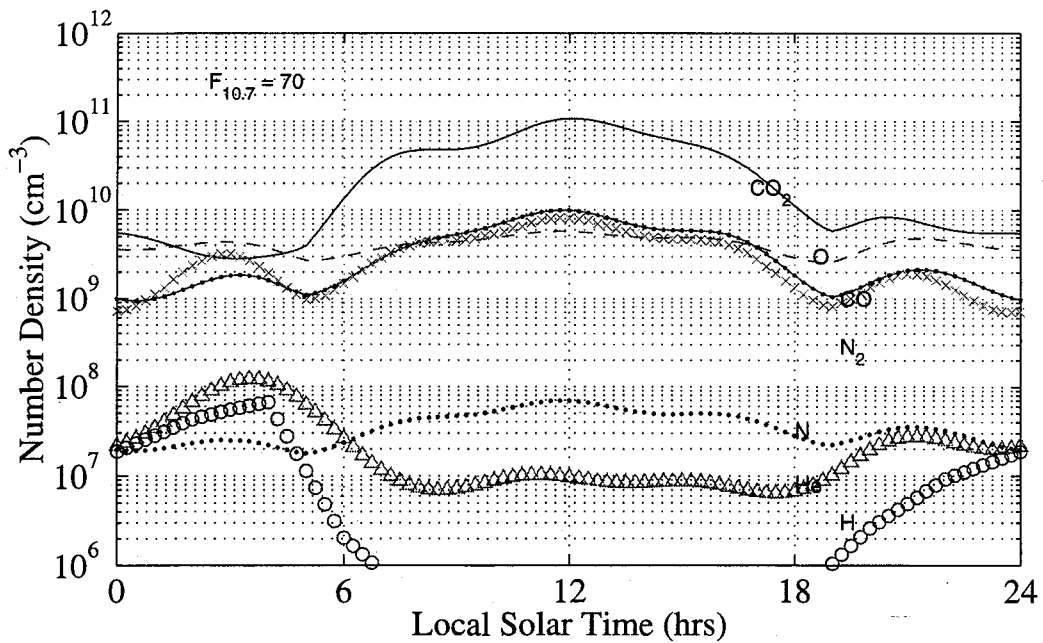
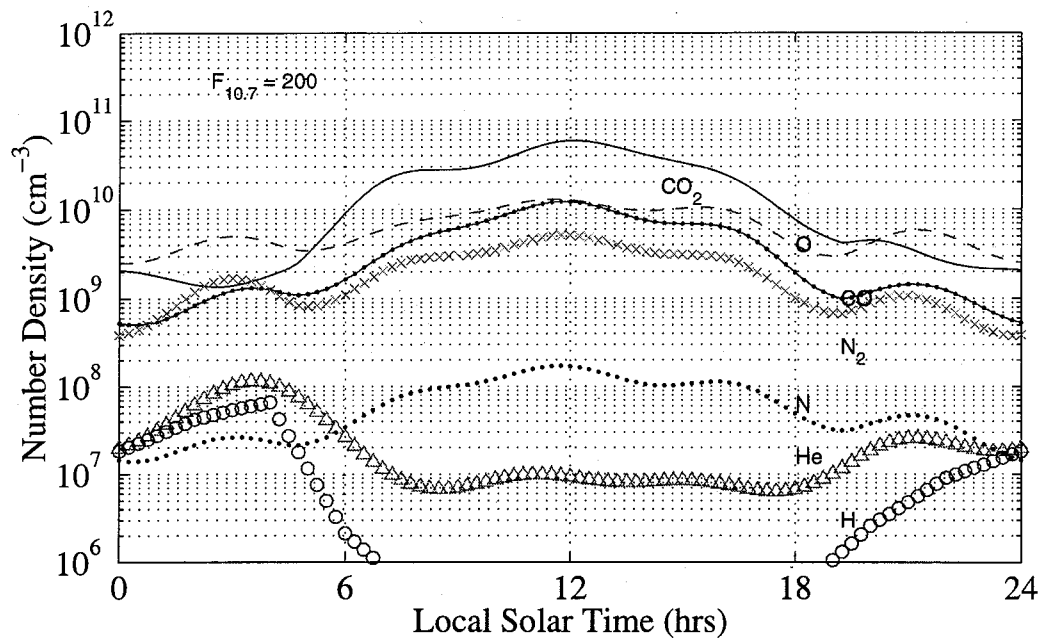


Figure A.5 : Number Densities at 140 km for  $F_{10.7}$  at 200 and 70 (Lat =  $0^\circ$ )

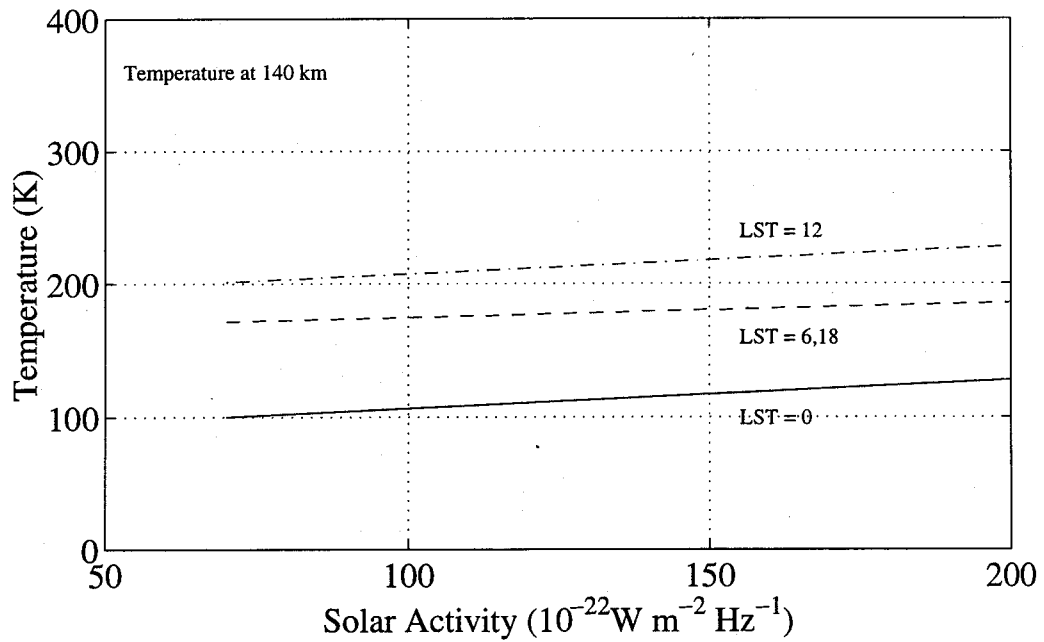
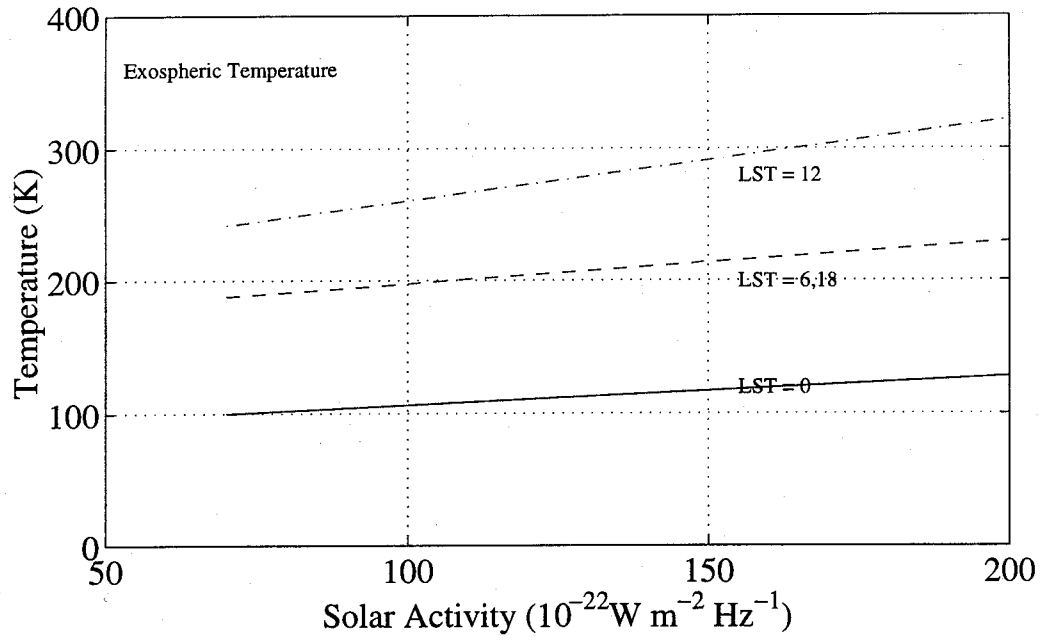


Figure A.6 : Temperature vs. solar activity at LST of 0, 6, 12, and 18

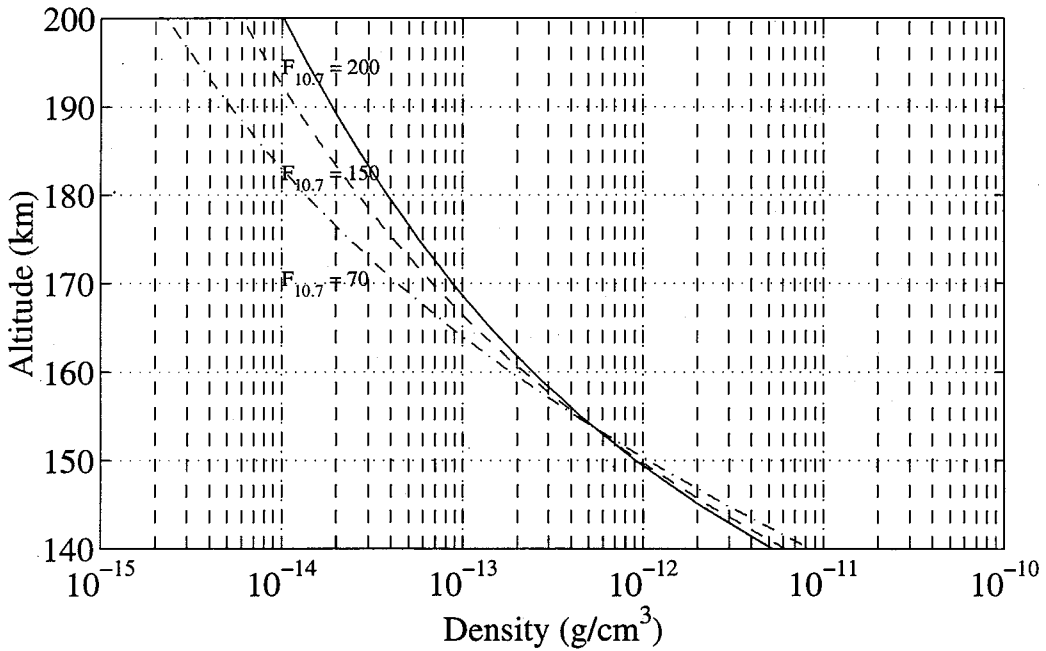
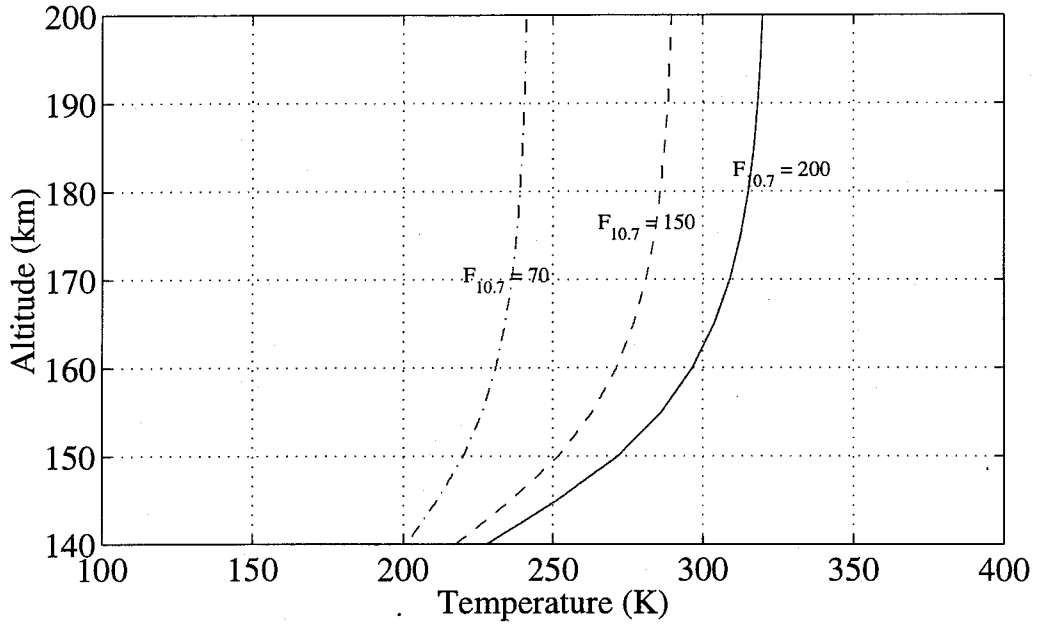


Figure A.7: Temperature and density profiles vs. altitude at F<sub>10.7</sub> at 200, 150 and 70

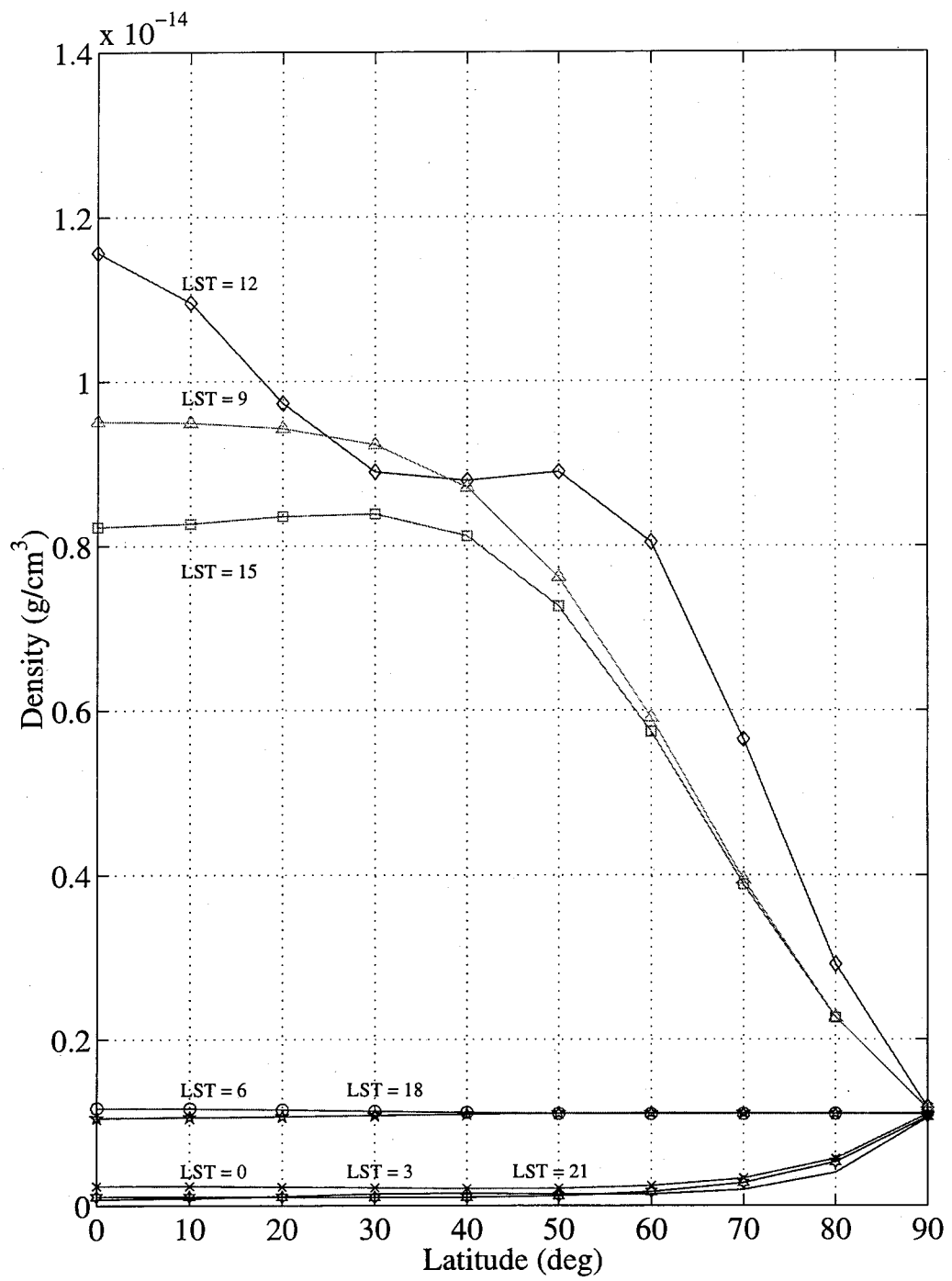


Figure A.8 : Diurnal variation of density vs. latitude at F<sub>10.7</sub> of 200

## **Appendix B: Plots of Data Used to Update One Step SZA Model**

Plots in Appendix B show the dispersion of the data set used by the minimum variance method to update model coefficients. There are 3791 data points used in analysis for this research. There are 1337 drag density measurements and 2454 RWD density measurements. The data is represented in plots of data point versus: orbit number (RWD assigned orbits starting at 20000); local solar time; altitude; observed density; daily  $F_{10.7}$   $\text{cm}^2$  solar flux; 81 day average  $F_{10.7}$   $\text{cm}^2$  solar flux; latitude; sigma; solar zenith angle; assigned weight for minimum variance method.

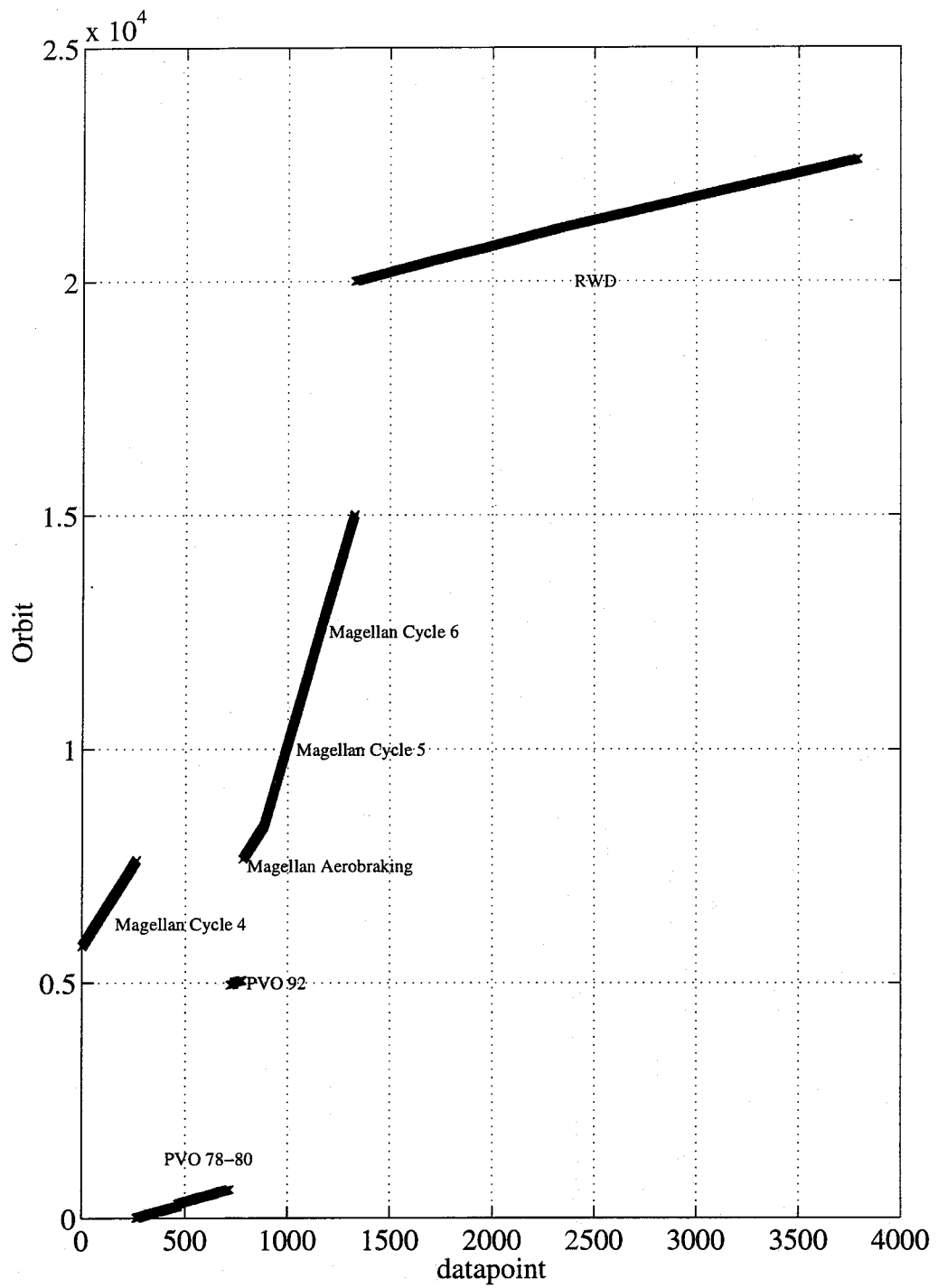


Figure B.1 : Orbit numbers of data set

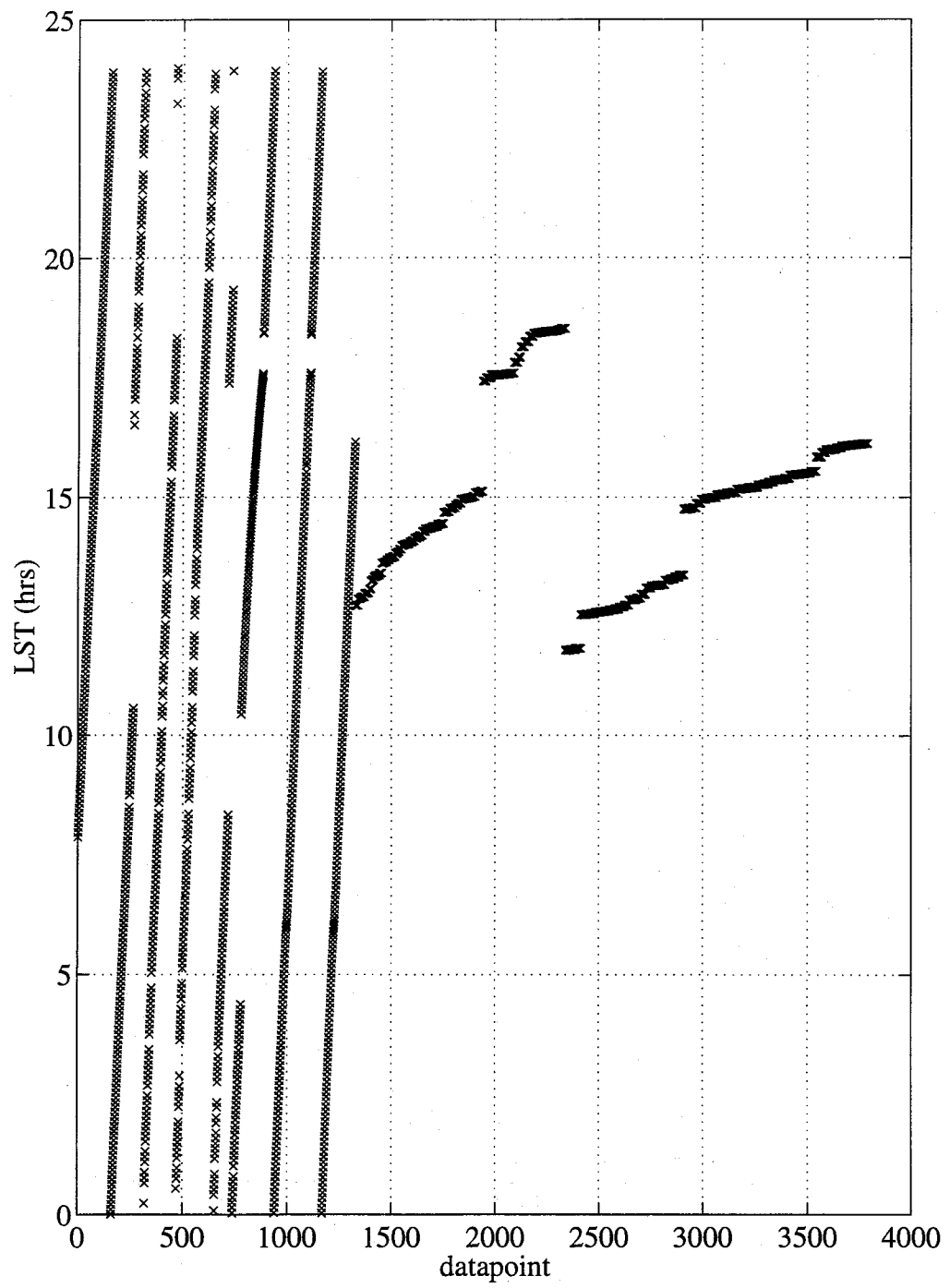


Figure B.2 : Local solar times of data set

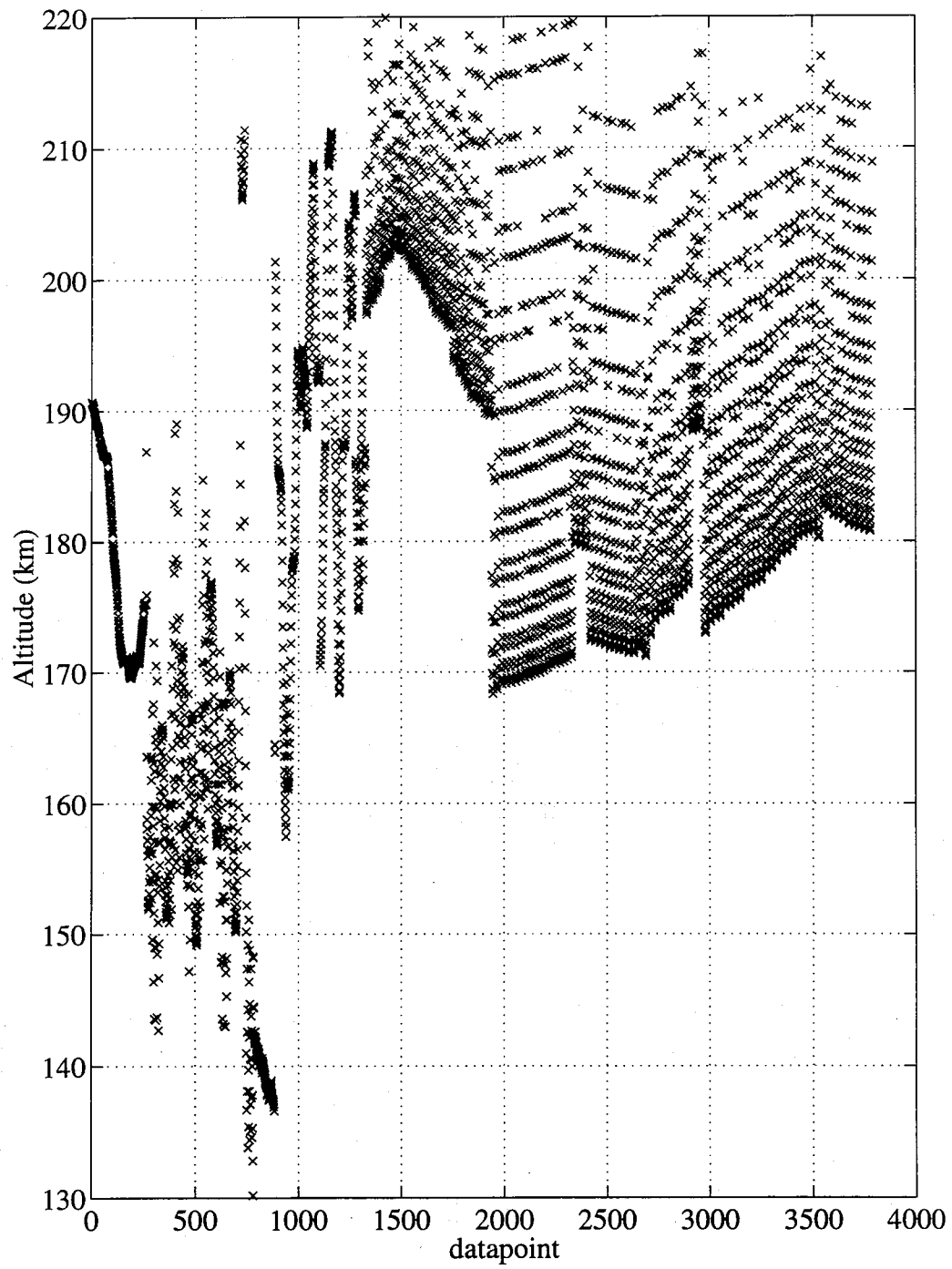


Figure B.3 : Altitudes of data set

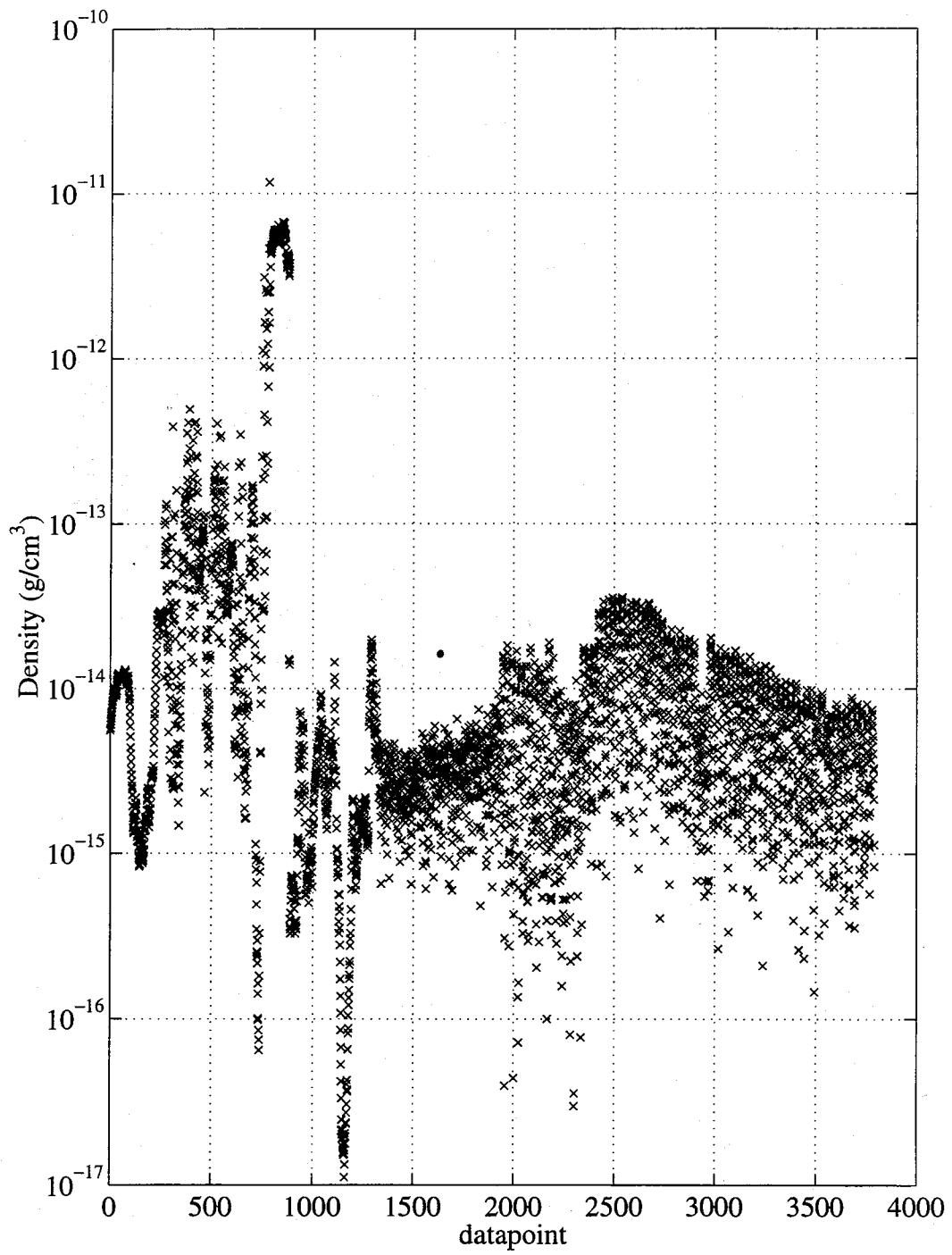


Figure B.4 : Densities of data set

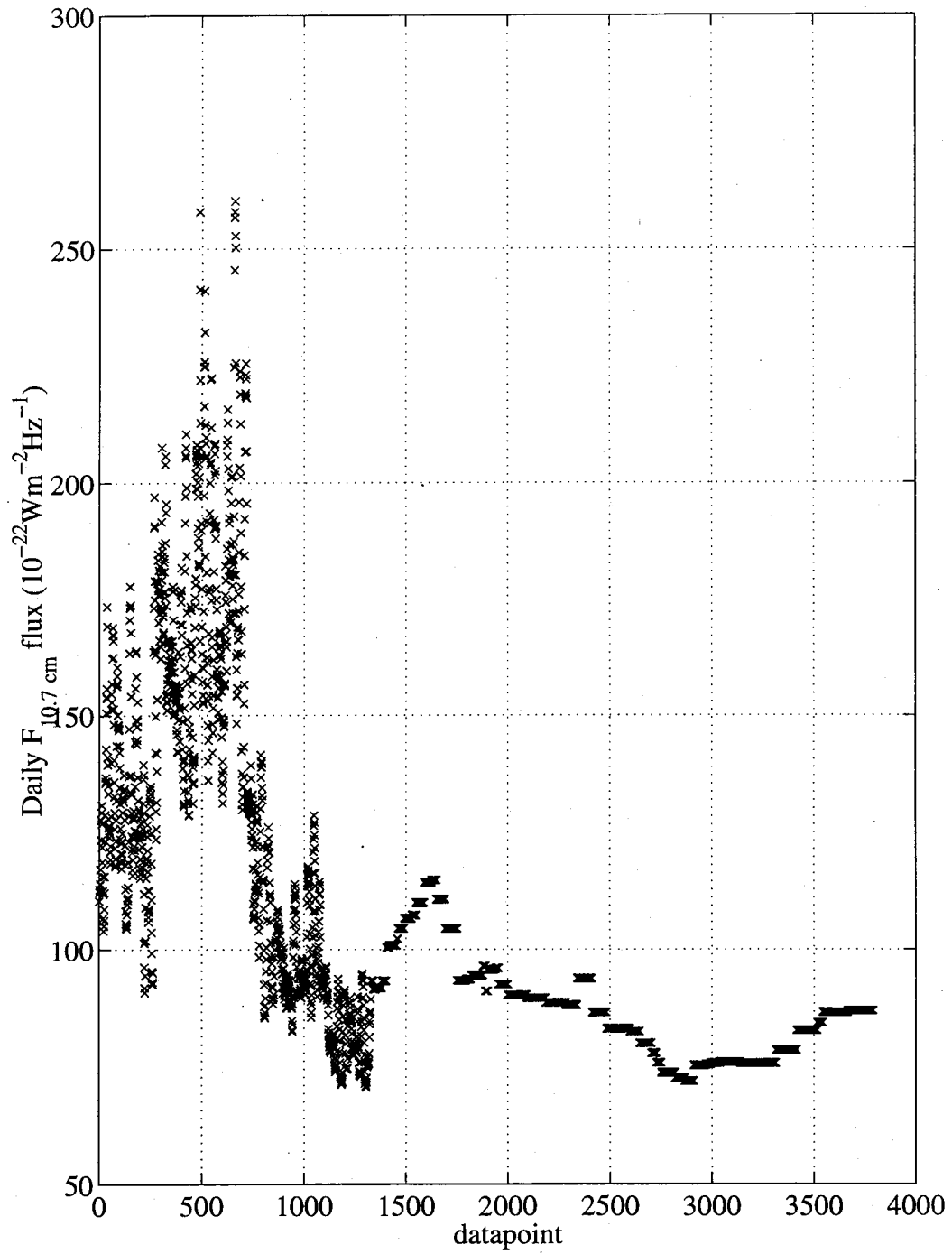


Figure B.5 : Daily F<sub>10.7</sub> solar flux of data set

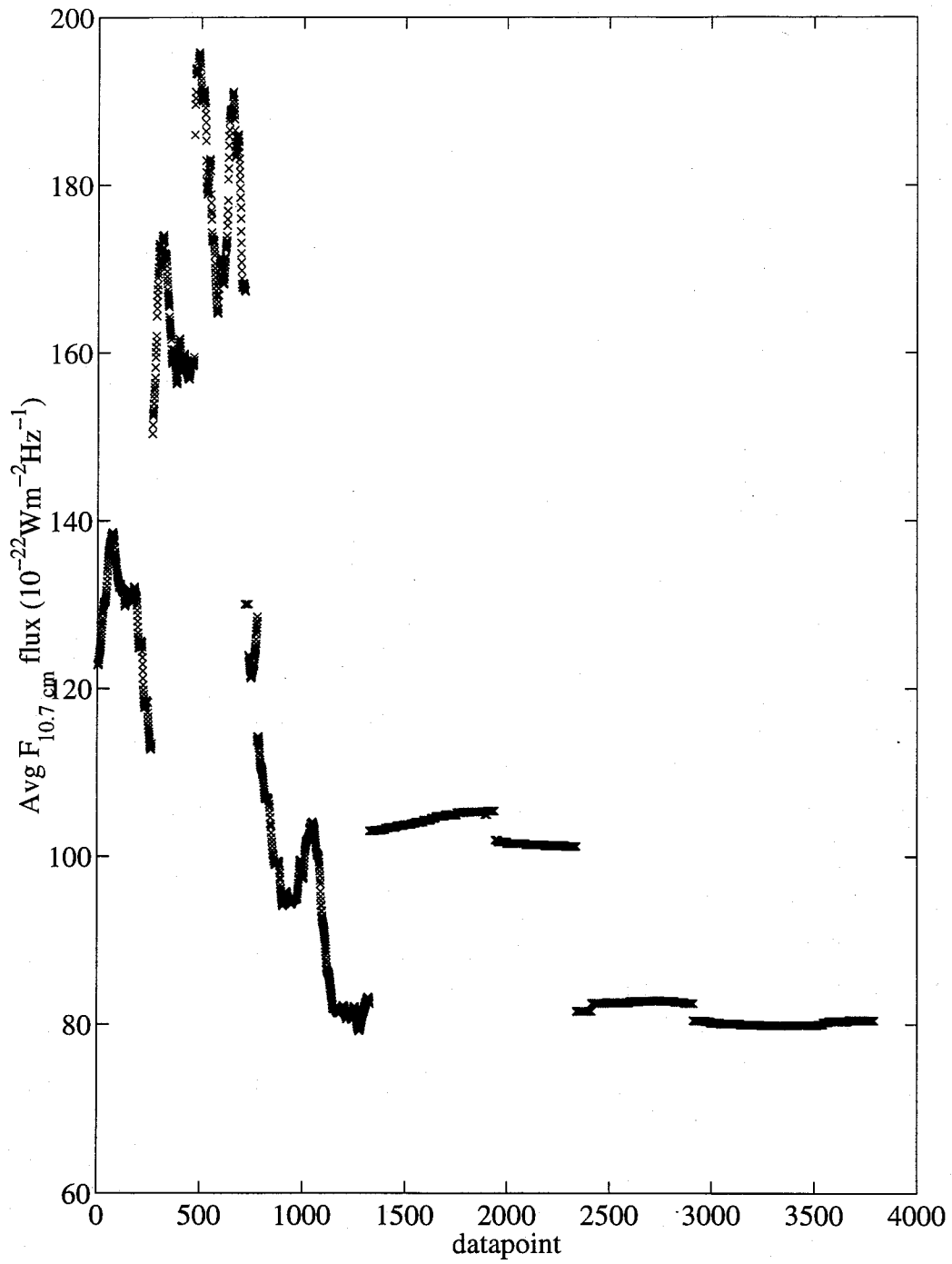


Figure B.6 : 81 day average  $F_{10.7}$  solar flux of data set

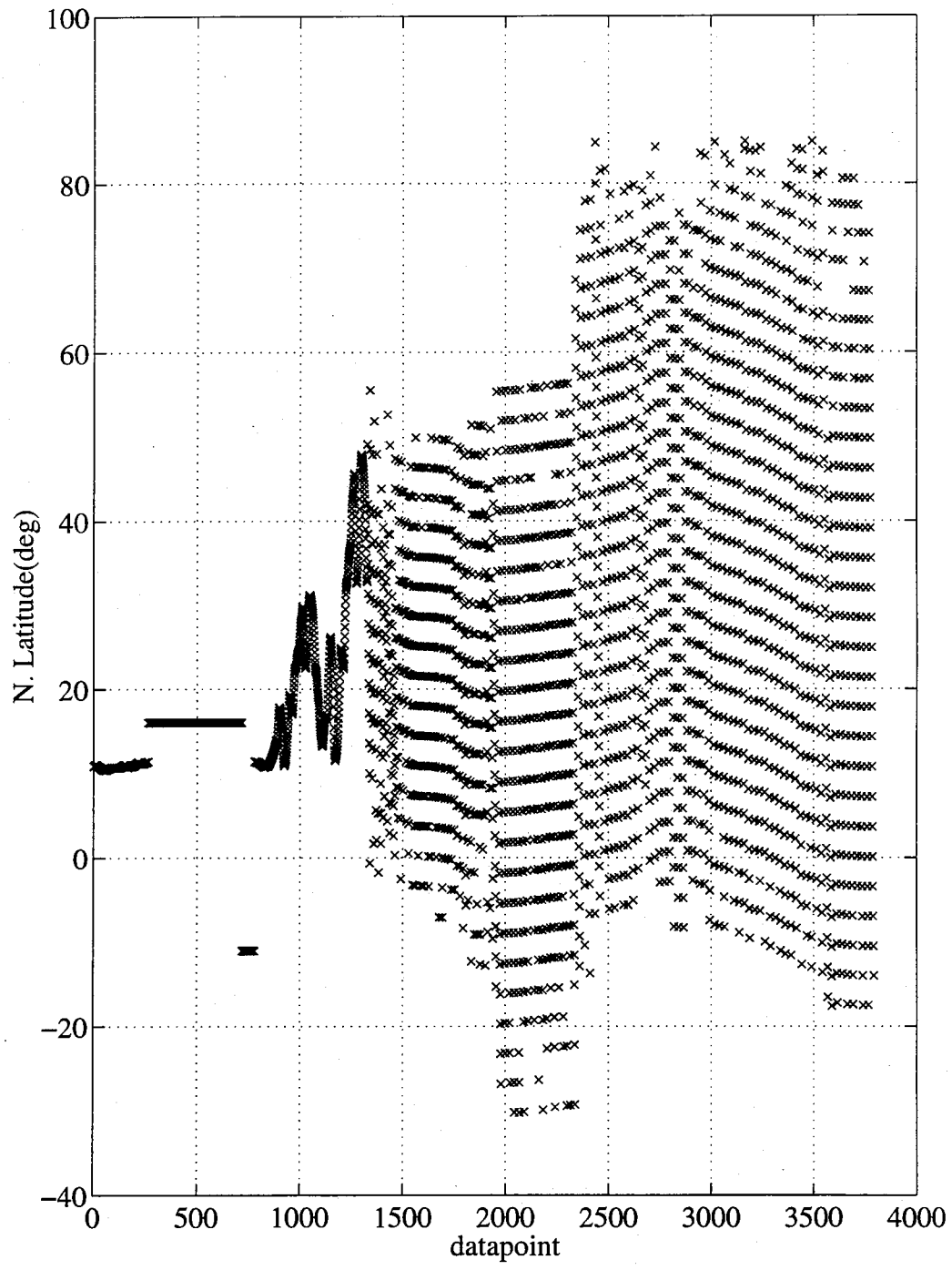


Figure B.7 : Latitudes of data set

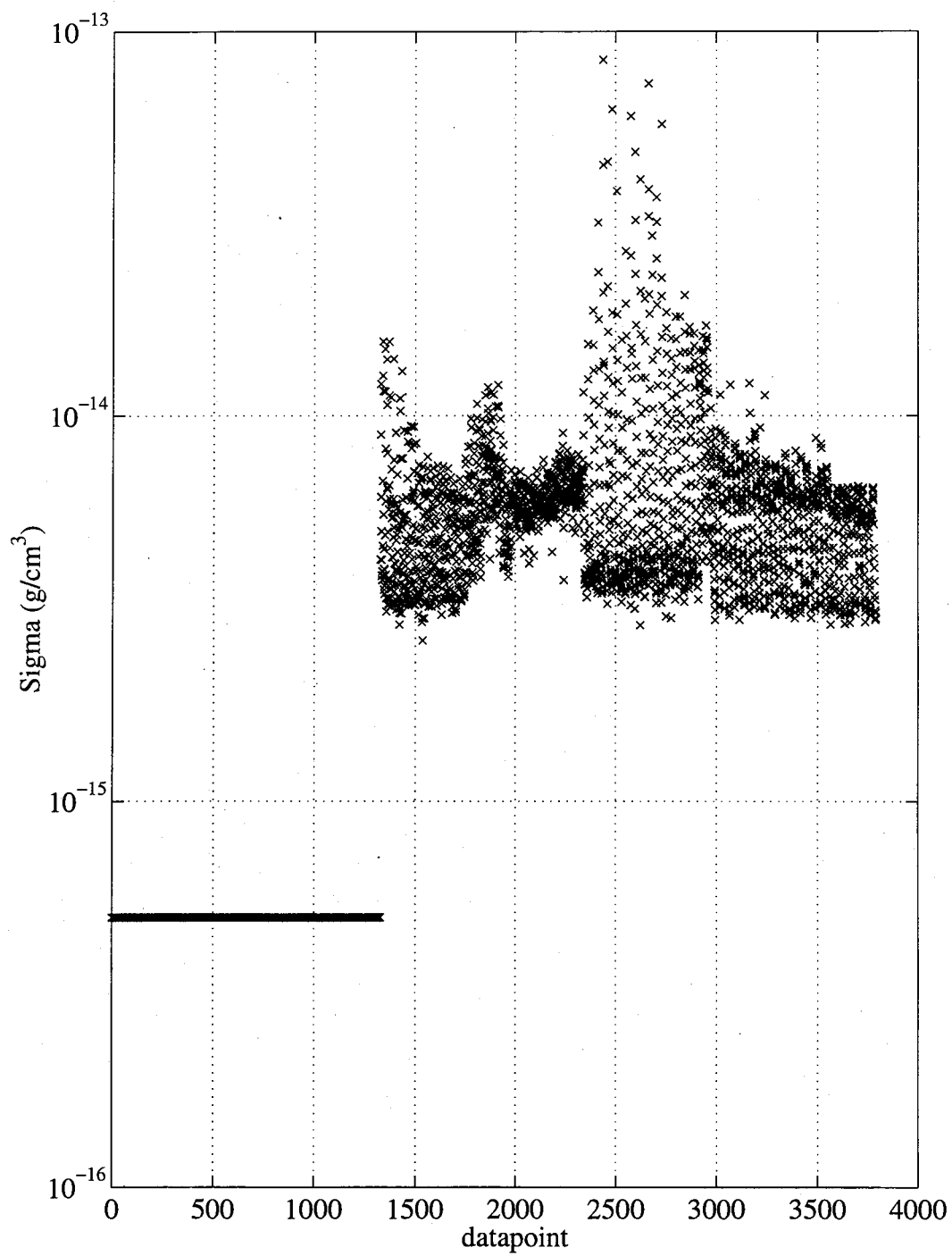


Figure B.8 : Density Measurement Standard Deviations of data set

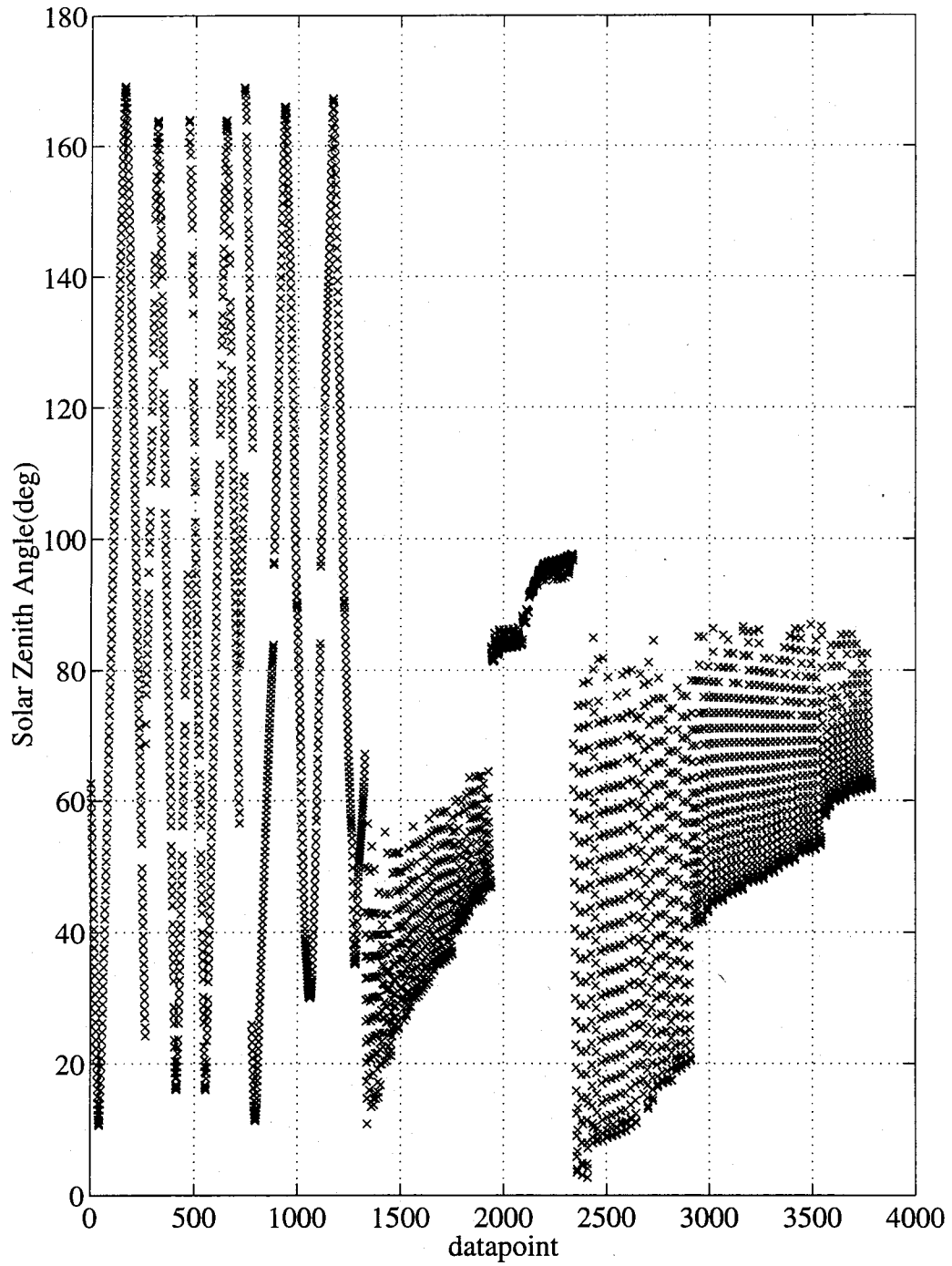


Figure B.9 : Solar zenith angles of data set

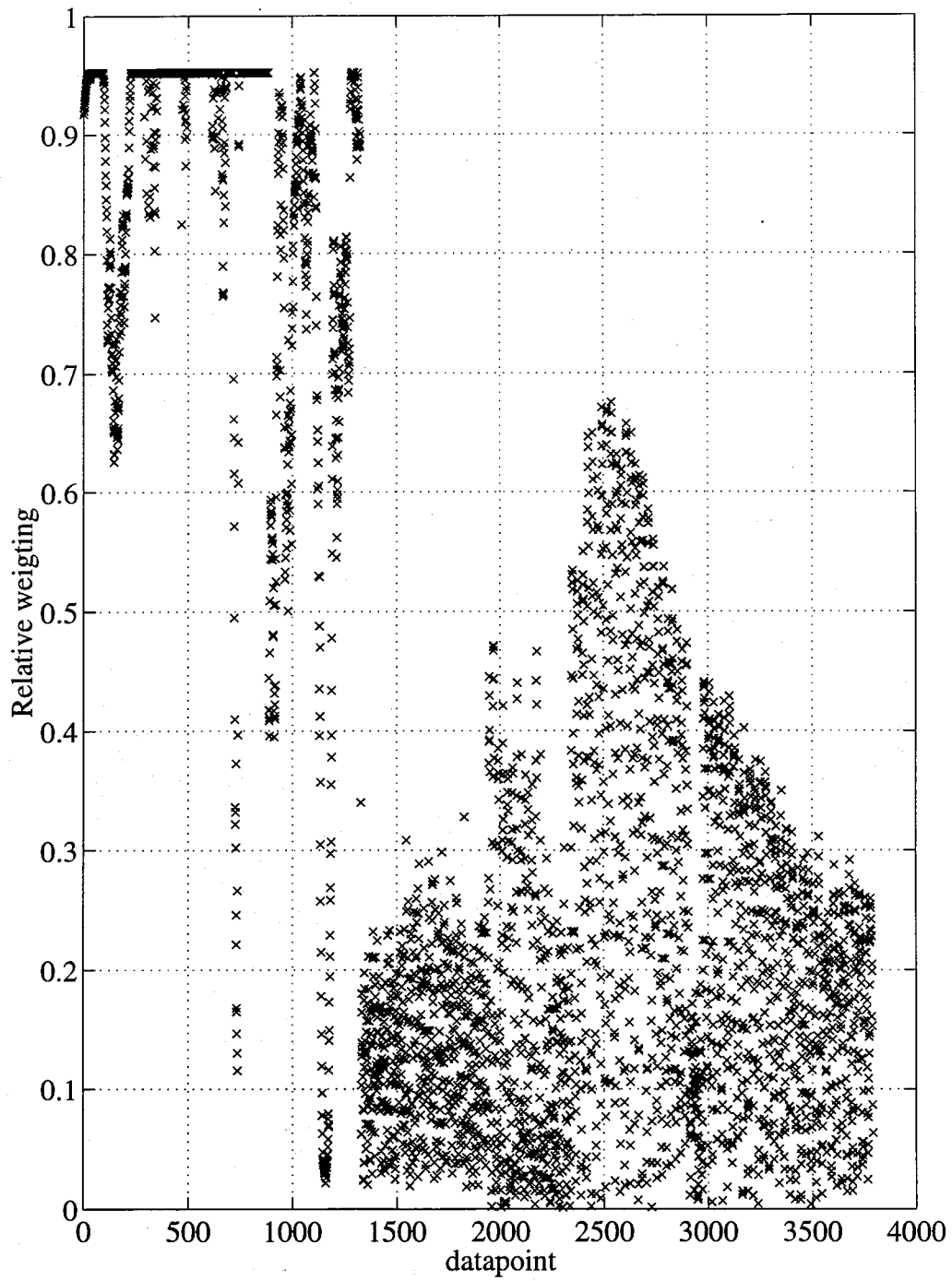


Figure B.10 : Relative weighting of data set

## **Appendix C: Coefficient Solution Results and Correlation Tables**

The following pages contain tables of solution case results for the five coefficient sets from Section V. The first tables list coefficients solved during minimum variance, the converged result, the sigma measure of uncertainty, and the ratio of the sigma measure over the value to indicate how credible the converged result is for that estimated coefficient. The second table for each section are tables of correlation percentages between coefficients solved for during each case.



## 2 Drag One Step Coefficients and Sigmas, and Correlations Tables

Coefficient	Value	Sigma	Sigma/Value
(1) = CO2 k	1.18E+00	0.1803	0.152461
(2) = O k	9.47E-01	0.0705	0.074439
(3) = EXOT avg	2.42E+02	7.8163	0.032269
(4) = EXOT a10	6.09E-01	0.0229	0.037584
(5) = EXOT b11	-5.39E-02	0.0145	0.269117
(6) = EXOT a20	-4.67E-02	0.0242	0.518434
(7) = EXOT b22	-1.41E-02	0.005	0.354761
(8) = EXOT a30	-2.48E-01	0.0267	0.107553
(9) = EXOT b33	3.02E-03	0.001	0.331455
(10) = EXOT a40	-1.90E-02	0.0279	1.466183
(11) = EXOT b44	1.72E-04	0.0002	1.159622
(12) = EXOT a50	5.40E-02	0.0249	0.461496
(13) = EXOT b55	-2.78E-06	0	0
(14) = EXOT f avg	1.73E-03	0.0004	0.231147
(15) = EXOT f	4.31E-04	0.0005	1.15899
(16) = EXOT alpha	7.34E-04	0.0003	0.408452
(17) = CO2 f avg	-1.34E-03	0.0009	0.673703
(18) = O f avg	4.25E-03	0.0019	0.44688
(19) = He k	2.55E+00	0.4141	0.162647





#### 4. One Step Coefficients and Sigmas, and Correlations Tables

Coefficient	Values	Sigmas	Sigma/Value
(1) = CO2 k	1.15E+00	0.1803	0.156728
(2) = O k	1.03E+00	0.0666	0.064786
(3) = EXOT avg	2.30E+02	6.2131	0.026976
(4) = EXOT a10	5.95E-01	0.0227	0.038174
(5) = EXOT b11	-5.85E-02	0.0118	0.201782
(6) = EXOT a20	-3.16E-02	0.0193	0.610798
(7) = EXOT b22	-1.43E-02	0.0041	0.286553
(8) = EXOT a30	-2.30E-01	0.0187	0.081167
(9) = EXOT b33	2.63E-03	0.0008	0.303778
(10) = EXOT a40	-1.00E-02	0.0167	1.668665
(11) = EXOT b44	2.00E-04	0.0001	0.500075
(12) = EXOT a50	3.86E-02	0.0193	0.500597
(13) = EXOT b55	-1.22E-05	0	0
(14) = EXOT f avg	1.45E-03	0.0002	0.138408
(15) = EXOT f	-9.33E-05	0.0003	3.216468
(16) = EXOT alpha	4.95E-04	0.0003	0.605742
(17) = CO2 f avg	-1.33E-03	0.0008	0.603045
(18) = O f avg	4.15E-03	0.0014	0.337602
(19) = He k	1.52E+00	0.3487	0.229423



## 5. Three Step Coefficients and Sigmas, and Correlations Tables

Step One

Coefficient	Value	Sigma	Sigma/Value
(1) = CO2 k	1.25E+00	0.0666	0.053097
(2) = O k	9.97E-01	0.0476	0.047721
(3) = EXOT avg	2.32E+02	3.4365	0.014837
(4) = EXOT a10	5.89E-01	0.012	0.020388
(5) = EXOT b11	-5.97E-02	0.0113	0.189308
(6) = EXOT a20	-2.70E-02	0.0132	0.489269
(7) = EXOT b22	-1.43E-02	0.0036	0.251907
(8) = EXOT a30	-2.29E-01	0.0166	0.072508
(9) = EXOT b33	2.75E-03	0.0008	0.290508
(10) = EXOT a40	-9.42E-03	0.0149	1.582514
(11) = EXOT b44	1.92E-04	0.0001	0.519696
(12) = EXOT a50	3.35E-02	0.0156	0.465686
(13) = EXOT b55	-1.18E-05	0	0

(1)	100												
(2)	-56.4	100											
(3)	45.5	-92.3	100										
(4)	-11.2	-2.4	2.6	100									
(5)	-12.3	9.4	10.8	13.3	100								
(6)	-9.9	13.3	-16.9	41.3	-16.1	100							
(7)	13.2	2	-21.3	-20.8	-41.4	-19	100						
(8)	6.2	4.2	-3.1	-45.2	-14.7	5.9	6.6	100					
(9)	1.5	-11.2	14.1	39.8	-12.8	48.1	7.1	7.1	100				
(10)	11.5	-5.4	5	15	-3.5	-31.6	34.8	5.9	5.9	100			
(11)	-2.7	1.7	-2.2	-23.9	16.7	-39.7	-2.5	-22.7	-22.7	-8.6	100		
(12)	2.1	-0.4	-6.5	-30.4	-2.3	-2.7	14.9	-24.4	-24.5	16.5	9.4	100	
(13)	0.7	4	1.5	-7.5	9.3	2.6	5.5	38.3	-3	28.5	-20.1	-2.5	100
(1)		(2)	(3)	(4)	(5)	(6)	(7)	(8)	(9)	(10)	(11)	(12)	(13)

Step Two

Coefficient	Value	Sigma	Sigma/Value Ratio
(1) = EXOT avg	2.32E+02	5.321	0.022973
(2) = EXOT f avg	1.34E-03	0.0002	0.149198
(3) = EXOT f	-6.18E-05	0.0003	4.857592
(4) = CO2 f avg	-8.68E-04	0.0003	0.345531
(5) = O f avg	4.21E-03	0.001	0.237643

Correlation Matrix

(1)	100				
(2)	31.6	100			
(3)	9.6	-7.3	100		
(4)	-23.2	5.9	-10.1	100	
(5)	39.4	-73.3	13.5	-34	100
	(1)	(2)	(3)	(4)	(5)

97 Step Three

Coefficient	Values	Sigmas	Sigma/Value Ratio
(1) = EXOT avg	2.32E+02	5.2473	0.022655
(2) = EXOT alpha	6.01E-04	0.0002	0.332591
(3) = He k	2.19E+00	0.3084	0.140951

Correlation Matrix

(1)	100		
(2)	75.1	100	
(3)	4.3	55.2	100
	(1)	(2)	(3)

## 6. Table of Previous Venus Thermosphere Model Coefficients

Coefficient	Hedin	VIRA	KH 93
CO2 k	1.00E+00	1.12E+00	1.03E+00
O k	1.00E+00	9.70E-01	1.01E+00
EXOT avg	2.28E+02	2.29E+02	2.36E+02
EXOT a10	5.74E-01	5.92E-01	5.82E-01
EXOT b11	-1.06E-01	0.00E+00	-8.39E-03
EXOT a20	-1.54E-01	-6.30E-02	-1.22E-01
EXOT b22	-7.12E-03	0.00E+00	-1.47E-02
EXOT a30	-1.83E-01	-2.34E-01	-2.30E-01
EXOT b33	4.41E-03	0.00E+00	1.33E-03
EXOT a40	1.22E-01	2.40E-02	4.40E-02
EXOT b44	3.20E-04	0.00E+00	1.83E-04
EXOT a50	-9.28E-03	3.60E-02	4.56E-02
EXOT b55	-2.32E-05	0.00E+00	3.53E-05
EXOT favg	1.00E-03	1.37E-03	1.68E-03
EXOT f	6.00E-04	8.40E-04	4.77E-04
EXOTalpha	0.00E+00	0.00E+00	5.58E-04
CO2 f avg	-2.38E-03	-2.38E-03	-2.02E-03
O f avg	2.84E-03	2.84E-03	6.00E-03
CO2 alpha	0.00E+00	0.00E+00	0.00E+00
O alpha	0.00E+00	0.00E+00	3.32E-03
O f	1.20E-03	1.20E-03	3.06E-03
He k	1.00E+00	1.00E+00	1.00E+00

## **Appendix D: Observations Versus VIRA and One Step SZA Model Residuals**

Plots in this section are provided to give some idea as to how the updated model using one step coefficient set compares to the observed densities used to generate the updated model. The first seven pages show the seven drag density data sets versus the one step SZA(solid line) and VIRA(dashed line) coefficient models. The remaining 17 pages are plots of reaction wheel data orbits showing the following: the density measurement ( $\text{g/cm}^3$ ) (shown as the circle) with associated standard deviations (error bars) which represent the original Espiritu<sup>2</sup> results and have not been multiplied by a factor of four; the model density prediction from the one step SZA coefficient set model (solid line); the model density prediction from the VIRA model (dashed line); and corresponding drag density observation (star), if available.

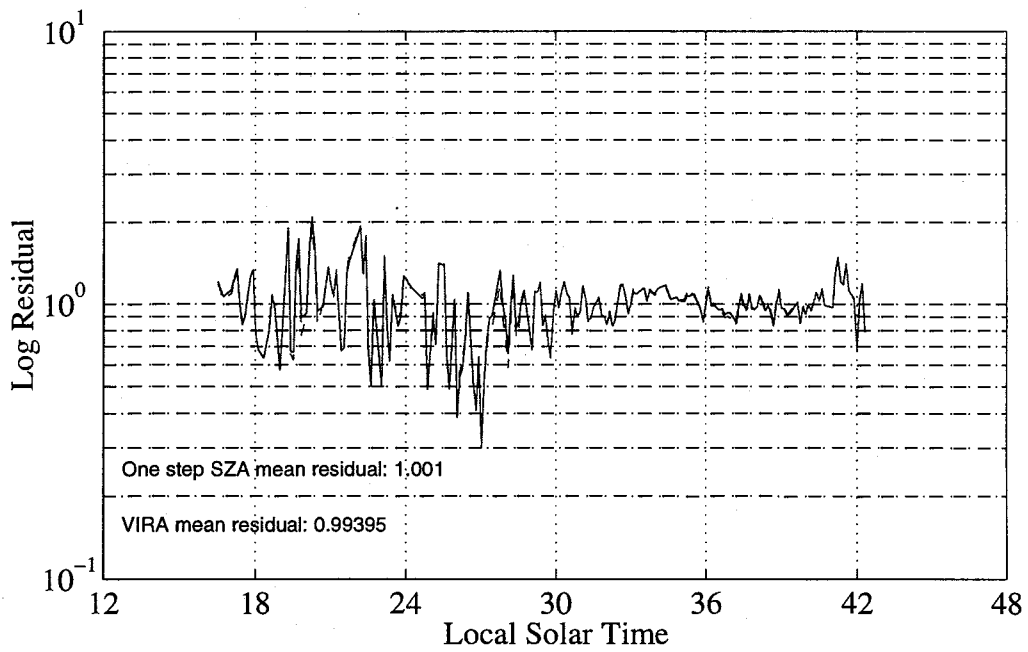
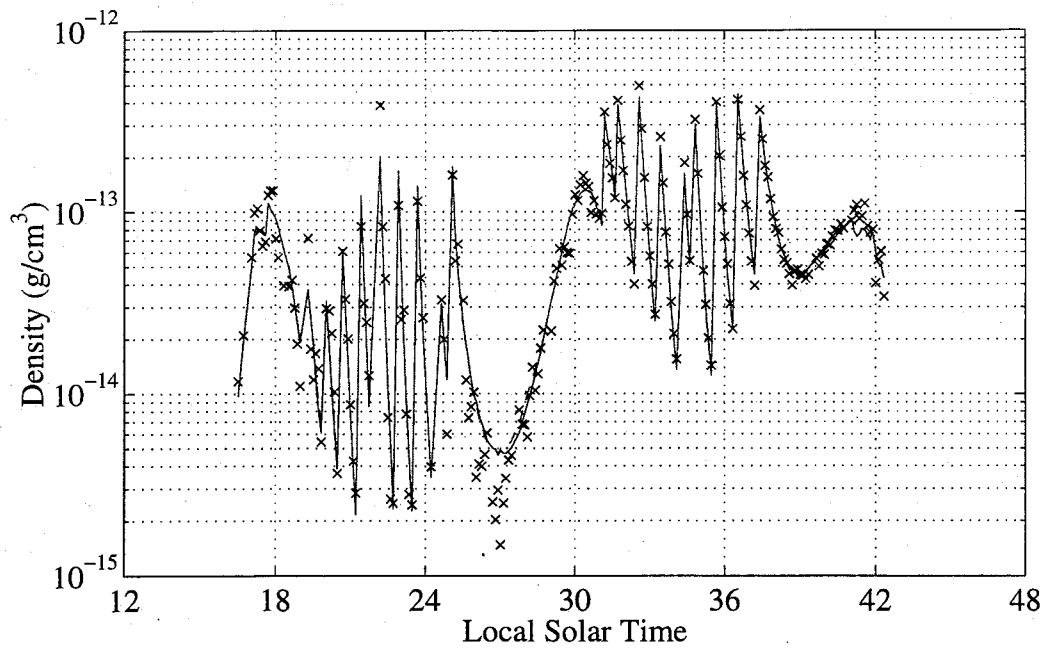


Figure D.1 : Pioneer Venus Data 78-80 part I

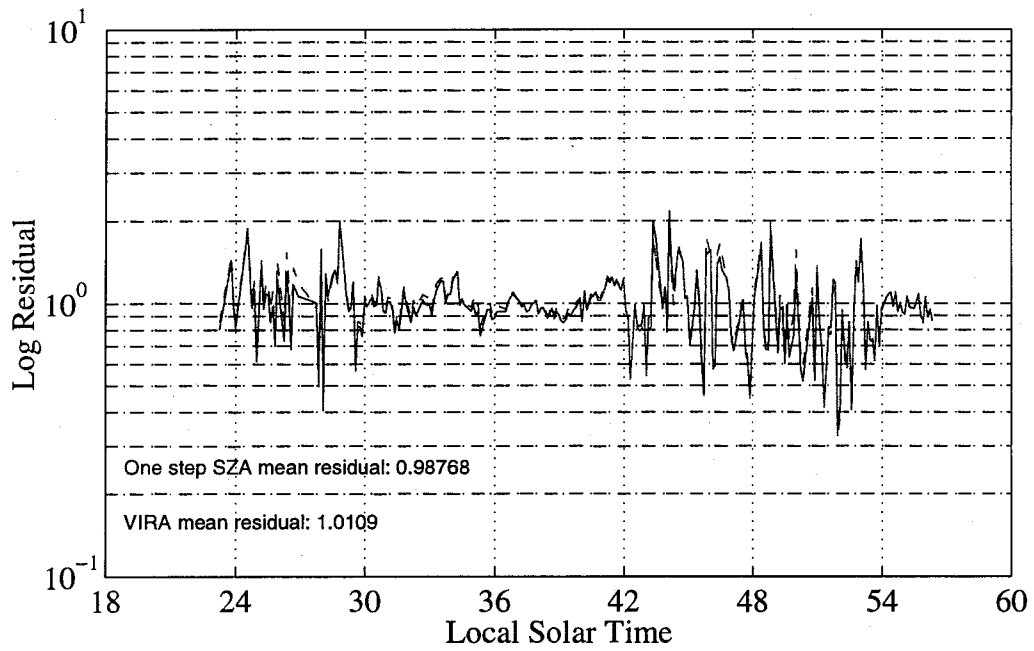
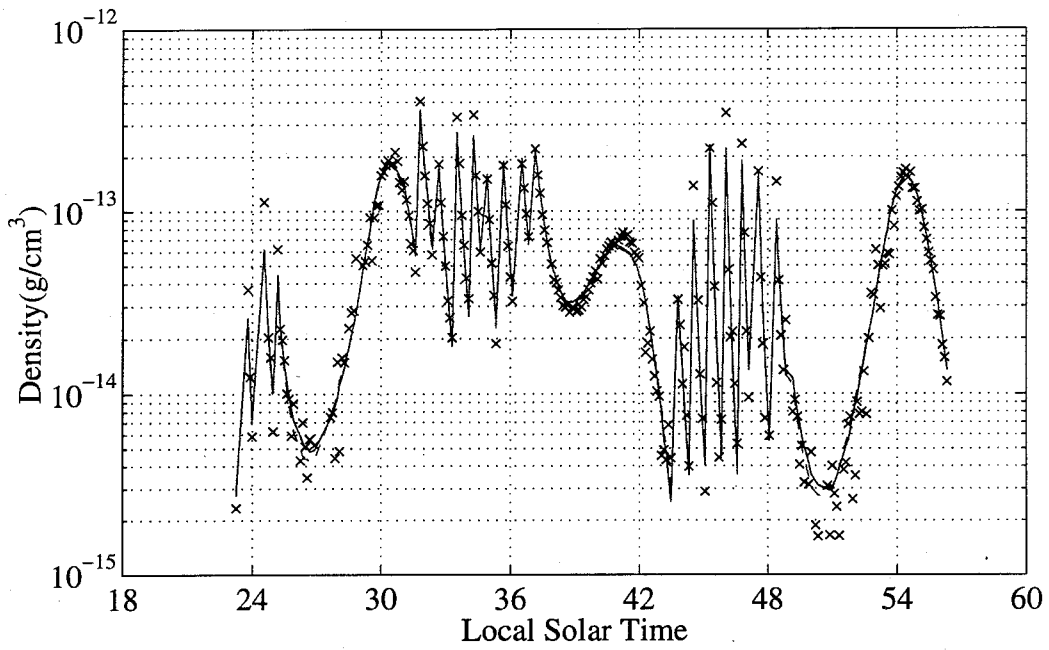


Figure D.2 : Pioneer Venus Data 78-80 part II

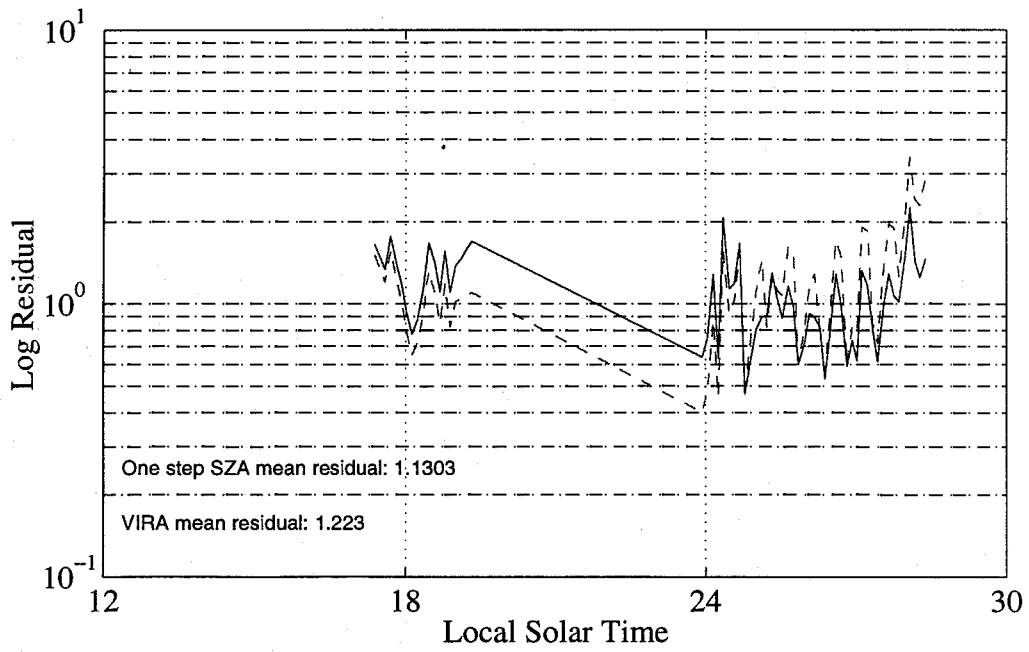
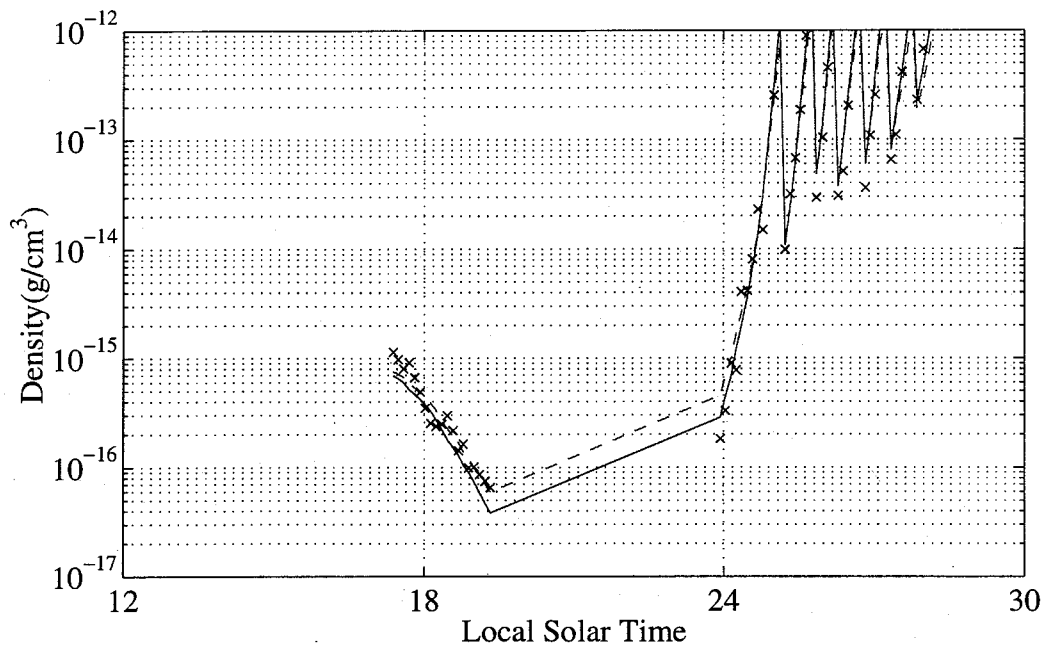


Figure D.3 : Pioneer Venus Data 92

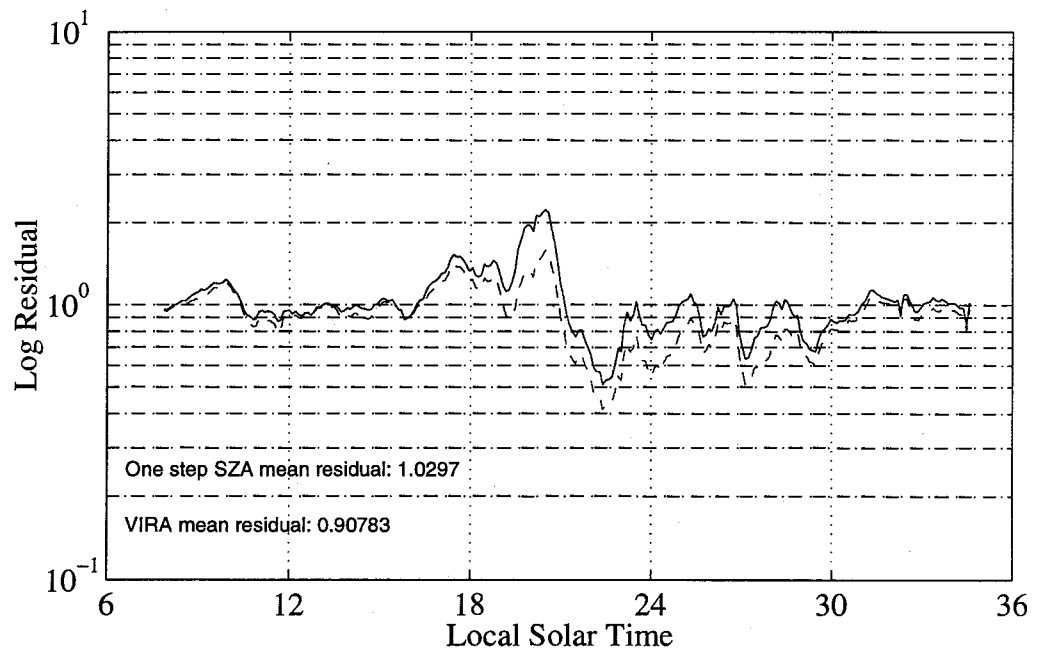
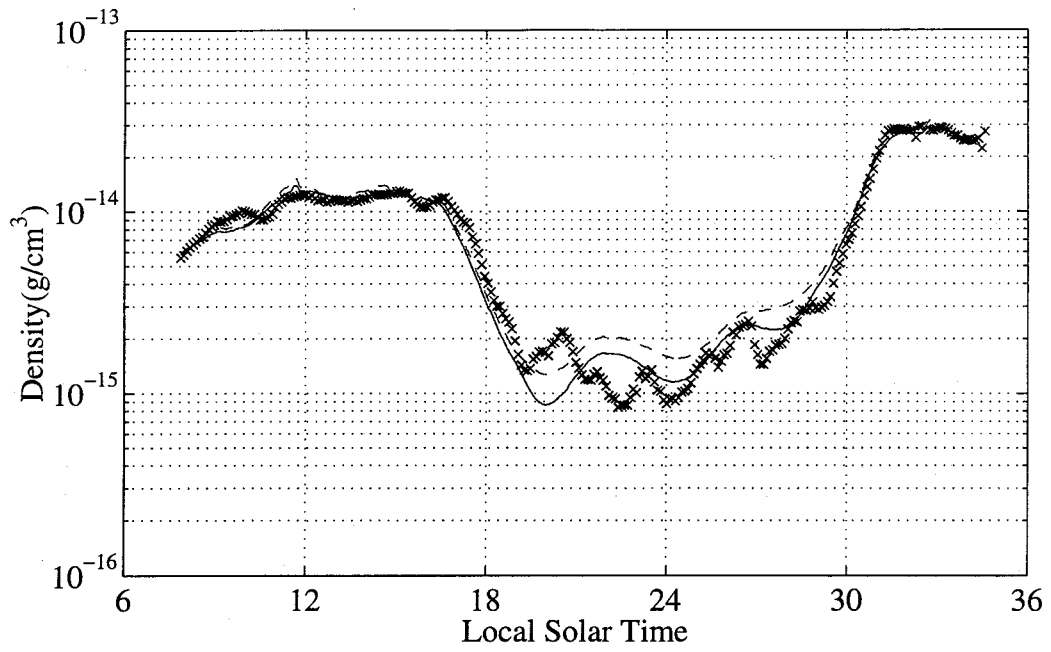


Figure D.4 : Magellan Cycle 4

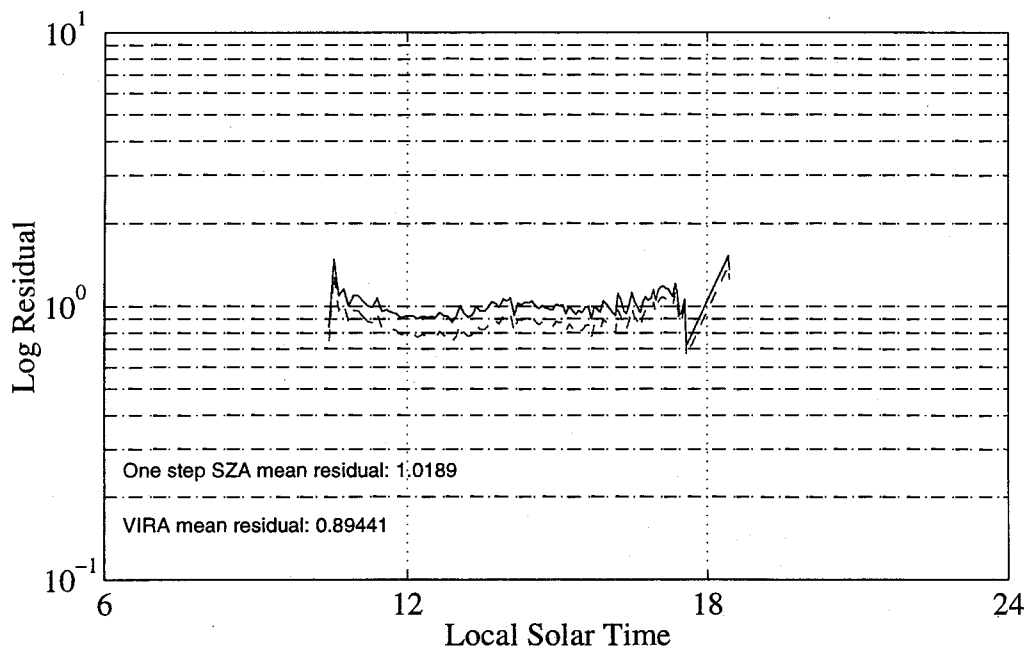
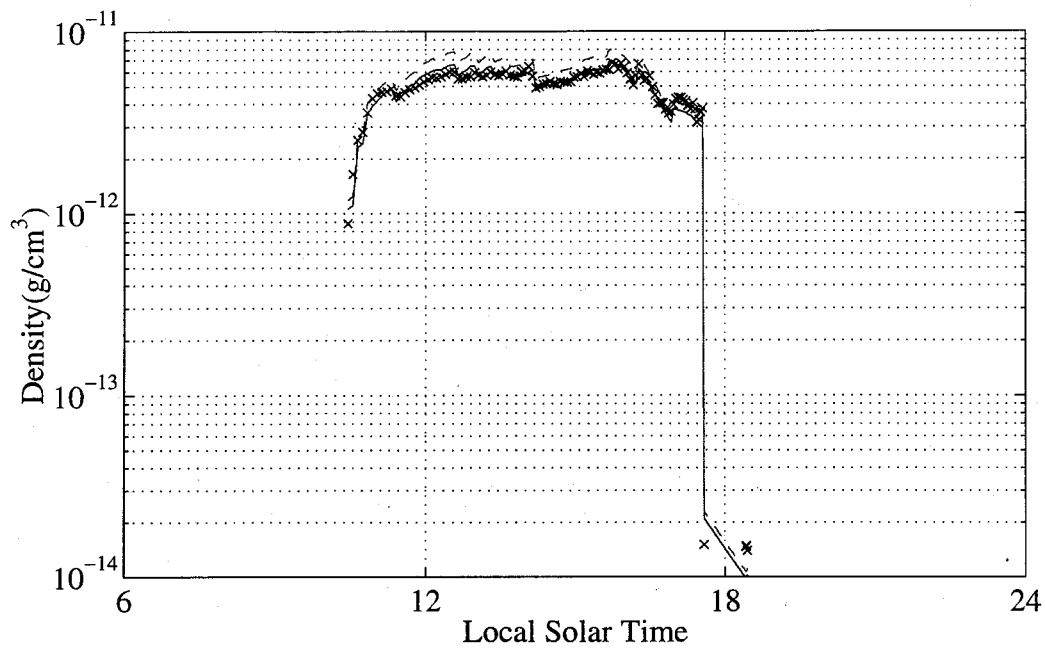


Figure D.5 : Magellan Aerobraking

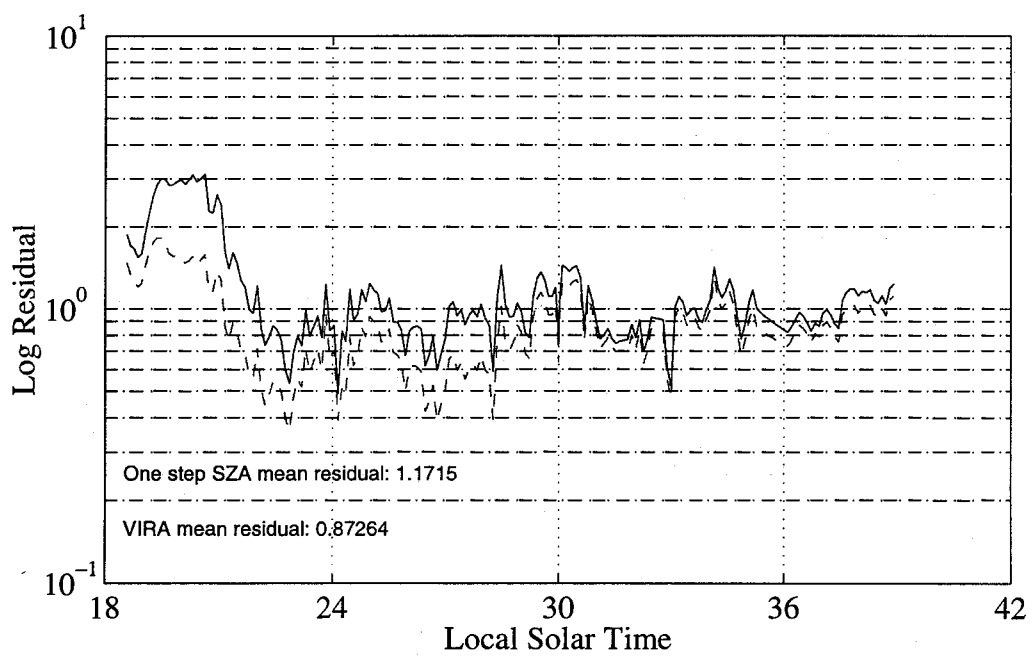
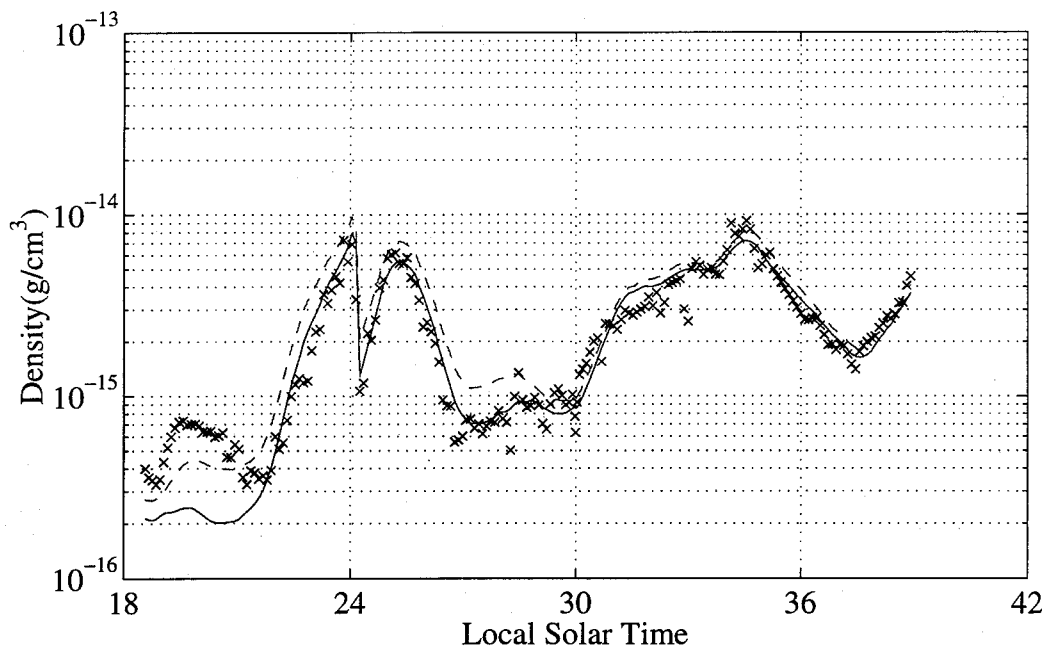


Figure D.6 : Magellan Cycle 5

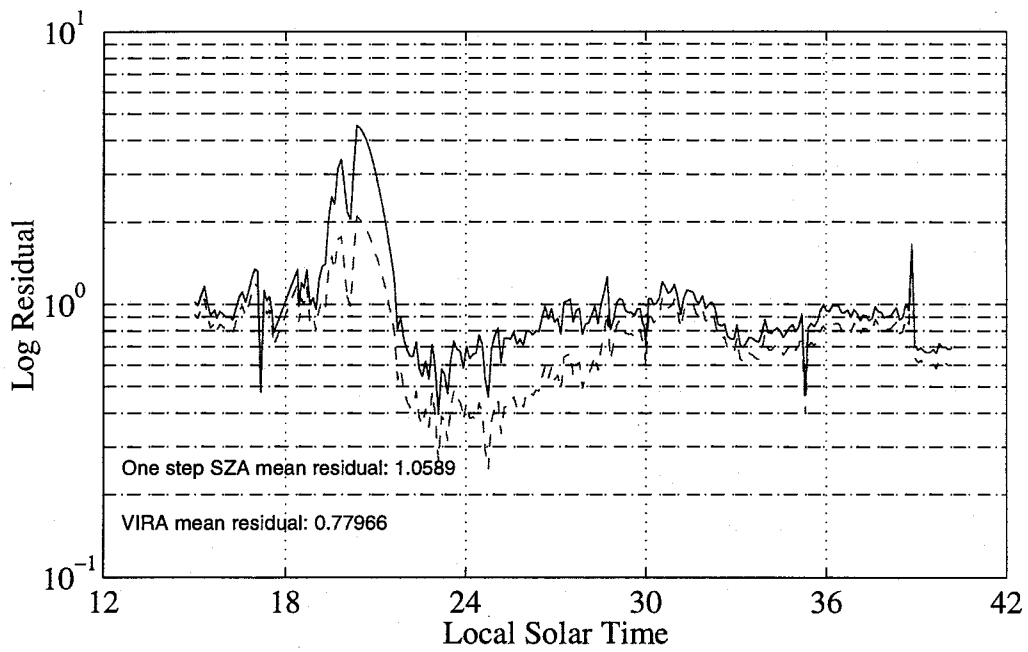
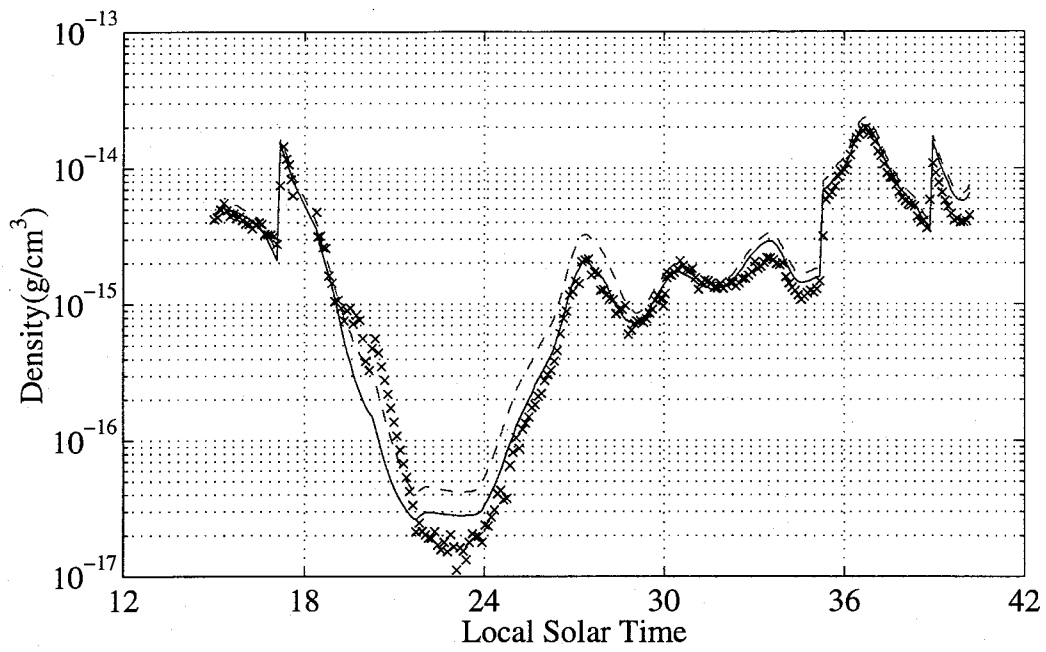


Figure D.7 : Magellan Cycle 6

